



UNIVERSITA' DEGLI STUDI DI MILANO
DIPARTIMENTO DI FISICA
SCUOLA DI DOTTORATO IN
FISICA, ASTROFISICA E FISICA APPLICATA
CICLO XXIV

**THE BOREXINO IMPACT IN THE GLOBAL
ANALYSIS OF NEUTRINO DATA**

Settore Scientifico Disciplinare FIS/04

Tesi di Dottorato di:
Alessandra Carlotta Re

Tutore: Prof.ssa Emanuela Meroni

Coordinatore: Prof. Marco Bersanelli

Anno Accademico 2010-2011

Contents

Introduction	1
1 Neutrino Physics	3
1.1 Neutrinos in the Standard Model	4
1.2 Massive neutrinos	7
1.3 Solar Neutrinos	8
1.3.1 pp chain	9
1.3.2 CNO chain	13
1.3.3 The Standard Solar Model	13
1.4 Other sources of neutrinos	17
1.5 Neutrino Oscillation	18
1.5.1 Vacuum oscillations	20
1.5.2 Matter-enhanced oscillations	22
1.5.3 The MSW effect for solar neutrinos	26
1.6 Solar neutrino experiments	28
1.7 Reactor neutrino experiments	33
1.8 The global analysis of neutrino data	34
2 The Borexino experiment	37
2.1 The LNGS underground laboratory	38
2.2 The detector design	40
2.3 Signal processing and Data Acquisition System	44
2.4 Calibration and monitoring	45
2.5 Neutrino detection in Borexino	47
2.5.1 Neutrino scattering cross-section	48
2.6 ${}^7\text{Be}$ solar neutrino	48
2.6.1 Seasonal variations	50
2.7 Radioactive backgrounds in Borexino	51

CONTENTS

2.7.1	External backgrounds	53
2.7.2	Internal backgrounds	54
2.8	Physics goals and achieved results	57
2.8.1	^7Be solar neutrino flux measurement	57
2.8.2	The day-night asymmetry measurement	58
2.8.3	^8B neutrino flux measurement	60
2.8.4	Pep neutrino flux measurement	61
2.8.5	Geo-neutrino observation	63
3	Toward the global analysis: the method	67
3.1	Survival probability computation	68
3.1.1	Survival probability: the sun contribution	72
3.1.2	Survival probability: the earth contribution	73
3.2	Experimental input data	77
3.3	Computation of the expected results	78
3.4	The statistical approach	78
4	Analysis of Borexino data	81
4.1	The berillium contribution	82
4.2	The boron contribution	85
4.2.1	The boron spectral shape contribution	88
4.3	The Day-Night asymmetry contribution	89
4.4	The pep contribution	94
4.5	Conclusions	96
5	Global analysis of data from neutrino experiments	99
5.1	Analysis of solar neutrino data	101
5.1.1	Analysis of radiochemical data	103
5.1.2	Analysis of SNO data	103
5.1.3	Analysis of Super Kamiokande data	105
5.1.4	Analysis of all solar neutrino data	107
5.2	Analysis of KamLAND anti-neutrino data	111
5.3	Joint analysis of solar and KamLAND data	114
5.4	Terrestrial neutrino sources contribution	116
5.5	Global analysis of neutrino data	117
5.6	The free-fluxes analysis	118
5.6.1	Berillium and boron fluxes as free parameters	120
5.6.2	CNO fluxes as free parameters	123

CONTENTS

Conclusion	127
List of publication and activities	129
A Results of global analyses	133
Bibliography	150
Acknowledgements	151

List of Figures

1.1	Processes of the pp chain reaction	10
1.2	Processes of the CNO cycle	12
1.3	Power generation per mass unit of fuel for pp and CNO processes	12
1.4	Solar neutrino fluxes on the earth's surface	14
1.5	The effective masses of neutrinos in matter	24
1.6	Non-adiabatic evolution	26
1.7	Trend of neutrino P_{ee} vs. energy	28
1.8	General scenario of the $\tan^2 \theta_{12} - \Delta m_{21}^2$ space of parameters	36
2.1	Inside view of the Borexino detector	37
2.2	LNGS underground laboratories map	38
2.3	Prospect of the expected muons flux vs. depth overburden	39
2.4	Schematic view of the Borexino detector	40
2.5	Some Borexino experiment's components	42
2.6	Layout of the Borexino experiment in the Hall C of the LNGS	43
2.7	Block diagram of the Borexino electronics layout	45
2.8	Tree-level Feynman diagrams for ν - e^\pm scattering	47
2.9	Typical ${}^7\text{Be}$ recoil-electron spectrum	49
2.10	Pictorial representation of the earth-sun orbit	50
2.11	A Monte Carlo fit of the Borexino signal in the 270-1600 keV energy region	59
2.12	The global experimental constraints on the low energy solar P_{ee}	59
2.13	Borexino ${}^8\text{B}$ recoil energy spectrum	61
2.14	Electron neutrino survival probability as a function of energy	62
2.15	Geo-neutrinos theoretical spectrum	65
2.16	Borexino geo-neutrinos analysis	65
3.1	Scheme of neutrino flavor eigenstate evolution	68
3.2	Trend analysis of the oscillating term $f(\zeta)$	71
3.3	Solar density profile	72

LIST OF FIGURES

3.4	Solar neutrinos production points distribution	73
3.5	Pictorial representation of the earth	74
3.6	Earth density profile	75
3.7	Annual average of the solar exposure as a function of the nadir angle θ_z	76
3.8	Expected solar exposure for the Borexino experiment	76
4.1	Iso-contours for the Borexino ${}^7\text{Be}$ neutrino flux	83
4.2	Fit of the Borexino ${}^7\text{Be}$ neutrino flux result	85
4.3	Iso-contours for the Borexino ${}^8\text{B}$ neutrino total flux	86
4.4	Fit of the Borexino ${}^7\text{Be}$ and ${}^8\text{B}$ neutrino flux results	87
4.5	Fit of the Borexino ${}^7\text{Be}$ and ${}^8\text{B}$ neutrino results	88
4.6	Δm_{21}^2 χ^2 -profile of the Borexino ${}^7\text{Be}$ and ${}^8\text{B}$ results analysis	89
4.7	Iso-contours for the Borexino ${}^7\text{Be}$ neutrino flux during day and night.	90
4.8	Iso-contours for the A_{DN} of the Borexino ${}^7\text{Be}$ signal.	90
4.9	Fit of the Borexino day-night asymmetry	91
4.10	Fit of the Borexino day-night asymmetry, ${}^7\text{Be}$ and ${}^8\text{B}$ neutrino results	92
4.11	Δm_{21}^2 χ^2 -profile of the Borexino ${}^7\text{Be}$, A_{DN} and ${}^8\text{B}$ results analysis	93
4.12	Iso-contours for the Borexino pep neutrino flux	94
4.13	Fit of all the available Borexino results	95
4.14	Δm_{21}^2 χ^2 -profile of the Borexino global analysis	96
5.1	Fit of the radiochemical experiments data	102
5.2	Fit of the SNO experiment results	104
5.3	Fit of the SK experiment results	106
5.4	Fit of the solar experiments (Borexino excluded) results	108
5.5	Fit of the solar experiments results	109
5.6	Δm_{21}^2 χ^2 -profile of the solar global analysis without and with Borexino	110
5.7	$\sin^2 \theta_{13}$ χ^2 -profile of the solar global analysis	110
5.8	$\sin^2 \theta_{13}$ χ^2 -profile of the KamLAND analysis	111
5.9	Fit of the KamLAND experiment results	112
5.10	The solar vs reactor data fit at different $\sin^2 \theta_{13}$ values	113
5.11	Fit of the joint solar and KamLAND data-set	115
5.12	$\sin^2 \theta_{13}$ χ^2 -profile of the joint solar-KamLAND analysis	115
5.13	$\sin^2 \theta_{13}$ χ^2 -profile of the atmospheric, reactor and accelerator analysis	116
5.14	Global analysis of all the neutrino experimental results	117
5.15	$\sin^2 \theta_{13}$ χ^2 -profile of the global analysis	118
5.16	Global fit with Be and B as free parameters	122
5.17	Global fit vs SHP11 high and low-metallicity neutrino fluxes predictions	123

LIST OF FIGURES

5.18 Global fit with Be, B and CNO as free parameters	124
5.19 f_{CNO} χ^2 -profile of the joint solar-KamLAND global analysis	124

List of Tables

1.1	Fermion quantum fields in the Standard Model	5
1.2	Neutrino fluxes predicted by the SHP11 Standard Solar Model	16
1.3	Characteristic values of L and E for neutrino sources and experiments	20
2.1	Calibrations sources: the gamma emitting isotopes.	47
2.2	Calibration sources	47
2.3	Rock radioactivity at LNGS underground laboratories	52
2.4	Typical sources of background in Borexino	56
2.5	The best estimates for the pep and CNO solar neutrino interaction rates	63
3.1	Coverage probability in correspondance to $\Delta\chi^2$ values	79
4.1	Summary of the Borexino experimental input data	82
5.1	Summary of the experimental input data	100
5.2	Some of the neutrino fluxes predicted by the SHP11 model	119
A.1	Results of the analysis of Borexino data at different θ_{13} values	134
A.2	Results of the analysis of radiochemical data at different θ_{13} values	135
A.3	Results of the analysis of SNO data at different θ_{13} values	136
A.4	Results of the analysis of Super Kamiokande data at different θ_{13} values	137
A.5	Results of the analysis of KamLAND data at different θ_{13} values	138
A.6	Results of the analysis of the solar-without-Borexino data set at different θ_{13} values	139
A.7	Results of the analysis of the solar-with-Borexino data set at different θ_{13} values	140
A.8	Results of the analysis of the solar plus KamLAND data set at different θ_{13} values	141

Introduction

It is 2012 and we live in a world permeated by technology and science. Words like progress, energy and physics are getting more and more familiar day by day. Today, if one Googles neutrino, more than 8,780,000 results appear in a tenth of a second.

This burst of growth in neutrino's fame is mainly due to the exciting developments that neutrino physics has seen over the past decade, following the experimental evidence of their oscillations in the atmospheric, solar, reactor and accelerator sectors. In fact, a precise measurement of neutrino properties plays a crucial role in understanding many phenomena, from fundamental interactions to physics at the cosmological scale.

This thesis reports on the work I carried out within the Borexino collaboration in the past three years.

The Borexino detector, designed and constructed for sub-MeV solar neutrino spectroscopy, is taking data at the Gran Sasso Laboratory (LNGS, Italy) since May 2007. The detector was designed according to the principle of graded shielding and today is characterized by an extreme radiopurity.

Since the start of data taking, the Borexino collaboration has released many interesting results. During last year, there have been three publications which demonstrate the unique characteristics of Borexino: the ${}^7\text{Be}$ solar neutrino rate measurement with an accuracy better than 5%, the evidence of a null day-night asymmetry with accuracy of $\sim 1.5 \times 10^{-2}$, and, for the first time, the direct measurement of the so-called pep solar neutrino flux (Ref. [1, 2, 3]).

Starting from January 2009, I have been directly involved in many aspects of the data-taking activities e.g. the regular data acquisition (DAQ) shifts and the detector extensive calibration campaigns. In January 2011 I was appointed "run coordinator": I spent a month in LNGS coordinating the Borexino DAQ crews, supervising the detector electronics and, during one of the scintillator purification campaigns, being responsible for the communication between the software and the operational groups, creating a crucial link that contributed to the overall success of the task.

These activities helped in collecting the data used in the work I present.

My original contribution consisted in analyzing the Borexino results (the ones listed above and also the boron neutrino flux measurement in Ref. [4]), in order to understand their implications in neutrino oscillation physics and in solar astrophysics. In particular, I reviewed, improved and developed a code through which it was (and still is today) possible to realize the actual impact of the Borexino experiment in the global analysis of neutrino data.

The dissertation is structured in two main parts: the first is a short review of neutrino physics, in particular solar neutrino physics, with an excursus on the Borexino experiment; the second is devoted to areas in which my contribution was more significant and direct and it concerns the so-called global analysis of data from Borexino, and from solar atmospheric, reactor, and accelerator oscillation experiments.

In chapter 1, the current situation of neutrino oscillations and solar neutrino physics is presented, along with an outline of the global analysis of neutrino data.

Chapter 2 summarizes Borexino's physics goals, its design, detection principle, and requirements.

Chapter 3 introduces the basic assumptions of our global analysis: from the very first steps of the analysis chain to the statistical approach we use while processing the output data.

Chapter 4 deals with the Borexino contribution to the global analysis of neutrino data. Each Borexino result is introduced and analyzed.

Finally, chapter 5 concerns the Borexino impact in the global analysis of all the neutrino data, examined from the point of view of neutrino oscillation physics and from that of solar astrophysics.

Every effort was made to write each chapter so that it could be read individually. However, cross-references to sections from different chapters are given for better comprehension of specific topics.

Chapter 1

Neutrino Physics

The phenomenon of radioactivity was discovered in 1892 by Henry Becquerel. Niels Bohr was the first physicist to realize that beta decay is a process in which the electron is ejected from the nucleus, but a two-body decay clashed with the discovery of the continuous spectrum of beta rays by James Chadwick, in 1914. This discovery posed a difficult problem from the theoretical point of view until Wolfgang Pauli, in 1929, wrote his famous letter (Ref. [5]) about saving the energy conservation law in the nuclear beta decay process by means of a new particle:

“Dear Radioactive Ladies and Gentlemen,
[...] I have, in connection with the continuous β -spectrum, hit upon a desperate remedy for rescuing the alternation law¹ of statistics and the energy law. This is the possibility that there might exist in the nuclei electrically neutral particles, [...] which have spin half, obey the exclusion principle and moreover differ from light quanta in not travelling with the velocity of light.”

So, the neutrino was born into the world of theoretical physics. Even if Pauli didn't published his idea since he considered the proposal too tentative to justify its appearance in published records, the idea spread throughout the community. In 1932 Chadwick discovered the neutron and, in 1933, Fermi wrote the four-fermion Hamiltonian (Ref. [6]) for beta decay using the electron, the proton, the neutron and, for the first time, the neutrino. A new field of theoretical physics came into existence: the weak interaction.

In early 1950's, Fred Reines and Clyde Cowan started thinking about neutrino detection; their first plans were to detect neutrinos emitted from nuclear explosions but, realizing that nuclear reactors could provide a much higher neutrino flux, they mounted an experiment at the Hanford nuclear plant.

¹The "alternation law" is now commonly known as spin-statistics theorem.

1.1 Neutrinos in the Standard Model

The idea was to detect electron anti-neutrinos as the initiator of the inverse beta decay reaction:

$$\bar{\nu}_e + p \rightarrow n + e^+ .$$

The Hanford experiment had a large background due to cosmic rays even when the reactor was off so, in 1955, the detector was moved to the Savannah River nuclear plant, in a location at 11 m from the reactor center and 12 m underground. Finally, in 1956, Cowan and Reines provided the very first experimental evidence of neutrino's existence.

Starting from the 1960's, neutrinos produced in the sun, in the atmosphere and from supernovae were also observed. Ever since it was proposed, the neutrino has played crucial roles from time to time in the advancement of our understanding of particle physics.

1.1 Neutrinos in the Standard Model

One of the greatest successes of theories and discoveries over the past century has been the establishment that everything in the universe has to be made up of twelve basic building blocks, the so-called *elementary particles*, governed by four fundamental forces: the strong force (reference intensity: $I = 1$), the electromagnetic force (relative intensity: $I_{\text{rel}} = 10^{-2}$), the weak force ($I_{\text{rel}} = 10^{-7}$) and the gravitational force ($I_{\text{rel}} = 10^{-39}$).

The very simple but comprehensive theory which explains how these twelve elementary particles and three of the forces are related to each other, is the so-called *Standard Model* (SM) of particles and forces. Developed in the early 1970s, this model has successfully explained a host of experimental results and precisely predicted a wide variety of phenomena.

Thanks to the works of Glashow, Salam, Ward, Weinberg, Iliopoulos, Maiani and many others physicists, a model for the electroweak and strong interactions has been built and today we know that the Standard Model is based on the gauge group:

$$G_{\text{SM}} = \text{SU}(3)_C \times \text{SU}(2)_L \times \text{U}(1)_Y , \tag{1.1}$$

where the strong, weak and electromagnetic interactions are respectively connected to the $\text{SU}(3)_C$, $\text{SU}(2)_L$ and $\text{U}(1)_Y$ gauge groups. In particular, the Quantum Chromodynamics (QCD) theory, that is the theory of strong interactions, is based on the $\text{SU}(3)_C$ group while $\text{SU}(2)_L \times \text{U}(1)_Y$ is the group underlying the Weinberg-Salam theory of electroweak interactions.

$\text{SU}(3)_C$ and $\text{SU}(2)_L \times \text{U}(1)_Y$ do not mix with each other and, therefore, the strong and electroweak interactions can be treated separately.

The twelve elementary particles have spin half and are called *fermions* since they obey to the Fermi-Dirac statistics. Moreover, according to the spin-statistics theorem, they respect the Pauli exclusion principle.

The fermions are classified according to how they interact: there are six quarks and six leptons; pairs from each classification are grouped together to form a generation with corresponding particles exhibiting similar physical behavior.

The six quarks are paired in three generations: the up and down quarks form the first generation, followed by the charm and strange quarks, and then the top and bottom quarks.

The six leptons are similarly arranged: according to flavor, there is the electronic family (electron and electron neutrino), the muonic (muon and muon neutrino), and the tauonic (tau and tau neutrino) family.

The defining property of the quarks is that they carry color charge, and hence, interact via the strong interaction. Combinations of quarks and anti-quarks generate baryons and mesons, in general hadrons. Hadrons interact with other fermions both electromagnetically and via the weak interaction.

Three (e^- , μ^- , τ^-) of the six leptons have electric charge whereas the neutrinos (ν_e , ν_μ , ν_τ) are electrically neutral. By virtue of carrying an electric charge, the electron, muon, and tau leptons interact electromagnetically while the three neutrinos dynamics is directly influenced by the weak nuclear force only. A general statement about neutrinos is that they do not decay and pervade the universe although rarely interact with baryonic matter.

Quantum field	SU(3) _C	SU(2) _L	U(1) _Y
$Q_L = \left(\begin{matrix} u_L \\ d_L \end{matrix} \right), \left(\begin{matrix} c_L \\ s_L \end{matrix} \right), \left(\begin{matrix} t_L \\ b_L \end{matrix} \right)$	3	2	1/6
$L_L = \left(\begin{matrix} \nu_{eL} \\ e_L \end{matrix} \right), \left(\begin{matrix} \nu_{\mu L} \\ \mu_L \end{matrix} \right), \left(\begin{matrix} \nu_{\tau L} \\ \tau_L \end{matrix} \right)$	1	2	-1/2
$U_R = u_R, c_R, t_R$	3	1	2/3
$D_R = d_R, s_R, b_R$	3	1	-1/3
$E_R = e_R, \mu_R, \tau_R$	1	1	-1

Table 1.1: Fermion quantum fields in the Standard Model. Quantum numbers relative to the gauge symmetries are indicated.

1.1 Neutrinos in the Standard Model

The complete set of fermions entering the Standard Model is shown in Tab. 1.1 together with the corresponding quantum numbers: right- and left-handed fields are listed separately. This is due to the fact that the weak interaction only involves the left-handed fields and therefore the Standard Model is a chiral theory.

The model also contains a single Higgs boson doublet Φ with charges $(1, 2, \frac{1}{2})$, whose vacuum expectation value breaks the gauge symmetry. This is the only piece of the SM model which still misses experimental confirmation and for this reason the search for the Higgs boson remains one of the premier tasks of present and future high energy collider experiments.

Neutrinos that reside in the lepton doublets are named *active neutrino* and they have weak interactions. On the other hand, if a neutrino does not have SM gauge interaction, it is called *sterile neutrino* and it is a singlet of the global SM gauge group.

The SM only admits three active neutrinos accompanying the charged lepton flavor eigenstates, e^- , μ^- and τ^- therefore the weak charged current (CC) interactions between neutrinos and their corresponding charged leptons are given by the Lagrangian:

$$-\mathcal{L}_{CC} = \frac{g}{2 \cos \theta_W} \sum_l \bar{\nu}_{Ll} \gamma^\mu l_L^- W_\mu^+ + \text{h.c.} . \quad (1.2)$$

In addition, the SM neutrinos have also neutral current (NC) interactions:

$$-\mathcal{L}_{NC} = \frac{g}{\sqrt{2}} \sum_l \bar{\nu}_{Ll} \gamma^\mu \nu_{Ll} Z_\mu^0 . \quad (1.3)$$

W^\pm and Z^0 are, respectively, the charged and neutral vector bosons which mediate the weak interactions. These bosons are very massive ($M_{W,Z} \approx 90 \text{ GeV}$) hence they give rise to interactions of very short range. W^\pm exchange results in a change of charge of the lepton, while Z^0 exchange does not.

In the Standard model all neutrino interactions are described by these two Lagrangians and no sterile neutrinos are assumed to exist. Furthermore, from Eq. 1.3 it is possible to determine the decay width of the Z^0 boson into neutrinos. This decay width results to be proportional to the number of light² left-handed neutrinos. At present the measurement of the invisible Z^0 width yields $N_\nu = 2.984 \pm 0.008$ (Ref. [7]) hence it follows that there are only three light active neutrinos.

An important feature of the SM, which is relevant to the question of the neutrino mass, is the fact that the gauge symmetry G_{SM} and the particle content of Tab.1.1

²In defining a neutrino light, we reasonably assume that $m_\nu \leq \frac{m_{Z^0}}{2}$.

presents an accidental global symmetry:

$$G_{\text{SM}}^{\text{global}} = \text{U}(1)_{\text{B}} \times \text{U}(1)_{\text{L}_e} \times \text{U}(1)_{\text{L}_\mu} \times \text{U}(1)_{\text{L}_\tau} .$$

$\text{U}(1)_{\text{B}}$ is the baryon number symmetry, and $\text{U}(1)_{\text{L}_e, \text{L}_\mu, \text{L}_\tau}$ are the three lepton flavor symmetries, with total lepton number given by

$$\text{L} = \text{L}_e + \text{L}_\mu + \text{L}_\tau .$$

In the Standard Model, fermions masses arise from the Yukawa interactions which couple a right-handed fermion with its left-handed doublet and the Higgs field:

$$-\mathcal{L}_{\text{Yukawa}} = Y_{ij}^{\text{d}} \bar{Q}_{\text{Li}} \phi \text{D}_{\text{Rj}} + Y_{ij}^{\text{u}} \bar{Q}_{\text{Li}} \tilde{\phi} \text{U}_{\text{Rj}} + Y_{ij}^{\text{l}} \bar{L}_{\text{Li}} \phi \text{E}_{\text{Rj}} + \text{h.c.} , \quad (1.4)$$

where $\tilde{\phi} = i\tau_2 \phi^*$. After a spontaneous symmetry breaking, the Yukawa contribution leads to charged fermion masses defined as:

$$m_{ij}^{\text{f}} = Y_{ij}^{\text{f}} \frac{v}{\sqrt{2}} , \quad \frac{v}{\sqrt{2}} = \langle \phi^0 \rangle = 246 \text{ GeV} ,$$

being Y_{ij}^{f} the Yukawa coupling of the fermion fields with the Higgs field, and $\frac{v}{\sqrt{2}}$ the vacuum expectation value of the Higgs field.

However, since no right-handed neutrinos exist in the model, the Yukawa interactions of Eq. 1.4 leave the neutrinos massless. Hence, the Standard Model assumes that neutrinos are massless and, in order to give them a mass, the Standard Model should be extended.

1.2 Massive neutrinos

As it was discussed in the previous paragraph, neutrinos are introduced in the SM as truly massless fermions however, the experiments that measured the flux of atmospheric neutrinos found a disappearance of muon neutrinos when propagating over distances of order of hundreds or more kilometers. On the other hand, experiments that measured the flux of solar neutrinos found a disappearance of solar electron neutrinos while propagating to the earth. These experimental results could be easily explained assuming neutrino flavor oscillations which, as pointed out by Pontecorvo and Gribov (Ref. [8, 9]) in 1968, can occur only if neutrinos are massive and mixed.

In general, additional neutrino mass terms can be of two different types: Dirac or Majorana. In the case of *Dirac neutrinos*, the neutrino mass term is generated by the

1.3 Solar Neutrinos

same standard Higgs mechanisms that produce quark and charged lepton masses. One introduces the fields ν_{R}^i ($i = e, \mu, \tau$), the right-handed neutrino fields, which must be singlets under the SM gauge group: $\nu_{\text{R}}^i(1, 1, 0)$. By introducing the right-handed (sterile) neutrinos, the neutrino mass term does not destroy the global gauge invariance of the total Lagrangian since the Dirac mass term is generated after spontaneous symmetry breaking from Yukawa interactions:

$$-\mathcal{L}_{\text{mass}}^{\text{D}} = M_{\text{D}} (\bar{\nu}_{\text{R}} \nu_{\text{L}} + \text{h.c.}) . \quad (1.5)$$

The total lepton number L is conserved but the separate lepton flavor symmetries are broken. As a consequence, neutrino with definite mass are Dirac particles described by four-component spinors and Dirac neutrinos and anti-neutrinos have opposite L .

In the case of *Majorana neutrinos*, the lepton number L is not conserved anymore and the neutrino mass term is a linear combination of the product of left- and right-handed (charge-conjugate) components of neutrino fields:

$$-\mathcal{L}_{\text{mass}}^{\text{M}} = \frac{1}{2} M_{\text{M}} (\bar{\nu}_{\text{L}}^{\text{c}} \nu_{\text{L}} + \text{h.c.}) . \quad (1.6)$$

The Majorana mass term breaks the lepton number by two units and Majorana neutrinos obey the so-called *Majorana condition*:

$$\nu_{\text{M}} = \nu_{\text{M}}^{\text{c}} .$$

Up to a possible Majorana phase $e^{i\eta}$, this condition implies that one field describes both neutrino and anti-neutrino states, which are not distinguishable. Therefore, a Majorana neutrino is described by a two-component spinor while Dirac particles, are represented by four-component spinors.

At present, the question of the Dirac or Majorana nature for neutrino masses is still theoretically and experimentally open.

1.3 Solar Neutrinos

The basic nuclear process in the sun and in most of the other stars is the fusion of hydrogen into helium. Hydrogen is by far the most abundant element in the universe: more than 90% of the atoms in the universe are hydrogen, and all but less than 1% of the remainder are helium.

We owe the idea that the solar energy is produced by nuclear fusion reactions to Hans Bethe who, in 1939, laid out the foundations of the theory of how stars burn (Ref.

[10]). The sun can be seen as an extremely successful prototype of a self-sustaining thermonuclear reactor. In fact, as far as we can tell from the fossil records on earth, the sun's output has been nearly constant over a time scale of more than 10^9 years.

Neutrinos are an essential part of the process of stellar evolution. The sun shines because of the thermonuclear reactions which happen in the core of the sun and generate the solar energy. These reactions produce electron neutrinos, the so-called *solar neutrinos*, and occur via two main chains: the proton-proton *pp* chain (Sec. 1.3.1) and the carbon *CNO* cycle (Sec. 1.3.2). Both chains end up in the fusion of protons into helium as described via the compact form:



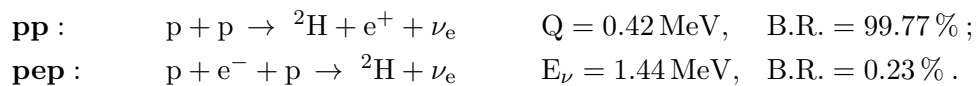
with an energy release of about 28 MeV, eventually appearing as sunlight.

The solar neutrinos have energies roughly in the range of a few MeV, depending on the involved nuclear reactions. Since the density of a typical stellar core is about 100 g/cm^3 and typical ν_e -e scattering cross section is around 10^{-43} cm^2 , the mean free path of a neutrino is of the order of 10^{17} cm , which is much larger than the radius of the sun and of typical stars. Thus, neutrinos escape the sun (or the stars) carrying away about 2-3% of the total energy emitted by the star. Solar neutrinos and in general stellar neutrinos are messengers of physics information coming from the stellar core. Therefore a detailed study of stellar neutrinos is very useful in providing information on stellar interior, as well as in probing the theoretical models for the structure and evolution of the sun and other stars.

1.3.1 pp chain

The theory that a reaction between two protons could be the starting point of the sun burning chain was firstly proposed by sir Arthur Eddington in 1926 (Ref. [11]) but, regardless his theoretical work, it was still unclear how could be possible that a proton-proton fusion proceed since ${}^2\text{He}$, the most obvious product, is very unstable and immediately dissociates back into a pair of protons. Finally in 1939, Hans Bethe proposed (Ref. [10]) that a combination of four protons and two electrons could occur essentially in two ways only: one by assuming two protons to react and form a deuteron, the other by using carbon and nitrogen as catalysts (i.e. the CNO cycle).

Indeed the very first step in the fusion process is the combination of two protons to form the only stable two-nucleon system, the deuteron:



1.3 Solar Neutrinos

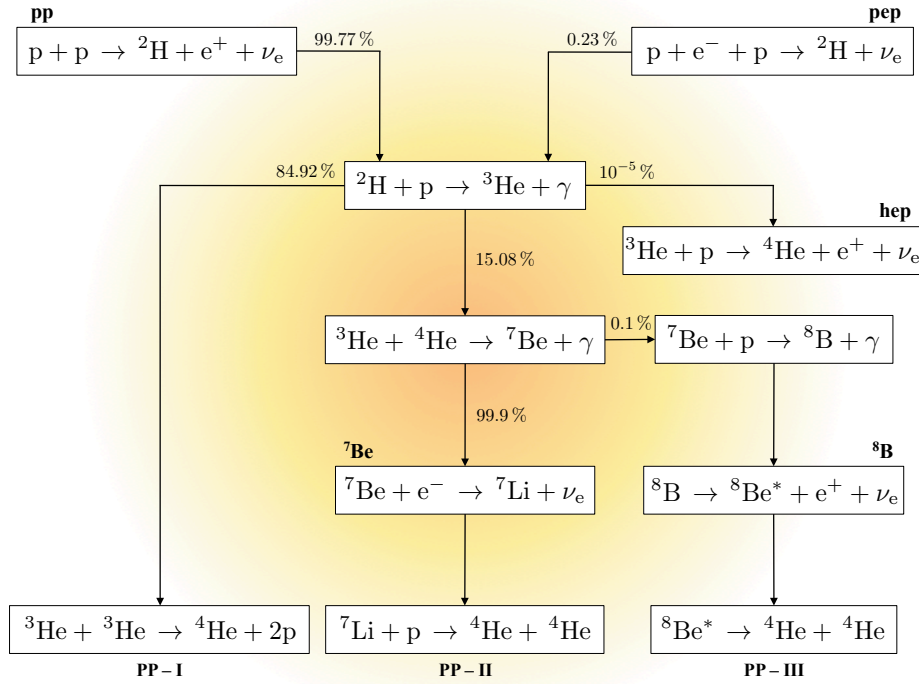
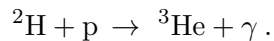


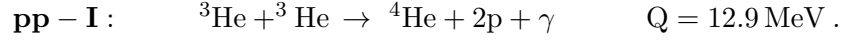
Figure 1.1: Sequence of processes in proton-proton pp chain of fusion reactions.

The neutrino in the final state is the clear signature of a weak interaction process occurring to a proton which decays into a neutron and this is the only possibility since not enough energy is available to create, for instance, a π meson and to have $p \rightarrow n + \pi^+$. After deuterium formation, the following reaction is likely to occur:

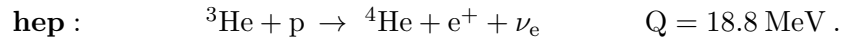


At this point, the deuteron-deuteron reactions are very rare because of the small number of deuterons present: only one deuteron is formed every $\sim 10^{18}$ protons, so it is about 10^{18} times more likely that a deuteron reacts with a proton rather than with another deuteron. It is also unlikely for ^3He to react with ^2H because of the density of ^2H is very low and because deuterium is converted to ^3He very rapidly.

Basically, after the ${}^3\text{He}$ formation, only three sub-branches are possible. The most frequent branch, named PP-I (B.R. $\sim 85\%$), leads to the production of ${}^4\text{He}$ and to the conclusion of the pp chain:

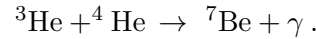


The second sub-branch involves reaction of ${}^3\text{He}$ with protons:

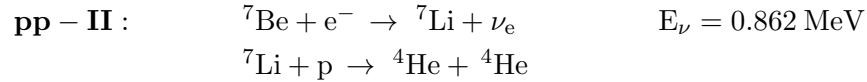


Neutrinos produced in this reaction, the *hep* neutrinos, have a continuous spectrum and are characterized by the highest energy ($E_\nu : 0 - 18.8 \text{ MeV}$) among all the pp chain neutrinos. Anyway, the hep reaction barely happens (B.R. = $10^{-5} \%$).

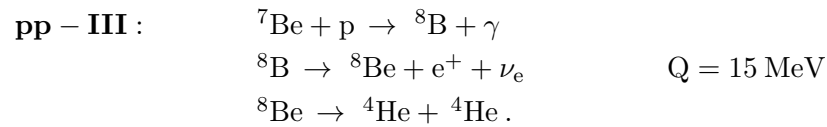
The last possibility (B.R. $\sim 15\%$) is the combination of ${}^3\text{He}$ with an α particle resulting in the creation of ${}^7\text{Be}$:



In this case, the production of ${}^7\text{Be}$ can be followed either by:



or by the processes:



The net reaction and the net Q-value are the same for each of the three possible paths. The one actually chosen depends on the composition of the star and on its temperature. In the sun case, the first channel (PP-I branch, $\sim 85\%$ of total neutrino flux) results in a continuous distribution of neutrinos with a maximum energy of 0.42 MeV. In the second case (PP-II branch, $\sim 15\%$ of the total neutrino flux), the two-body ${}^7\text{Be}$ electron capture gives a monoenergetic neutrino of energy 0.862 MeV (B.R. = 90.7%) while the ${}^8\text{B}$ decay (PP-III branch, $\sim 10^{-4}\%$ of the total neutrino flux) gives a continuous neutrino distribution with endpoint at about 15 MeV. The complete chain is schematically indicated in Fig. 1.1.

1.3 Solar Neutrinos

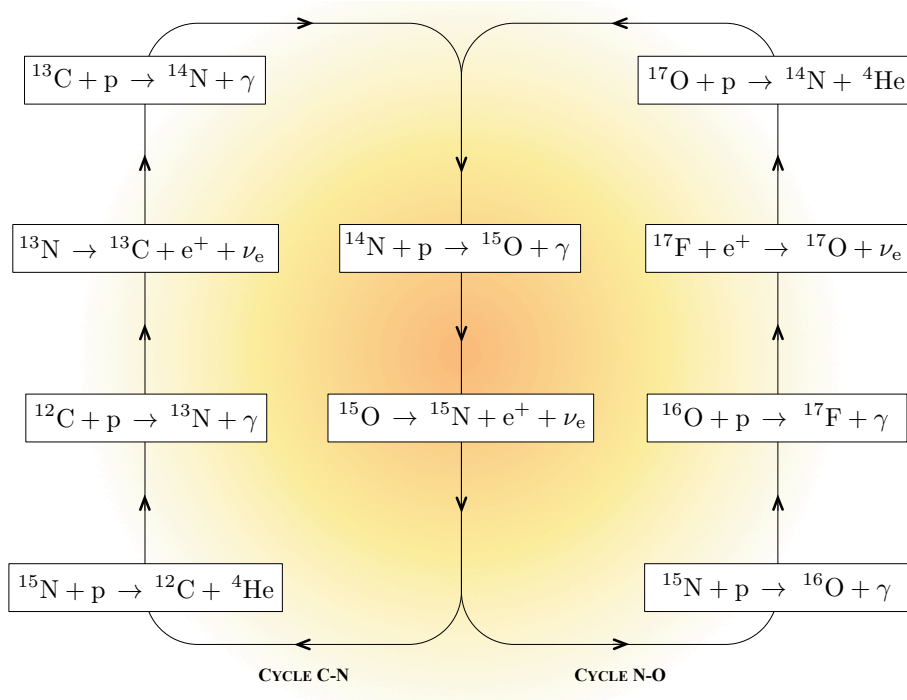


Figure 1.2: Sequence of processes in Carbon *CNO* cycle of fusion reactions.

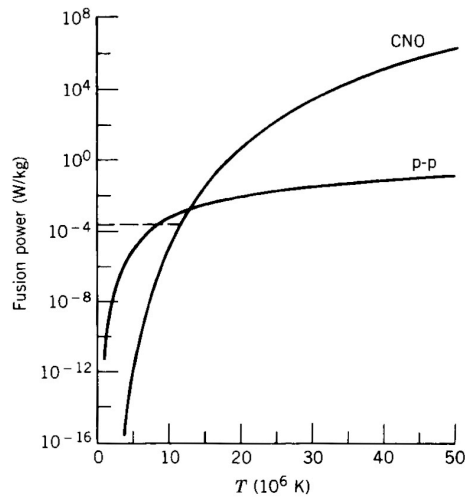
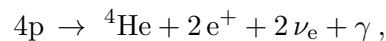


Figure 1.3: Power generation per mass unit of fuel for proton-proton and carbon processes. The dashed line indicates the sun's power of about 2×10^{-4} W/kg (Ref. [12]).

1.3.2 CNO chain

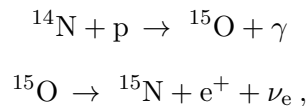
When elements heavier than hydrogen and helium are present in the interior of a star, a series of fusion reaction different from the pp-chain can occur. This is the case of the carbon or CNO cycle (Fig. 1.2). The CNO cycle starts with a ^{12}C nucleus capturing a free proton and producing radioactive ^{13}N . Actually, in this cycle, the ^{12}C is neither created or destroyed, but acts as a catalyst to aid the fusion process.

As already said, the net process is:



as in the proton-proton chain, with the same Q-value.

From Fig. 1.2 it can be seen that the CNO cycle is actually composed by two sub-cycles, the Carbon-Nitrogen (C-N) and the Nitrogen-Oxygen (N-O) cycles, sharing the reactions:



which determine the overall cycle rate.

The carbon cycle can proceed more rapidly than the pp-chain because it has no analogue of the deuterium bottleneck. However, the Coulomb barrier is 6 to 7 times higher for proton reactions with carbon and nitrogen than for proton-proton reactions and therefore the CNO cycle will be dominant only at relatively high temperatures, when additional thermal energy can increase the probability to penetrate the Coulomb barrier.

Actually, as it can be seen in Fig. 1.3, the CNO cycle dominates over the pp chain only if the temperature exceeds 1.8×10^7 K that is a power generation of 10^{-3} W/kg roughly. For the sun, this condition is not met, and the CNO cycle contributes only 1.5% to the total neutrino production.

1.3.3 The Standard Solar Model

The calculation of solar neutrino fluxes for both the pp chain and the CNO cycle depends on many factors such as the solar temperature, relative abundance of elements, nuclear reaction rates as well as the hydrodynamics of the solar interior. This calculation was pioneered by John N. Bahcall and co-workers, and subsequently performed by other groups as well.

1.3 Solar Neutrinos

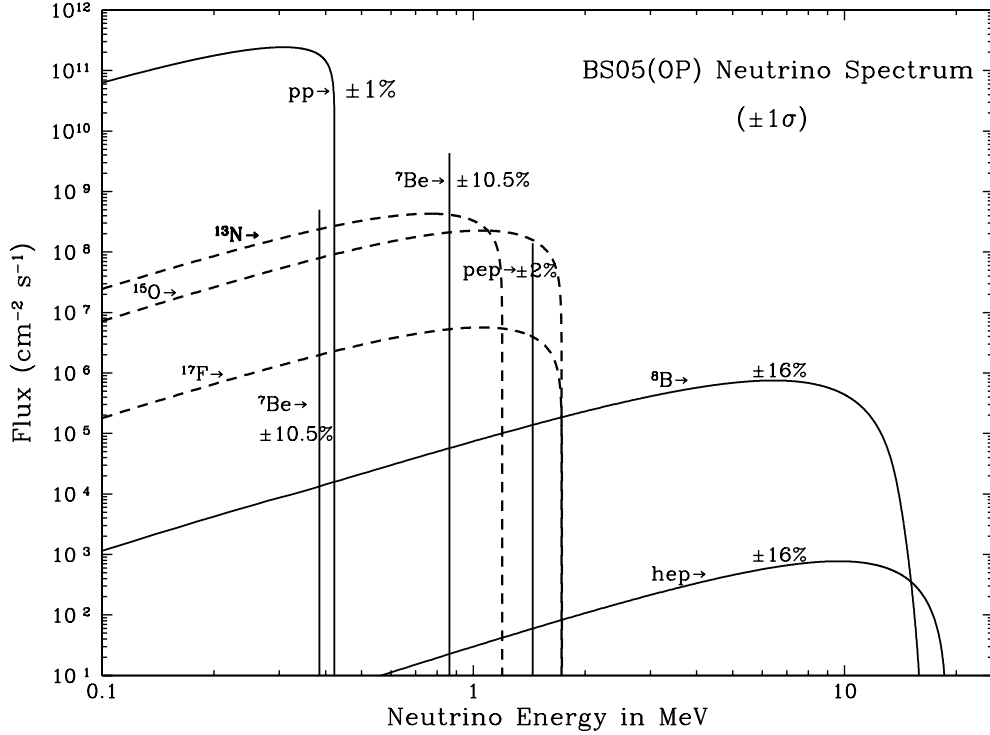


Figure 1.4: Solar neutrino fluxes on the earth's surface (Ref. [13, 14]): the neutrinos originated in the pp-chain with solid lines; the neutrinos originated in the CNO cycle with dashed lines. For the continuous spectra, the unit is $\text{cm}^{-2} \text{s}^{-1} \text{MeV}^{-1}$; for the discrete lines, the plot unit is $\text{cm}^{-2} \text{s}^{-1}$.

Since according to the net reaction (Eq. 1.7), two neutrino shares the total ${}^4\text{He}$ binding energy of $E({}^4\text{He}) \simeq 28 \text{ MeV}$, a rough calculation of the order of magnitude of the total neutrino flux on earth gives:

$$\Phi \simeq \frac{L_{\odot}}{4\pi d_{\text{se}}^2 \times \frac{1}{2} E({}^4\text{He})} \simeq 6 \times 10^{10} \nu \text{ cm}^{-2} \text{ s}^{-1}, \quad (1.8)$$

where L_{\odot} is the solar luminosity ($L_{\odot} = 4 \times 10^{33} \text{ erg/s}$), and d_{se} is the sun-to-earth distance ($d_{\text{se}} = 1.5 \times 10^{13} \text{ cm}$). As already discussed in Sec. 1.3.1, the main contribution to the solar neutrino flux comes from the pp reaction products so it is very reasonable to estimate the pp neutrino flux on earth to be about $10^{10} \nu \text{ cm}^{-2} \text{ s}^{-1}$ (see also Fig. 1.4). In order to calculate the effective flux for each neutrino belonging to either the pp chain or the CNO cycle, a solar model is needed.

A stellar model is a solution to the evolutionary equation of a star and its basic assumption is that the gravitational contraction and the radiative pressure from the thermonuclear reaction exactly counterbalance each other.

The Standard Solar Model (SSM) is a stellar model tailored on our closest and best known star, the sun. The SSM gives a quantitative description of the sun and it is based upon results of experimental observations, laboratory measurements of nuclear reactions cross-sections and theoretical predictions. Other basic assumptions are: spherical symmetry, hydrostatic and thermal equilibrium, equation of state of an ideal gas, and present surface abundances of elements similar to the estimated primordial composition. The boundary conditions and main inputs to the model can be summarized as:

- the solar luminosity;
- the solar age;
- the solar mass;
- the solar radius;
- the initial elemental abundances (the *metallicity*³);
- the nuclear parameters.

Inputs are also provided by the cross sections and energies of the nuclear reactions involved, the opacity of the star, and its isotopic abundances. The evolution equation then outputs, among other quantities, the energy spectrum and fluxes of all the emitted neutrinos.

In the last years, a real controversy over the solar chemical composition, the so-called *solar metallicity problem* arose. Originally the adopted elemental abundances was the one derived from the so-called *high metallicity* hypothesis (Ref [15]). Nevertheless, starting from early 2000's, a set of improved measurements of the elemental abundances on the sun surface has suggested to reduce the content of heavier elements such as carbon, nitrogen and so on; this is the origin of the so-called *low metallicity* hypothesis (Ref. [16, 17]) which today is a widely accepted alternative scenario to that of the high metallicity. Changing the input abundances causes a change in the prediction of the neutrino fluxes which is more or less relevant depending on the particular source. More refined calculation are in progress and the solar metallicity controversy is still an open question in the solar physics field.

³In astrophysics, the metallicity of an object is the fraction of chemical elements other than hydrogen and helium.

1.3 Solar Neutrinos

SOLAR NEUTRINO FLUXES - SHP11

ν Flux	High Metallicity	Low Metallicity	Difference %
pp	5.98(1 \pm 0.006)	6.03(1 \pm 0.006)	0.8
pep	1.44(1 \pm 0.012)	1.47(1 \pm 0.012)	2.1
hep	8.04(1 \pm 0.30)	8.31(1 \pm 0.30)	3.4
^7Be	5.00(1 \pm 0.07)	4.56(1 \pm 0.07)	8.8
^8B	5.58(1 \pm 0.14)	4.59(1 \pm 0.14)	17.7
^{13}N	2.96(1 \pm 0.14)	2.17(1 \pm 0.14)	26.7
^{15}O	2.23(1 \pm 0.15)	1.56(1 \pm 0.15)	30.0
^{17}F	5.52(1 \pm 0.17)	3.40(1 \pm 0.16)	38.4

Table 1.2: Neutrino fluxes as predicted by the SHP11 Solar model (Ref. [18]) having as input the GS98 high metallicity solution (Ref. [15]) and the AGSS09 low metallicity solution (Ref. [17]). The percentage difference among the two predictions is indicated. The fluxes are given in units of 10^{10} (pp), 10^9 (^7Be), 10^8 (pep, ^{13}N , ^{15}O), 10^6 (^8B , ^{17}F) and 10^3 (hep) $\text{cm}^{-2} \text{s}^{-1}$. Asymmetric uncertainties have been averaged.

The real problem is however due to the fact that, if the low metallicity abundances are given as input, the solar model fails to reproduce some of the helioseismological observables, like the speed of sound on the sun surface. On the other hand, the internal structure predicted by the solar models which have as input the high metallicity abundances, is in exceptional agreement with the same helioseismological measurements. Nowadays, mainly for this reason, the most used Standard Solar Model is still the one computed assuming the high metallicity elemental abundances. But, in this case, a disagreement with measured metal abundances remains.

The work presented in this Ph.D. thesis is based on the Standard Solar Model (Ref. [18]) recently published by Aldo Serenelli, William Haxton and Carlos Peña Garay. This solar model, hereafter called SHP11, uses newly analyzed nuclear fusion cross sections and, among many other quantities, predicts the different solar neutrinos fluxes according to the high (GS98, Ref. [15]) or low (AGSS09, Ref. [17]) metallicity hypothesis.

The predicted neutrino fluxes on earth are listed in Tab. 1.2, with their associated theoretical uncertainties: the second and third columns show the neutrino fluxes calculated in the high and low metallicity hypothesis respectively.

The maximum difference between the two predictions is found for the CNO neutrinos (about 30%). Also the ${}^7\text{Be}$ and the ${}^8\text{B}$ neutrino fluxes change significantly (8.8% and 17.7% respectively), while pp and pep neutrinos are basically unaffected.

1.4 Other sources of neutrinos

Solar neutrinos are not the only source of neutrinos in the universe: there are many different processes, natural or anthropic, which can yield neutrinos production.

In general, neutrinos can be classified according to their sources. In addition to solar neutrinos, there can be:

- reactor neutrinos,
- accelerator neutrinos,
- geologic neutrinos (the geo-neutrinos),
- atmospheric neutrinos,
- Big Bang neutrinos (the relic neutrinos),
- supernovae neutrinos.

The first two categories are anthropic while the others have natural origin.

Nuclear reactors are the major source of human-generated neutrinos. Anti-neutrinos are emitted in the beta-decay of neutron-rich daughter fragments in the fission process. The average nuclear fission releases about 200 MeV of energy, of which roughly 4.5% is radiated away as anti-neutrinos. The anti-neutrino energy spectrum depends on the degree to which the fuel is burned (for instance, ${}^{239}\text{Pu}$ fission anti-neutrinos on average have slightly more energy than those from ${}^{235}\text{U}$ fission), but in general, the detectable anti-neutrinos from fission have a peak energy between about 3.5 and 4 MeV, with a maximal energy of about 10 MeV (Ref. [19]).

Some particle accelerators have been used to make neutrino beams, the so-called accelerator neutrinos. The most common technique is to smash protons onto a fixed target, producing charged pions or kaons. These unstable particles are then magnetically focused into a tunnel where they decay, emitting neutrinos while in flight.

For what concerns the natural sources, neutrinos are part of the natural background radiation in the crust and mantle of the earth. In particular, the decay chains of ${}^{238}\text{U}$

1.5 Neutrino Oscillation

and ^{232}Th isotopes, as well as ^{40}K , include beta decays which emit anti-neutrinos, the so-called geo-neutrinos (see also Sec. 2.8.5).

Atmospheric neutrinos result from the interaction of cosmic rays with nuclei in the earth's atmosphere, creating showers of particles, many of which are unstable and produce neutrinos when decaying.

The relic neutrinos are defined as the background of low energy neutrinos left over from the Big Bang in our universe.

Neutrinos are also an important product of Type Ib, Ic and Type II supernovae. In such events, the density at the core becomes so high (10^{17} kg/m^3) that protons and electrons combine to form a neutron and an electron neutrino. A second and more important neutrino source is the thermal energy ($3 \times 10^{53} \text{ erg}$) of the newly formed neutron core, which is dissipated via the formation of neutrino - anti-neutrino pairs of all flavors (Ref. [20]). Most of the energy produced in supernovae is thus radiated away in the form of a burst of neutrinos.

1.5 Neutrino Oscillation

Regardless of their origin, neutrinos can only be produced and detected via weak interactions, namely, with a definite flavor.

However, if neutrinos are massive, the states of definite flavor may not coincide with states of definite mass. Then, the neutrino beam produced is a superposition of different mass eigenstates. As the beam propagates, its components evolve differently so that the probability of finding different flavor eigenstates in the same beam varies with distance, hence the oscillation phenomenon pointed out by B. Pontecorvo.

If neutrinos have masses, in general, the flavor eigenstates ν_α , are a superposition of mass eigenstates ν_i with different masses m_i :

$$|\nu_\alpha\rangle = \sum_{i=1}^n U_{\alpha i}^* |\nu_i\rangle, \quad (1.9)$$

where n is the number of light neutrino species and U is the mixing matrix ($U \rightarrow U^*$ for $\nu \rightarrow \bar{\nu}$).

For simplicity, one can assume the same 3-momentum \mathbf{p} for the different components in the neutrino beam. Since their masses are different, the energies of these components are also different:

$$E_i = \sqrt{\mathbf{p}^2 + m_i^2}.$$

After travelling a distance L or equivalently, for relativistic neutrinos, a time t , a neu-

trino originally produced with flavor α evolves as:

$$|\nu_\alpha(t)\rangle = \sum_{i=1}^n U_{\alpha i}^* |\nu_i(t)\rangle. \quad (1.10)$$

In defining $|\nu_\alpha(t)\rangle$, we reasonably assume that the neutrinos ν_α are stable particles. Thus, at any time t , the probability of finding a ν_β in the original ν_α beam is:

$$\begin{aligned} P_{\alpha\beta} &= |\langle \nu_\beta | \nu_\alpha(t) \rangle|^2 = \sum_{i=1}^n \sum_{j=1}^n U_{\alpha i}^* U_{\beta j} \langle \nu_j | \nu_i(t) \rangle^2 \\ &= \sum_{i=1}^n \sum_{j=1}^n |U_{\alpha i} U_{\beta i}^* U_{\alpha j}^* U_{\beta j}| \cos[(E_i - E_j)t - \varphi_{\alpha\beta ij}], \end{aligned} \quad (1.11)$$

where E_i (m_i) is the energy (the mass) of the neutrino mass eigenstate ν_i and

$$\varphi_{\alpha\beta ij} = \arg(U_{\alpha i} U_{\beta i}^* U_{\alpha j}^* U_{\beta j}).$$

In all practical situations, neutrino are extremely relativistic so that it is possible to rewrite:

$$|p_i| \simeq |p_j| \equiv |\mathbf{p}| \simeq E \quad \Rightarrow \quad E_i \simeq |\mathbf{p}| + \frac{m_i^2}{2|\mathbf{p}|} + O(p^2).$$

Using the time evolution, $|\nu_i(t)\rangle = e^{-iE_i t} |\nu_i(0)\rangle$ and the ortogonality relation between the mass eigenstates $\langle \nu_j | \nu_i \rangle = \delta_{ij}$, we get the following transition probability:

$$P_{\alpha\beta} = \delta_{\alpha\beta} + 2 \sum_{i \neq j}^n \Im [U_{\alpha i} U_{\beta i}^* U_{\alpha j}^* U_{\beta j}] \sin(2 X_{ij}) - 4 \sum_{i \neq j}^n \Re [U_{\alpha i} U_{\beta i}^* U_{\alpha j}^* U_{\beta j}] \sin^2 X_{ij}, \quad (1.12)$$

where

$$X_{ij} = \frac{(m_i^2 - m_j^2)L}{4E} = 1.27 \frac{\Delta m_{ij}^2}{\text{eV}^2} \frac{L/\text{m}}{m/\text{MeV}}. \quad (1.13)$$

Here L is the distance between the production point of ν_α and the detection point of ν_β . The second sum in Eq. 1.12 (the Real part, \Re) is CP conserving while the first one (the Imaginary part, \Im) is CP violating and has opposite sign for neutrinos and anti-neutrinos.

The transition probability in Eq. 1.12 shows an oscillatory behavior with amplitudes that are proportional to elements in the mixing matrix, and with *oscillation lenght*:

$$L_{ij}^{\text{osc}} = \frac{4\pi E}{\Delta m_{ij}^2}. \quad (1.14)$$

1.5 Neutrino Oscillation

The oscillation length gives a distance scale over which the oscillation effects can be appreciable. Thus, as anticipated before, in order to undergo flavor oscillations, neutrinos must have different masses (i.e. $\Delta m_{ij}^2 \neq 0$) and they must mix (i.e. $U_{\alpha i} U_{\beta i} \neq 0$).

A neutrino oscillation experiment is characterized by the typical neutrino energy E and by the source detector distance L . In order to be sensitive to a given value of Δm_{ij}^2 , the experiment has to be set up with $E/L \approx \Delta m_{ij}^2$ that is $L \simeq L_{ij}^{\text{osc}}$. Tab.1.3 reports the typical value of L , E for different types of neutrino sources and experiments.

Neutrino sources	L (m)	E (MeV)	Δm_{ij}^2 (eV ²)
Solar	10^{10}	$10^{-1} - 10$	10^{-10}
Atmospheric	$10^4 - 10^7$	$10^2 - 10^5$	$10^{-4} - 10^{-1}$
Reactor	SBL	$10^2 - 10^3$	$10^{-3} - 10^{-2}$
	LBL	$10^4 - 10^5$	$10^{-5} - 10^{-4}$
Accelerator	SBL	10^2	$< 10^{-1}$
	LBL	$10^5 - 10^6$	$10^{-3} - 10^{-2}$

Table 1.3: Characteristic values of L and E for various neutrino sources and experiments, and the corresponding ranges of Δm_{ij}^2 to which they can be most sensitive. Acronym SBL means Short BaseLine, LBL means Long BaseLine

In general, if $E/L \gg \Delta m_{ij}^2$ ($L \ll L_{ij}^{\text{osc}}$), the oscillation phase does not have time to give an appreciable effect because $\sin^2 X_{ij} \ll 1$. Conversely, if $L \gg L_{ij}^{\text{osc}}$, the oscillating phase goes through many cycles before the detection and is averaged to $\langle \sin^2 X_{ij} \rangle = 1/2$. Maximum sensitivity to the oscillation phase and therefore to Δm_{ij}^2 is obtained when the set up is such that:

1. $E/L \approx \Delta m_{ij}^2$;
2. the energy resolution of the experiment is good enough, $\Delta E \ll L \Delta m_{ij}^2$;
3. the experiment is sensitive to different values of L .

1.5.1 Vacuum oscillations

In order to study the propagation of neutrino flavor eigenstates in vacuum, it is useful to start with the analysis of a two-neutrino case and then to extend the reasoning to the three-neutrino case. It is convenient to analyze the oscillation data in terms of the

simplest assumption that there is oscillation between two neutrinos only. In this case, the mixing matrix U depends on a single parameter θ and has a particularly simple form:

$$U = \begin{pmatrix} \cos \theta & \sin \theta \\ -\sin \theta & \cos \theta \end{pmatrix}, \quad (1.15)$$

and there is a single mass-squared difference Δm^2 . Then, the $P_{\alpha\beta}$ in Eq. 1.12 takes the well known form:

$$P_{\alpha\beta} = \delta_{\alpha\beta} - (2\delta_{\alpha\beta} - 1) \sin^2 2\theta \sin^2 X. \quad (1.16)$$

That is, for a given flavor of neutrino, a survival (conversion) probability:

$$P_{\alpha\alpha} = 1 - \sin^2 2\theta \sin^2 X, \quad (1.17)$$

$$P_{\alpha\beta} = \sin^2 2\theta \sin^2 X \quad (\alpha \neq \beta). \quad (1.18)$$

The physical parameter space is covered with $\Delta m^2 \geq 0$ and $0 \leq \theta \leq \frac{\pi}{2}$. Anyway, there is a two-fold discrete ambiguity in the interpretation of $P_{\alpha\beta}$ in terms of neutrino mixing: the two sets of different physical parameters $(\Delta m^2, \theta)$ and $(\Delta m^2, \frac{\pi}{2} - \theta)$ give the same transition probability in vacuum. One cannot tell from a measurement in vacuum whether the larger component of ν_α resides in the heavier or lighter neutrino mass eigenstate. This symmetry is lost when there are more than two neutrinos mixed in the neutrino evolution and/or when neutrinos travel through regions of dense matter.

In real world, there are (at least) three neutrinos so the two-generation analysis previously done holds strictly only in extreme cases, e.g. when one of the neutrinos is effectively decoupled from the other two. A formula similar to Eq. 1.16 can be derived in the realistic cases when all three neutrinos mix with one another.

In this case, the mixing matrix can be conveniently parametrized as the product of four sub-matrix:

$$U = \begin{pmatrix} 1 & 0 & 0 \\ 0 & c_{23} & s_{23} \\ 0 & -s_{23} & c_{23} \end{pmatrix} \cdot \begin{pmatrix} c_{13} & 0 & s_{13} e^{-i\delta_{CP}} \\ 0 & 1 & 0 \\ -s_{13} e^{-i\delta_{CP}} & 0 & c_{13} \end{pmatrix} \cdot \begin{pmatrix} c_{12} & s_{12} & 0 \\ -s_{12} & c_{12} & 0 \\ 0 & 0 & 1 \end{pmatrix} \cdot U_{MAJ} \quad (1.19)$$

where:

$$U_{MAJ} = \begin{pmatrix} e^{i\eta_1} & 0 & 0 \\ 0 & e^{i\eta_2} & 0 \\ 0 & 0 & 1 \end{pmatrix}, \quad c_{ij} = \cos \theta_{ij} \quad \text{and} \quad s_{ij} = \sin \theta_{ij}.$$

The angles θ_{ij} can be taken without loss of generality as $\theta_{ij} \in [0, \pi/2]$ and the phases $\delta_{CP}, \eta_1, \eta_2 \in [0, 2\pi]$.

1.5 Neutrino Oscillation

In particular, if there are only three Majorana neutrinos, U is a 3×3 matrix which relies on six independent parameters: three mixing angle (θ_{12} , θ_{23} , θ_{13}) and three phases (δ_{CP} , η_1 , η_2).

In the case of three Dirac neutrinos, the Majorana phases η_1 and η_2 are absorbed in the neutrino states and therefore the number of physical phases is one, similarly to the Cabibbo-Kobayashi-Maskawa (CKM) matrix for quarks. In any case, the phases η_1 and η_2 never appear in oscillation phenomena since they cancel out in UU^* products.

For Dirac neutrinos, the mixing matrix U is called the Pontecorvo-Maki-Nagakawa-Sakata (PMNS) matrix and takes the well known form:

$$U = \begin{pmatrix} c_{12} c_{13} & s_{12} c_{13} & s_{13} e^{-i\delta_{CP}} \\ -s_{12} c_{23} - c_{12} s_{13} s_{23} e^{-i\delta_{CP}} & c_{12} c_{23} - s_{12} s_{13} s_{23} e^{-i\delta_{CP}} & c_{13} s_{23} \\ s_{12} s_{23} - c_{12} s_{13} c_{23} e^{-i\delta_{CP}} & -c_{12} s_{23} - s_{12} s_{13} c_{23} e^{-i\delta_{CP}} & c_{13} c_{23} \end{pmatrix}, \quad (1.20)$$

commonly parametrized in its very compact form:

$$U = \begin{pmatrix} U_{e1} & U_{e2} & U_{e3} \\ U_{\mu1} & U_{\mu2} & U_{\mu3} \\ U_{\tau1} & U_{\tau2} & U_{\tau3} \end{pmatrix}. \quad (1.21)$$

Using the above mixing matrix (Eq. 1.20) inside Eq. 1.12 and assuming the so-called *normal hierarchy* ($\Delta m_{31}^2 \gg \Delta m_{21}^2$), one gets the following expression of the survival probability in vacuum for an electron neutrino ν_e :

$$P_{ee} = \cos^4 \theta_{13} \left[1 - \sin^2 2\theta_{12} \sin^2 \left(\frac{\Delta m_{21}^2}{4E} L \right) \right] + \sin^4 \theta_{13}. \quad (1.22)$$

If θ_{13} happens to be very small, the resulting P_{ee} coincides with the survival probability obtained in Eq. 1.17 for the two flavor case.

1.5.2 Matter-enhanced oscillations

When neutrinos propagate in dense matter, the interactions with the medium affect their flavor evolution (Ref. [21]). The basic reason for this behavior is simple: normal matter has electrons but no muons or taus at all. Thus, if a ν_e beam goes through matter, it can undergo to both charged and neutral current interactions with electrons. On the other hand, low-energy ν_μ or ν_τ interact with the electron only via neutral current, so their interaction is different in magnitude than that of the ν_e .

The evolution equation for n ultrarelativistic neutrinos propagating in matter, written in the mass basis, can be cast in the following form:

$$i \frac{d\vec{\nu}}{dx} = H \vec{\nu} \quad \text{and} \quad H = H_m + U V U^\dagger, \quad (1.23)$$

where $\vec{\nu} = (\nu_1, \nu_2, \dots, \nu_n)^T$, H_m is the Hamiltonian for the kinetic energy and V is the effective potential that describes the coherent forward interactions of the neutrinos with matter in the flavor basis.

In 1985, S. Mikheyev and A. Smirnov found out a very relevant feature of oscillation in matter: they discovered that, under particular conditions, the matter effect can lead to a resonant flavor transition (Fig. 1.5). This effect, known as MSW mechanism, is a key-point in explaining the solar neutrinos flavor oscillation (see Sec. 1.3).

For sake of simplicity, as we did in studying vacuum oscillations, the analysis is first reported in the simplest case of two-flavors and then extended to the three-flavors case. We study the evolution of ν_e in a medium with electrons, protons and neutrons with corresponding n_e , n_p and n_n number densities. We start considering the effect of the charged current interactions which only involve electron neutrinos (and anti-neutrinos of course) and the electrons of the medium. The effective charged current (CC) Hamiltonian can be parametrized as a contribution to the ν_e potential energy:

$$V_{CC} = \pm \sqrt{2} G_F n_e, \quad (1.24)$$

where G_F is the Fermi coupling constant and n_e the electron number density; the sign is positive for neutrinos and negative for anti-neutrinos. A detailed derivation of the matter potential can be found, for example, in Ref. [22].

For ν_μ and ν_τ the potential due to its CC interactions is zero for most media since neither μ or τ particles are present. In the same way as for V_{CC} , one can derive the effective potential for any active neutrino due to the neutral current (NC) interactions:

$$V_{NC} = \frac{\sqrt{2}}{2} G_F [-n_e (1 - 4\sin^2 \theta_w) + n_p (1 - 4\sin^2 \theta_w) - n_n]. \quad (1.25)$$

In neutral matter $n_e = n_p$ so the contributions from electrons and protons cancel each other and only the neutron contribution is left:

$$V_{NC} = -\frac{\sqrt{2}}{2} G_F n_n. \quad (1.26)$$

So, the evolution equation (Eq. 1.23) for the three SM active neutrinos with purely SM

1.5 Neutrino Oscillation

interactions in a neutral medium with electrons, protons and neutrons with $U^\nu = U$, yields a global effective potential V which can be written as:

$$V = \text{diag} \left(\pm\sqrt{2} G_F n_e(x), 0, 0 \right) \equiv \text{diag} (V_{CC}, 0, 0) . \quad (1.27)$$

The sign $+$ (or $-$) refers to neutrinos (or anti-neutrinos) and $n_e(x)$ is the electron number density in the medium, which in general changes along the neutrino trajectory and so does the potential. Since the neutral potential V_{NC} is the same for all flavors, it does not affect oscillations. In fact, V_{NC} is flavor diagonal and therefore can be eliminated from the evolution equation as it only contributes to an overall phase which is unobservable.

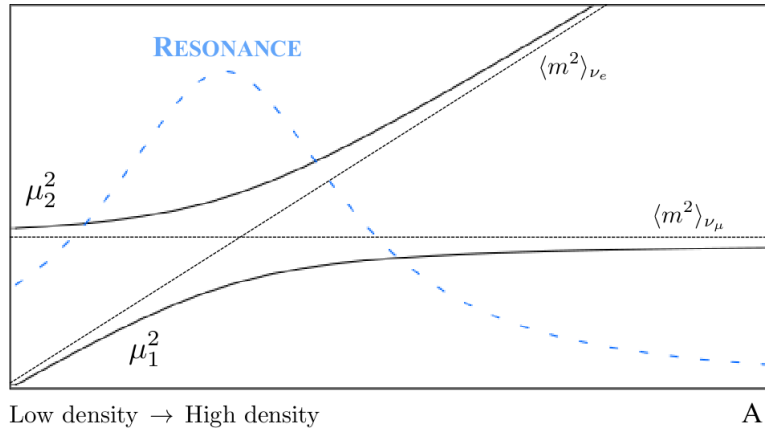


Figure 1.5: The effective masses in matter ($\mu_{1,2}^2$, Eq. 1.28) for two neutrino flavors as a function of the density A (Eq. 1.29). The solid lines are the instantaneous effective masses, the dashed lines are the expectation values of squared mass for the states ν_e and ν_μ . For the plot it is assumed $\theta = 0.3$ and the vertical scale is arbitrary.

The instantaneous mass eigenstates in matter, ν_i^m , are the eigenstates of H for a fixed value of x and are related to the flavor basis by:

$$\vec{\nu} = \tilde{U}(x) \vec{\nu}^m,$$

while $\mu_i(x)^2/(2E)$ are the corresponding instantaneous eigenvalues, being $\mu_i(x)$ the instantaneous effective neutrino masses.

In the simplest case of the evolution of a neutrino state which is an admixture of only two neutrino species $|\nu_\alpha\rangle$ and $|\nu_\beta\rangle$, the instantaneous effective neutrino mass can be cast as:

$$\mu_{1,2}^2 = \frac{1}{2} \left[m_1^2 + m_2^2 + A \pm \frac{\Delta m_{21}^2}{2} \sqrt{\sin^2 2\theta + (\cos 2\theta - x)^2} \right], \quad (1.28)$$

where, for the sake of convenience, we defined:

$$A = 2\sqrt{2} G_F n_e E = 2E (V_\alpha - V_\beta) \quad \text{and} \quad x = \frac{A}{\Delta m_{12}^2}. \quad (1.29)$$

The behaviour of μ_1^2 and μ_2^2 as functions of A are shown schematically in Fig. 1.5.

Propagation through matter is hence determined by these two eigenvalues, with the corresponding eigenstates $\tilde{\nu}_\alpha$ related to the flavor eigenstates as follows:

$$\tilde{U} = \begin{pmatrix} \cos \theta_m & \sin \theta_m \\ -\sin \theta_m & \cos \theta_m \end{pmatrix} \implies \begin{pmatrix} \nu_e \\ \nu_\mu \end{pmatrix} = \begin{pmatrix} \cos \theta_m & \sin \theta_m \\ -\sin \theta_m & \cos \theta_m \end{pmatrix} \begin{pmatrix} \tilde{\nu}_1 \\ \tilde{\nu}_2 \end{pmatrix}. \quad (1.30)$$

The angle θ_m is the instantaneous mixing angle in matter and it is given by:

$$\tan 2\theta_m = \frac{\Delta m^2 \sin 2\theta}{\Delta m^2 \cos 2\theta - A}. \quad (1.31)$$

Notice that, for a given sign of A (depending on the composition of the medium and on the flavor composition of the neutrino state), the mixing angle in matter may be either larger or smaller than in vacuum. Thus, the octant symmetry present in vacuum oscillations is broken by matter potentials. Generically matter effects are important when for some of the states, the corresponding potential difference factor A is comparable to their mass difference term $\Delta m^2 \cos 2\theta$. Most relevant, the mixing angle $\tan \theta_m$ changes sign if in some point along its path the neutrino passes by some matter density region verifying the *resonance condition*:

$$A_R = \Delta m^2 \cos 2\theta. \quad (1.32)$$

If in vacuum the lightest mass eigenstate has a larger projection on the flavor α while the heaviest has it on the flavor β , once inside a matter potential with $A > A_R$ the opposite holds. Thus, for a neutrino system which is travelling across a monotonically varying matter potential, the dominant flavor component of a given mass eigenstate changes when crossing the region with $A = A_R$.

1.5 Neutrino Oscillation

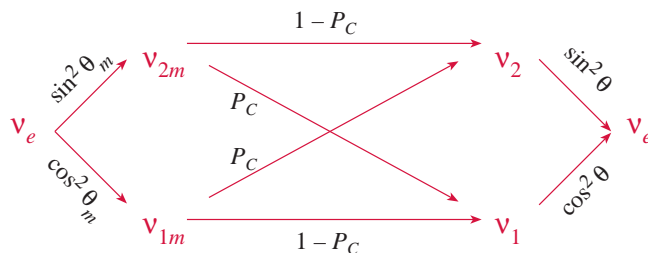


Figure 1.6: Non-adiabatic evolution. Propagation of a neutrino from the sun to the earth.

This phenomenon is known as *level crossing* and it is indicated in Fig. 1.5. For constant or slowly enough varying matter potential, the instantaneous mass eigenstates ν_1^m behave approximately as energy eigenstates and they do not mix in the evolution. This phenomenon is called *adiabatic transition*. On the contrary, when the matter potential experiences a considerable variation, the instantaneous mass eigenstates mix along the neutrino path so there can be *level-jumping* (see Fig. 1.6) and the evolution is named *non-adiabatic*.

1.5.3 The MSW effect for solar neutrinos

In order to study solar and supernova neutrinos, it is useful to study the oscillation probabilities of neutrinos that are produced in the core of the star (where matter effects are important) and escape into the vacuum (where matter effects are negligible): at some intermediate point, matter effects can be resonant (MSW mechanism). Let the star be the sun and, once again, let assume the case of two neutrino generations. Briefly, solar neutrinos behave as follows:

- ν_e are produced in the core of the sun ($r \approx 0$). The probability of ν_e being ν_{1m} or ν_{2m} are $\cos^2 \theta_m$ and $\sin^2 \theta_m$ respectively. When matter effects are dominant, $\nu_e \simeq \nu_{2m}$ i.e. $\sin^2 \theta_m = 1$.
- The oscillation wave-length λ is much smaller than the solar radius r_{sun} . Therefore neutrinos propagate for many oscillation wave-lengths: the phase averages out so that we have to combine probabilities instead of amplitudes. If the density changes very slowly, that is the adiabatic approximation case, each neutrino mass eigenstate will remain the same. Otherwise neutrinos will flip to the other mass eigenstate with some level-crossing probability P_C (see Fig. 1.6).

So for ν_{2m} , and equally for ν_{1m} , it follows that:

$$\nu_{2m}(r \approx 0) \text{ evolves to } \begin{cases} \nu_{2m}(r \approx r_{\text{sun}}) = \nu_2 & \text{with probability } 1 - P_C; \\ \nu_{1m}(r \approx r_{\text{sun}}) = \nu_1 & \text{with probability } P_C. \end{cases}$$

- Neutrinos propagate from the sun to the earth, and possibly inside the earth before reaching the detector. For simplicity, here we ignore earth matter effects.
- Finally, the ν_2 (or ν_1) is detected as ν_e with probability $\sin^2 \theta$ (or $\cos^2 \theta$).

Combining all these probabilities, as summarized in Fig. 1.6, one gets:

$$P_{ee} = \frac{1}{2} + \left(\frac{1}{2} - P_C \right) \cos 2\theta \cos 2\theta_m, \quad (1.33)$$

where θ_m is the effective mixing angle at the production point. It is worth to analyze Eq. 1.33 in few special cases:

- a) When matter effects are negligible, $\theta_m = 0$ and $P_C = 0$. This is the case of averaged vacuum oscillations and it is realized for solar neutrinos at lower energies.

$$P_{ee} = 1 - \frac{1}{2} \sin^2 2\theta. \quad (1.34)$$

- b) When matter effects dominate, the heavier effective neutrino mass eigenstate is $\nu_{2m}(r \approx 0) \simeq \nu_e$ and $\theta \ll 1$ that is $\cos 2\theta_m \simeq -1$.

$$P_{ee} = P_C. \quad (1.35)$$

- c) When neutrinos propagate adiabatically ($P_C = 0$) and $\theta \ll 1$:

$$P_{ee} = \sin^2 \theta. \quad (1.36)$$

This is the case of solar neutrinos at higher energies.

- d) When neutrinos propagate in the extreme non-adiabatic limit and $\theta \ll 1$:

$$P_{ee} = 1 - \frac{1}{2} \sin^2 2\theta. \quad (1.37)$$

The value of $P_C = \cos^2 \theta$ can be computed by considering very dense matter that abruptly terminates in vacuum. The produced neutrino $\nu_e \simeq \nu_{2m}$ does not change flavor at the transition region since it is negligibly short. Therefore $P_C = |\langle \nu_e | \nu_1 \rangle|^2 = \cos^2 \theta$. To understand the reason for which in this particular

1.6 Solar neutrino experiments

case P_{ee} is equal to averaged vacuum oscillations, it is useful to follow the neutrino path: matter effects are very large and block oscillation around and after the production point until, suddenly, they become negligible.

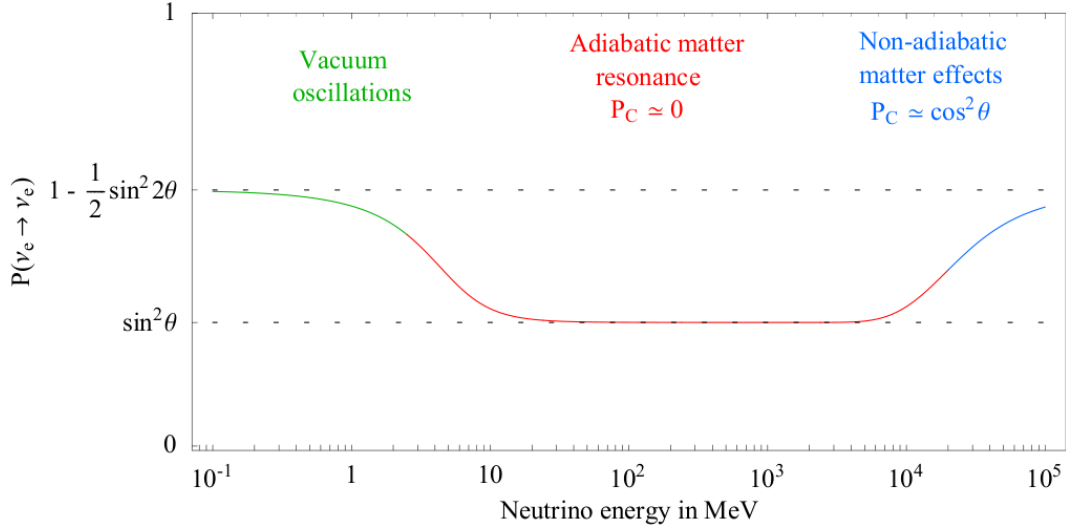


Figure 1.7: Behavior of P_{ee} that illustrates the limiting regimes a, c, d previously discussed. At lower energies, matter effects are negligible (a); at intermediate energies, matter effects are dominant and adiabatic (c); at higher energies, the MSW resonance is no longer adiabatic (d). The numerical example corresponds to solar oscillations. Absorption is neglected. (Ref. [23]).

The above derivation can be easily extended to the case of three neutrino generations (with the substitution $V \rightarrow V \cos^2 \theta_{13}$) and the analytical expression describing the full evolution in three neutrino species is:

$$P_{ee}^{3\nu} = \cos^4 \theta_{13} P_{ee}^{2\nu} + \sin^4 \theta_{13}. \quad (1.38)$$

From Eq. 1.38, it is clear that the third flavor enters in the survival probability computation only via the fourth power of sin and cos of θ_{13} . $P_{ee}^{2\nu}$ is the survival probability of an electron neutrino as calculated with the two neutrino species approximation.

1.6 Solar neutrino experiments

An ideal neutrino detection should measure, at the same time, the neutrino energy, direction and flavour.

However, in practice, every neutrino experiment has to find a compromise between the various and contrasting needs, e.g. between a very high resolution and a very high fiducial volume.

The main difficulty experienced by physicists, when trying to detect solar neutrino, is their very low cross section due to their low energy. The strategy to overcome this obstacle was (and still is today) the requirement of a large volume detector, combined with a high detection sensitivity, a low background environment and a deep underground location in order to shield the experiments from cosmic rays.

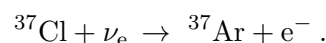
Until today, only few experiments succeeded in matching all the requirements and in detecting solar neutrinos; they can all be classified in two types: the *radiochemical* and the *real-time* experiments.

- **Radiochemical Experiments.** Based on neutrino capture reaction by specific isotopes. The reaction products are the chemically separated from the target mass and counted through low background proportional chambers. This technique is sensitive to the total capture rate above a certain threshold (depending on the chosen isotope) but does not convey any information on the neutrino exact timing and energy spectrum. Experiments belonging to this category are Homestake, SAGE and GALLEX/GNO.
- **Real-time Experiments.** Essentially water Čerenkov or liquid scintillator detectors, this kind of experiments reveals neutrinos through their elastic scattering on the electrons of the target, or the inverse beta decay reaction on deuterium which emits energetic electrons or inelastic scattering on deuterium producing free neutrons. Such experiments supply information about the energy, time and, for water Čerenkov only, direction of neutrinos. Experiments belonging to this category are Borexino, Super Kamiokande and SNO.

Here it follows a brief review of the principal neutrino oscillation experiments.

The Homestake experiment

The first result on the detection of solar neutrinos was announced by Ray Davis Jr. and his collaborators from the Brookhaven laboratory in 1968 (Ref. [24]). In the gold mine of Homestake in Lead, South Dakota, they installed a detector consisting of ~ 615 tons of C_2Cl_4 where solar electron neutrinos were captured via the reaction:



1.6 Solar neutrino experiments

The energy threshold of this reaction is 0.814 MeV, so the relevant fluxes are the ones of ${}^7\text{Be}$ and ${}^8\text{B}$ neutrinos.

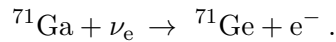
The average event rate measured (Ref. [25]) during the more than 20 years of operation is:

$$R_{\text{Cl}} = 2.56 \pm 0.23 \text{ SNU} \quad \rightarrow \quad \frac{R_{\text{Cl}}}{R_{\text{SSM}}^{\text{Cl}}} = 0.30 \pm 0.03 ,$$

where 1 SNU (Solar Neutrino Unit) = 10^{-36} captures/atom/sec, and $R_{\text{SSM}}^{\text{Cl}}$ is the expectation from the standard solar model.

The SAGE and GALLEX/GNO experiments

In the early 1990's two radiochemical experiments started taking data: SAGE (Soviet-American Gallium Experiment, Ref. [26]) and GALLEX (GALLium EXperiment, Ref. [27]). They both used ${}^{71}\text{Ga}$ as target for the reaction:



The SAGE detector was located in Baksan, Russia, and consisted of 30 tons (increased up to 57 tons starting from July, 1991) of liquid metallic gallium.

GALLEX was located in the national laboratory of Gran Sasso, Italy, and consisted of 30 tons of $\text{GaCl}_3\text{-HCl}$. The GALLEX program was completed in late 1997 and its direct successor, the GNO experiment (Gallium Neutrino Observatory, Ref. [28]), took data starting from spring 1998 to April 2003.

The special properties of a ${}^{71}\text{Ga}$ target consist in a low threshold (0.233 MeV) and a strong transition to the ground level of ${}^{71}\text{Ge}$ which gives a large cross section for the lowest energy solar neutrinos: the pp neutrinos.

The averaged event rate (Ref. [29, 30, 28]) measured by SAGE and GALLEX/GNO is:

$$R_{\text{Ga}} = 68.3 \pm 3.75 \text{ SNU} \quad \rightarrow \quad \frac{R_{\text{Ga}}}{R_{\text{SSM}}^{\text{Ga}}} = 0.52 \pm 0.03 ,$$

again, being 1 SNU (Solar Neutrino Unit) = 10^{-36} captures/atom/sec.

The Super Kamiokande experiment

The Super Kamiokande experiment is set in Kamioka, Japan, and it is a water Čerenkov detector that is able to detect in real time the electrons emitted from the water by the

elastic scattering (ES) of the solar neutrinos:

$$\nu_x + e^- \rightarrow \nu_x + e^-.$$

The scattered electrons produce Čerenkov light which is detected by photomultipliers. It is important to notice that, while the detection process in radiochemical experiments is a purely charged current (CC) interaction, the detection via elastic scattering goes through both the CC and neutral current (NC) interactions. Consequently, the ES detection process is sensitive to all the active neutrino flavors, although ν_e (the only CC scattering process) gives a contribution that is about 6 times larger than that of ν_μ or ν_τ due to the difference of the cross section.

Super Kamiokande (SK) started taking data in May 1996 and consists of 45000 tons of water (22500 fully usable for solar neutrino measurements) and so far it has analyzed its phase I, II and III.

The phase-I of the Super Kamiokande experiment (Ref. [31]) yielded a precise measurement of the solar neutrino flux. In spite of the loss of numerous photomultiplier tubes sustained in an accident, SK continued to collect data with reduced photo-cathode coverage and a higher energy threshold. Data collection and analysis methods had to be revised due to the loss of detector sensitivity. Super Kamiokande's phase II (Ref. [32]) ran from December 2002 to October 2005. The phase III (Ref. [33]) began in October 2006 and ended in August 2008 when the electronics were replaced.

The Super Kamiokande experiment has a detection threshold⁴ of 5 MeV and so, it can detect only the ^8B solar neutrinos (and the very small hep neutrino flux). Their results (Ref. [33]) are presented in terms of measured ^8B flux:

$$\Phi_{\text{SK}} = 2.32 \pm 0.04 (\text{stat}) \pm 0.05 (\text{syst}) \times 10^6 \text{ cm}^{-2} \text{ s}^{-1}, \quad \frac{\Phi_{\text{SK}}}{\Phi_{\text{SSM}}} = 0.41 \pm 0.01 .$$

The SNO experiment

The Sudbury Neutrino Observatory (SNO) was first proposed in 1987 and it started taking data in November 1999. The detector is located at the Creighton mine, near Sudbury in Canada, and it consists of a great sphere containing approximately 1000 tons of heavy water, D_2O , surrounded by photomultipliers. SNO reveals the Čerenkov light and it was designed in order to give a model independent test of the possible explanations of the observed deficit in the solar neutrino flux by having sensitivity to all flavors of active neutrinos and not just to the ν_e . This sensitivity is achieved because

⁴This is not the case of SK-II where the energy threshold increased to 7.5 MeV due to a large PMTs failure.

1.6 Solar neutrino experiments

energetic neutrinos can interact in the D₂O via three different reactions:

$$\begin{aligned} \text{CC} : \quad & \nu_e + \text{d} \rightarrow \text{p} + \text{p} + \text{e}^- \quad E_{\text{thr}} = 5 \text{ MeV} , \\ \text{NC} : \quad & \nu_x + \text{d} \rightarrow \text{n} + \text{p} + \nu_x \quad E_{\text{thr}} = 2.225 \text{ MeV} , \\ \text{ES} : \quad & \nu_x + \text{e}^- \rightarrow \nu_x + \text{e}^- , \end{aligned}$$

where $x = e, \mu, \tau$. The ES reaction though, is much more rare than the other two since it has a smaller cross section.

A peculiarity of SNO is its ability to directly test whether the deficit of solar ν_e is due to changes in the flavor composition of the solar neutrino beam, since the ratio CC/NC compares the number of ν_e interactions with those from all active flavors.

In its first year of operation, the SNO collaboration was concentrated on the measurement of the CC reaction rate (Ref. [34]) while in a following phase, after the addition of MgCl₂ salt to enhance the NC signal, it also performed a precise measurement of the NC rate (Ref. [35]). In the last phase, phase III, the salt was eliminated and a network of proportional counters filled with ³He was added with the purpose of directly measuring the NC rate (Ref. [36]) via the ³He(n,p)^H reaction.

At present, the SNO most precise determination of the solar fluxes yields (Ref. [37]):

$$\begin{aligned} \Phi_{\text{SNO}}^{\text{NC}} &= 5.54_{-0.31}^{+0.33} (\text{stat})_{-0.34}^{+0.36} (\text{syst}) \times 10^6 \text{ cm}^{-2} \text{ s}^{-1}, & \frac{\Phi_{\text{NCSNO}}}{\Phi_{\text{SSM}}} &\simeq 1.00 \pm 0.08, \\ \Phi_{\text{SNO}}^{\text{CC}} &= 1.67_{-0.04}^{+0.05} (\text{stat})_{-0.08}^{+0.07} (\text{syst}) \times 10^6 \text{ cm}^{-2} \text{ s}^{-1}, & \frac{\Phi_{\text{CCSNO}}}{\Phi_{\text{SSM}}} &= 0.29 \pm 0.02, \\ \Phi_{\text{SNO}}^{\text{ES}} &= 1.77_{-0.21}^{+0.24} (\text{stat})_{-0.10}^{+0.09} (\text{syst}) \times 10^6 \text{ cm}^{-2} \text{ s}^{-1}, & \frac{\Phi_{\text{NCSNO}}}{\Phi_{\text{SSM}}} &= 0.31 \pm 0.05. \end{aligned}$$

The Borexino experiment

The Borexino experiment is currently taking data at the Laboratori Nazionali del Gran Sasso in Abruzzo, Italy. Its main goal is the real-time measurement of the flux from the 0.862 MeV monoenergetic line of ⁷Be solar neutrinos, but Borexino reveals to be a versatile experiment and it also succeeded in measuring ⁸B solar neutrino flux, geoneutrinos and, recently, pep solar neutrinos.

Borexino employs a liquid scintillator that produces sufficient light to observe low energy event via the elastic scattering by electrons:

$$\nu_x + \text{e}^- \rightarrow \nu_x + \text{e}^- .$$

The reaction is sensitive to all neutrino flavors by the neutral current interaction, but

the cross section for ν_e is larger due to the combination of charged and neutral currents. A complete and detailed description of the Borexino detector and results can be found in Chap. 2.

1.7 Reactor neutrino experiments

Many experiments have searched for oscillation of electron anti-neutrinos produced at nuclear reactors. Neutrinos produced in nuclear reactors have energies similar to solar neutrinos, i.e. a few MeV, but the baselines of these experiments have ranged from tens of meters to over 100 km.

Due to the low energy, electrons are the only charged leptons which can be produced in the neutrino CC interaction. If the $\bar{\nu}_e$ oscillated to another flavor, its CC interaction could not be observed, therefore, oscillation experiments performed at reactors are basically disappearance experiments. They have the advantage that smaller values of Δm^2 can be accessed due to the lower neutrino beam energy.

A high precision observation of reactor neutrino oscillation has been made by the KamLAND experiment since 2002. KamLAND is a 1000 ton liquid scintillation detector currently operating in Kamioka mine in Japan. This underground site is located at an average distance (about 150-210 km) from the several Japanese nuclear plants.

In KamLAND, the three flavor survival probability ($P_{ee}^{3\nu}$), including matter effects, may be approximated as:

$$P_{ee}^{3\nu} = \cos^4 \theta_{13} P_{ee}^{2\nu} + \sin^4 \theta_{13} ,$$

where $P_{ee}^{2\nu}$ is the survival probability in matter for the two flavor mixing case.

For reactor anti-neutrinos studied at KamLAND, the matter effect in the Earth is not as large as for solar neutrinos. Assuming a constant rock density (2.7 g/cm^3), the two-neutrino survival probability is given by:

$$P_{ee}^{2\nu} = 1 - \sin^2 2\theta_{12_m} \sin^2 \left(\frac{1.27 \Delta m_{21_m}^2 L}{E} \right) ,$$

where L is the electron anti-neutrino flight distance in meters from the source to the detector, E is the $\bar{\nu}_e$ energy in MeV, and $\Delta m_{21_m}^2$ is in eV^2 , while θ_{12_m} and $\Delta m_{21_m}^2$ are the matter-modified mixing angle and mass splitting discussed in Sec. 1.5.2.

The KamLAND collaboration has recently published (Ref. [38]) new data with an improved statistics (total exposure of 3.49×10^{32} target-proton-year). In that paper, the electron survival probability is reconstructed in a 6 bin distribution according to

1.8 The global analysis of neutrino data

different values of the parameter x :

$$x = \frac{\langle \sin^2 2\theta_{12_m} \sin^2(\frac{1.27 \Delta m^2}{E \bar{\nu}_e} L) \rangle}{\sin^2 2\theta_{12}}.$$

1.8 The global analysis of neutrino data

The analysis which collects and combines all the results coming from the different types of experiments previously discussed, and tries to extract the maximum amount of information about the oscillation parameters of neutrinos is called *global analysis of neutrino data*. This analysis leads to favour or to exclude different regions of the $\tan^2 \theta_{12} - \Delta m_{21}^2$ space of parameters.

The first steps into this peculiar analysis were moved in early 1994 by G.L. Fogli and his collaborators (Ref. [39]) who consider

“the possible evidence of neutrino oscillations by analyzing simultaneously, in a well-defined hierarchical three-generation scheme, all the solar and atmospheric neutrino data [...] together with the constraints imposed by accelerator and reactor neutrino experiments [...] and includes the earth regeneration effect on solar neutrinos and the present theoretical uncertainties on solar and atmospheric neutrino fluxes.”

They found solutions and combined bounds in the parameter space of the neutrino masses and mixing angles, which were compatible with the whole set of experimental data and with their hierarchical assumption.

Since then, many different experiments started taking data and the scenario of the neutrino experimental results has enormously grown. Several global analysis were performed and refined by different groups and this yielded the definition of particular oscillation regimes corresponding to different values of oscillation parameters.

In the present work, we will mainly focus on the experimental contributions coming from solar neutrinos experiments. Therefore, we will analyze the range of parameters defined by:

$$\begin{aligned} \Delta m_{21}^2 : \quad & 10^{-12} \text{eV}^2 \leq \Delta m_{21}^2 \leq 10^{-3} \text{eV}^2, \\ \tan^2 \theta_{12} : \quad & 10^{-4} \leq \tan^2 \theta_{12} \leq 10. \end{aligned} \tag{1.39}$$

In Fig. 1.8, the regions of squared-mass splitting and mixing angle favored or excluded by various experiments are indicated. Referring to this plot, in the selected space of parameters, one can identify 5 different active oscillation regimes which correspond to 5 active oscillation solutions. The first, net distinction regards the Vacuum

and MSW regimes seen in Sec. 1.5.1 and 1.5.2; another discriminating rule is the order of the value of $\tan^2 \theta_{12}$ and Δm_{21}^2 . Schematically, starting from the higher Δm_{21}^2 and $\tan^2 \theta_{12}$ values, the oscillation scenarios are classified and named as:

- The MSW oscillation regimes:
 - Large Mixing Angle solution,
 - Small Mixing Angle region,
 - Low mass region;
- The Quasi-Vacuum regime;
- The Vacuum regime.

According to Ref. [40], we can roughly locate the Large Mixing Angle (hereafter *LMA*) solution in the Δm_{21}^2 sector $[10^{-3}, 10^{-5}] \text{ eV}^2$, and the $\tan^2 \theta_{12}$ sector $[10^{-1}, 1]$. Similarly, the Small Mixing Angle (*SMA*) solution can be located in the Δm_{21}^2 sector $[10^{-4.5}, 10^{-5.5}] \text{ eV}^2$, and the $\tan^2 \theta_{12}$ sector $[10^{-3}, 10^{-2}]$ while the Low mass solution (*LOW*) in the Δm_{21}^2 : $[10^{-6}, 10^{-8}] \text{ eV}^2$ and $\tan^2 \theta_{12}$: $[10^{-1}, 1]$ sectors.

Assuming the $\tan^2 \theta_{12}$ sector lying in the $[10^{-1}, 1]$ region, the Quasi-Vacuum regime (*QV*) is defined (Ref. [41]) to be in the Δm_{21}^2 sector $[10^{-10}, 10^{-7}] \text{ eV}^2$ while the pure Vacuum regime (*VAC*) in the $[10^{-12}, 10^{-10}] \text{ eV}^2$ region. The particular vacuum solution for which the ratio $\left[\frac{\Delta m_{21}^2}{4E} L \right] = 1$ is named *Just-So*. The Quasi-Vacuum regime interpolates smoothly between the Just-So and the MSW oscillation regimes: in this regime, the neutrino flavor transitions are increasingly affected by matter effects as Δm_{21}^2 increases and, as a consequence, the usual vacuum approximation has to be improved through matter-induced corrections.

1.8 The global analysis of neutrino data

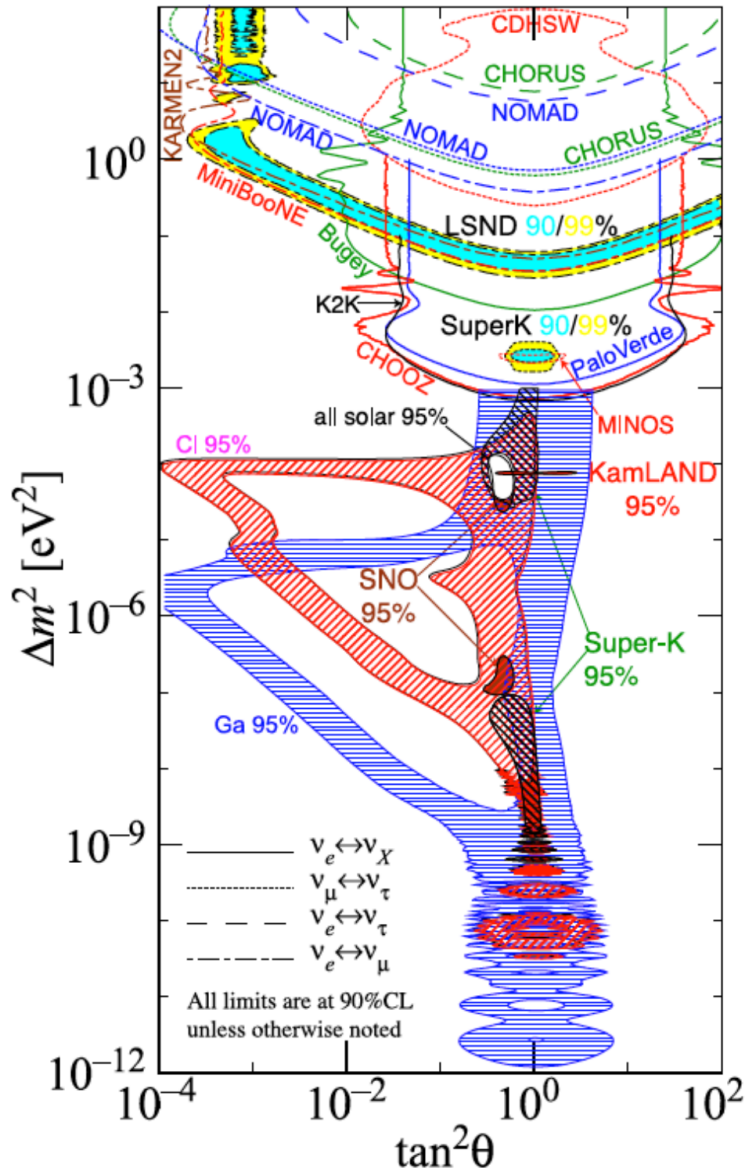


Figure 1.8: The regions of squared-mass splitting and mixing angle favored or excluded by various experiments (Ref. [7])

Chapter 2

The Borexino experiment

The Borexino experiment is a real-time detector whose main goal is the measurement of low energy solar neutrinos fluxes. Originally proposed by R.S. Raghavan in 1989, the BOREX experiment was to be a detector filled with several kiloton of a trimethylborate ($C_3H_9BO_3$) scintillator capable of detecting the 8B solar neutrinos. Neutral current interactions would lead to nuclear de-excitations of the ^{11}B in the scintillator, while the charged current neutrino capture reactions would lead to production of the positron-emitting ^{11}C . The Borexino experiment was to be the 4 ton prototype for the BOREX experiment.

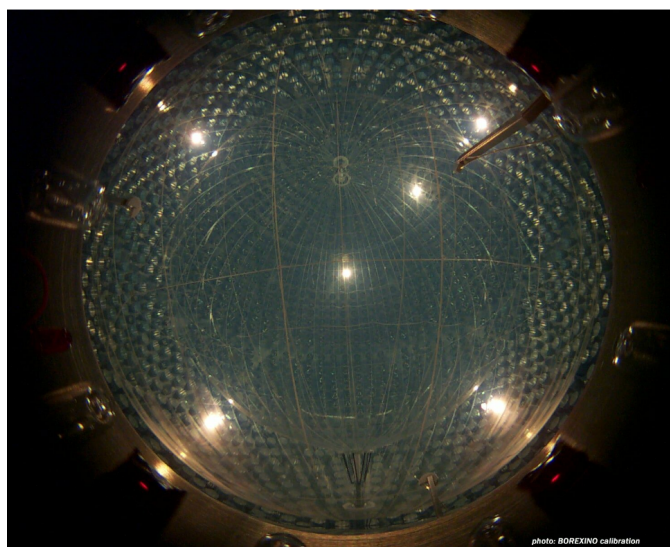


Figure 2.1: Inside view of the Borexino detector.

2.1 The LNGS underground laboratory

However, it was quickly realized that, if a scintillator could be purified sufficiently, an experiment such as Borexino could be an effective detector for the much higher rate of ${}^7\text{Be}$ neutrinos: the proposal evolved but the name remained. A one ton fiducial mass prototype, the Counting Test Facility (CTF) was built in the mid 1990s with the task of demonstrating the feasibility of large scale purification of organic liquid scintillators to the levels required for ${}^7\text{Be}$ neutrino detection. After successful demonstration of the purification techniques, the construction of the Borexino detector began in 1998. In late 2006, the filling process took place, first with ultra-pure water and then with the scintillator. Finally, after nine months of tests, data taking with a full detector (Fig. 2.1) started on May 15, 2007.

2.1 The LNGS underground laboratory

The Laboratori Nazionali del Gran Sasso (LNGS) are located in Assergi, a small town in the central Apennine Mountains, at approximately 100 miles north-east of Rome, Italy. The underground portion of the laboratory is adjacent to the A24 highway tunnel linking Rome with the Adriatic shoreline; in this peculiar site, the altitude is 963 m and the average rock cover is about 1,400 m with a shielding capacity against cosmic rays of 3,800 meter water equivalent (m.w.e.).

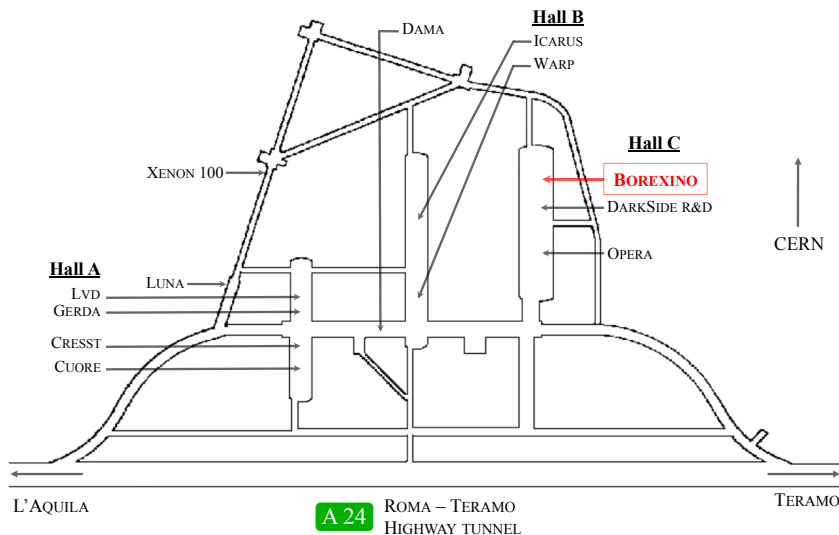


Figure 2.2: Layout of the underground experimental halls at LNGS.

The underground laboratory consists of three experimental halls named A, B and C, with lengths of about 100 m and heights above 18 m, for an overall volume exceeding 180,000 m³. Experimental setups of many differently sized projects are situated in the halls or in the network of service tunnels that complete the structure (see Fig. 2.2). The Borexino experiment occupies the North half the Hall C beside the Opera experiment.

Existing and future experiments for detection of low-energy neutrinos or rare events need a low-background environment and thus a deep underground location in order to reduce the cosmic radiation background by several order of magnitude (Fig. 2.3). At the underground LNGS, the muon flux is reduced of a factor 10⁶ respect to the surface.

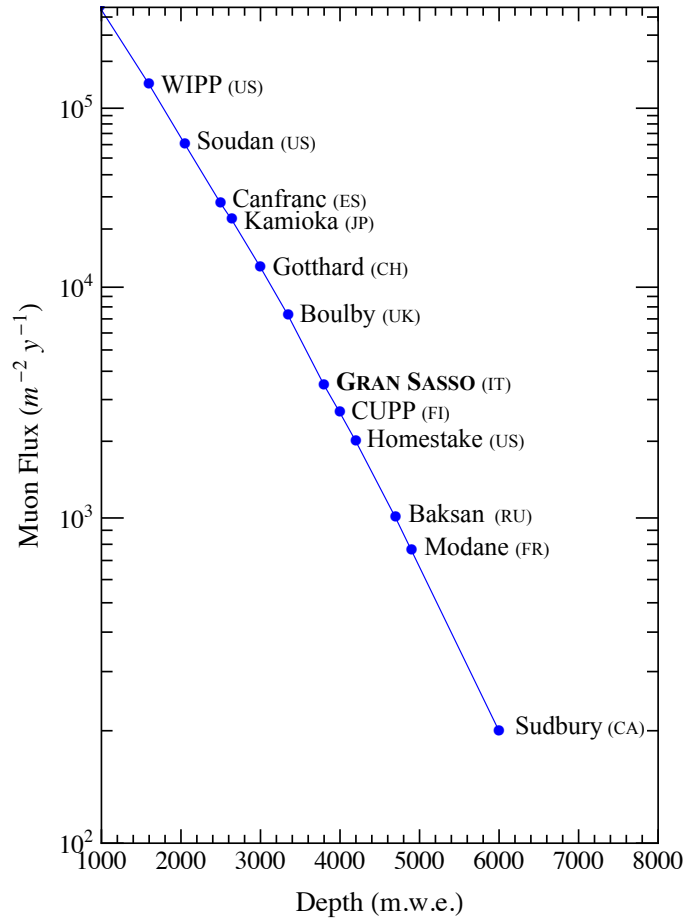


Figure 2.3: Prospect of the expected muons flux vs. depth overburden (m.w.e.) in different underground laboratories around the world.

2.2 The detector design

2.2 The detector design

In the current configuration, the Borexino detector contains 100 ton of liquid scintillator that converts the energy deposited by neutrino interactions into light. The detector is instrumented with photomultiplier tubes that can measure the intensity and the arrival time of this light, allowing the reconstruction of the energy, position and time of the events.

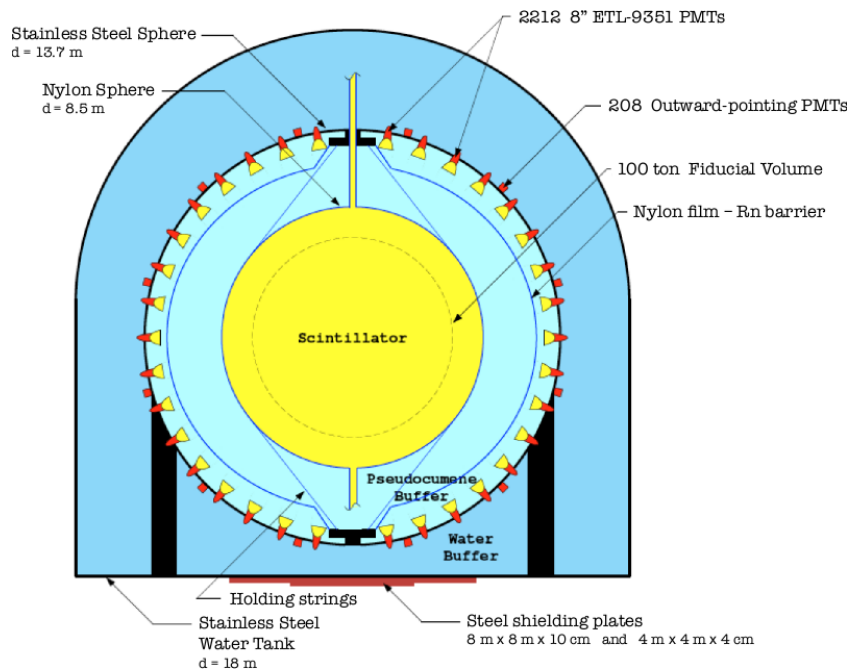


Figure 2.4: Schematic view of the Borexino detector.

In order to suppress the external background due to the surrounding rock, the detector is made of concentric spherical layers. Figure 2.4 shows this onion-like structure in a cut-away view. Requirements of radiopurity for construction materials obviously become more stringent the closer the materials are to the detector's active volume. The detector main characteristics are listed below, from inside to outside.

Liquid scintillator

After careful researches on different organic scintillators, both as small-scale lab tests and at larger scale in the Counting Test Facility (CTF) detector, the liquid scintillator was chosen as follows: a mixture of pseudocumene (PC, 1,2,4-trimethylbenzene, $C_6H_3(CH_3)_3$) as solvent and PPO (2,5-diphenyloxazole, $C_{15}H_{11}NO$) as fluor, with a 1.5 g/l concentration. This scintillator has an electron density of:

$$(3.307 \pm 0.003) \times 10^{29}/\text{ton}, \quad (2.1)$$

a mass density of about 0.879 g/cm^3 , and a specific scintillation output of ≈ 12000 photons/MeV (Ref. [42]). The sensitive volume of the scintillator is 320 m^3 (280 ton). Nevertheless, in order to maximize the radiopurity, a software volume cut can be applied to define a fiducial volume (FV).

Inner vessel

The scintillator is held in a transparent spherical nylon membrane of 8.5 m diameter and $125 \mu\text{m}$ thickness. This membrane, named inner vessel (IV), must be tight as it separates fluids which should never mix. Steel and nylon pipes are connected to the upper and lower poles, and allow loading and circulation from several fluid-handling facilities. The IV anchorage is guaranteed by a set of longitudinal nylon strings, with attached load cells for monitoring the IV mechanical stability.

Liquid buffer

The IV is surrounded by 1040 ton shielding liquid, the buffer. The buffer density has to be similar to the scintillator in order to balance the hydrostatic pressure and to avoid modifications of the vessel spherical shape or, even worse, mechanical ruptures. Since the pseudocumene density is about 0.88 g/cm^3 , water could not be used and it was decided to fill the buffer with pure pseudocumene plus dimethylphthalate (DMP, a quencher), in a 5 g/l solution. The addition of the quencher does not influence photon mean path nor Čerenkov light emission, while reduces the residual fluorescence of pseudocumene.

Outer vessel

After CTF experience, a second nylon membrane, named outer vessel (OV), was added in the buffer liquid region: its aim is to stop radon gas diffusion toward the inner vessel. It has a diameter of 12.6 m and a $125 \mu\text{m}$ thickness.

2.2 The detector design

Stainless steel sphere

All the components described so far are housed in a stainless steel sphere (SSS) 8-10 mm thick, with a 13.7 m diameter. This sphere also supports the photomultipliers and it is held by 20 legs welded to the external water tank floor.

External tank

The full experimental setup is housed in a dome shaped steel tank. The diameter of the cylinder base is 18 m while the highest point of the dome is 17 m above the floor. The tank is filled with 2400 ton of ultra pure water as the outermost shielding of the detector. Water tank inner walls, as well as the outer SSS surface, are covered with some Tyvek sheets. Tyvek is a high reflectivity material that enhances the muon detection probability by maximizing light collection.

Photomultiplier tubes

In Borexino there are 2212 8" ETL-9351 photomultipliers (PMTs), made of a special low radioactivity glass, with a complex sealing system studied to resist pseudocumene corrosive action on the front and water action on the back. This kind of PMTs is sensitive to light with wavelength between 350 nm and 500 nm and its quantum efficiency peak at 420 nm is around 26%. 1838 PMTs are equipped with aluminum light concentrators (Fig. 2.5 left) in order to increase light collection capability. The overall geometrical coverage is $\approx 30\%$.

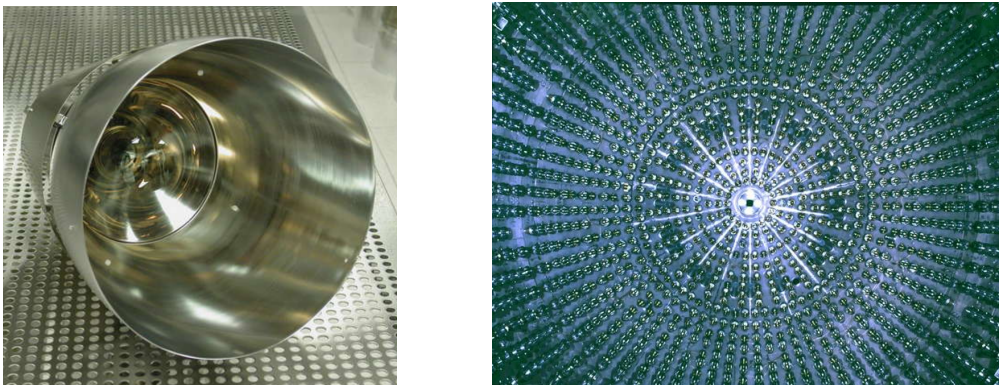


Figure 2.5: On the left, a sealed Borexino PMT fully assembled, with light concentrator. On the right, an inside view of the Borexino stainless steel sphere.

The photomultipliers are installed on the stainless steel sphere (Fig. 2.5 right) in dedicated feed-throughs and are connected to the outside via single submarine cables which carry both signal and high voltage. Exiting from the SSS, the 55 m length cables leave the water tank in the upper dome and finally reach the electronic room situated in the nearby Big Building East (see Fig. 2.6).

Muon Veto

Borexino is provided with both an inner and an outer muon veto. The Inner Muon Veto consists of about 400 PMTs without light concentrators. The high acceptance angle allows them to collect a strong signal in response to Čerenkov tracks produced by muons crossing the buffer liquid. The Outer Muon Veto is instead composed of 208 additional PMTs installed in the water tank, in order to detect the Čerenkov light produced by muons in the shielding water. A detailed description of the outer muon detector can be found in Ref. [43] and [44].

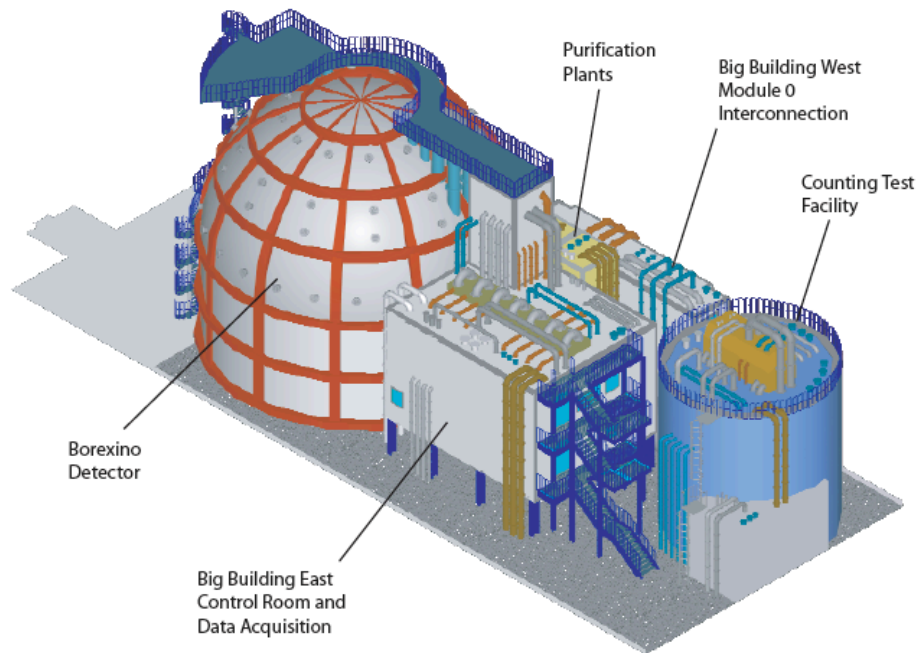


Figure 2.6: The layout of the Borexino experiment in Hall C of the LNGS. The Borexino detector is the large dome shown on the left. The CTF housed in the blue cylindrical structure is shown on the right.

2.3 Signal processing and Data Acquisition System

Purification skids

Borexino has been purifying scintillator with industrial scale purification skids. These skids remove contaminants with four processes: filtration, vacuum distillation, water extraction, and nitrogen stripping. Several 50 nm filters reduce particulates suspended in the scintillator. Vacuum distillation separates impurities with a higher boiling point than the scintillator. Water extraction is effective in removing polar molecules and metal ions, and it also hydrates the scintillator. Nitrogen stripping removes gases such as oxygen (which would quench the light output of the scintillator) and radioactive noble gases like radon, argon, and krypton. For the extraction processes where the scintillator is in contact with water or nitrogen, great care must be taken in order to prevent a contamination of the scintillator. A more detailed discussion is presented in Ref. [45].

2.3 Signal processing and Data Acquisition System

The basic observables for the identification of neutrino events in Borexino are the total energy released in the scintillator, as measured by the number of photons emitted, and the time distribution of these photons. The electronic signal processing scheme shown in Fig. 2.7 is designed to achieve the timing properties needed for a variety of key tasks: reconstruction of the event position, pulse shape analysis (PSA) of α and β types of events, and the identification of a variety of delayed coincidence tags with a wide range of time bases.

The data acquisition (DAQ) is based on the Linux operating system. The DAQ software is entirely custom made, with extensive use of multi-tasking techniques. User interfaces are all based on WEB techniques. The signal from PMTs is AC coupled to a front-end card (Ref. [46]) that performs noise filtering, pre-amplification, shaping and integration of the input signal. It provides both a linear response used for time measurement and a voltage signal proportional to the total charge. Each front-end board provides also an analog sum of 12 linear output signals that extend the dynamic range of the system to ~ 30 MeV by means of a flash ADC system. The outputs of the front end cards are sent to a specially designed VME slave card that performs the analog to digital conversion of the charge signal, measures the time of the linear signal with 0.4 ns resolution, computes the sum of recorded hits in a 60 ns time window (used for triggering) and stores the whole information in a dual port random access memory.

The outer muon tubes are read with a different front-end system that performs a charge to time conversion of each signal after a linear pre-amplification. The converted signal is then sent to time-digitizers which are read by their own processor. The trigger

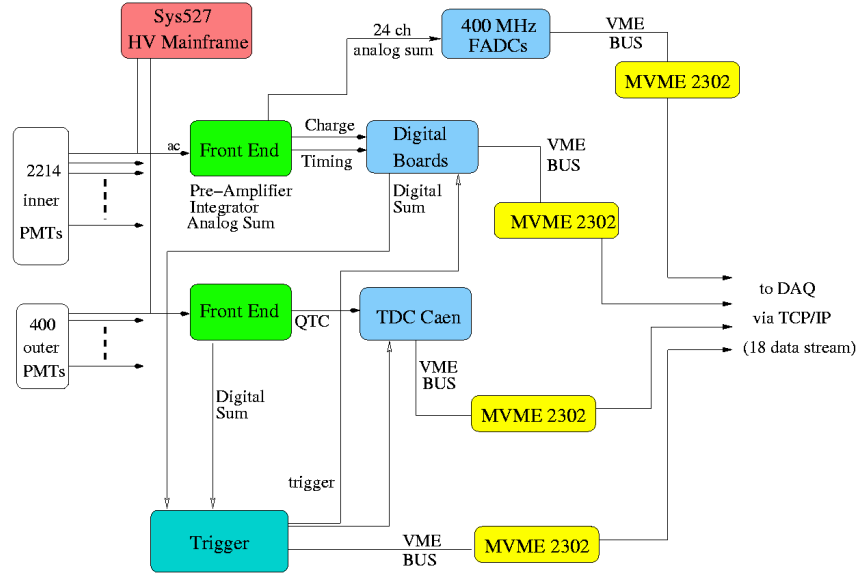


Figure 2.7: Block diagram of the Borexino electronics layout

can be generated both by the internal as well as by the outer muon detector. We require at least 25 PMTs hits occurring in a time window of 60 ns in the inner detector to generate a trigger. The trigger threshold is mainly determined by the ^{14}C contamination (see Sec. 2.7.2), which gives the largest contribution to the single rate.

2.4 Calibration and monitoring

Borexino relies on the precise determination of the time of flight of the photons from the location of the scintillation event to the PMTs system in order to reconstruct the event position and to define the fiducial volume. Furthermore, the knowledge of the total charge collected by each photomultiplier is important for the determination of high energy events. For these reasons, both time and charge calibration of the photomultiplier system is of utmost importance. To this aim, a multiplexed system of optical fibers has been developed.

Precision in the time measurement of single hits affects directly the position reconstruction precision. Position resolution is limited by the scintillator fluorescence decay time of 3.5 ns (effectively increased to 5.5 ns after light propagation effects, Ref. [47]), by the photomultiplier transit-time jitter of ~ 1 ns and by the inter-photomultiplier time equalization, which should be maintained at the sub-nanosecond level and is regularly

2.4 Calibration and monitoring

checked. The precision of the time measurement is also necessary for α - β discrimination, based on the different fluorescence time profiles for α and β scintillation events.

An accurate energy determination and resolution are crucial for the spectral shape recognition of the neutrino signal: the energy resolution of the detector depends on good charge calibration, the energy being determined, through a proportionality relation, from the number of detected photons or from the total charge collected by all photomultipliers.

The calibration program studies the detector response by means of laser monitoring and external point sources inserted periodically into the tank, as well as using active tags of trace impurities in the liquid scintillator. Here below a short list of the methods used in Borexino.

Laser monitor. The pulse timing and the gain of each individual phototube of the inner detector are calibrated by a laser system. Photons from this source are distributed to all PMTs via thin quartz fibers connected to the optical concentrators. The light yield corresponds to single photoelectrons as in real neutrino events. The outer muon veto detector is calibrated by a set of blue light-emitting diodes that are mounted on the inside wall of the outer tank. Their gains match typical photon yields of Čerenkov events.

Radioactive sources. The energy response can be continuously monitored using the internal trace of radioactivities originated from liquid scintillator as well as selected inserted sources. The spectroscopic features of the sources cover the entire range of energies up to about 5 MeV that is of interest to most of the physics questions addressed by Borexino. Since light quenching introduces non-linearities in the energy scale, it is crucial to have calibrating points throughout the entire energy region of interest. We designed a series of point calibration sources which can be positioned throughout the detector volume. The Borexino calibration campaigns were performed between October 2008 and July 2009: several α , β , γ and neutrons sources (see table 2.1 and 2.2) were deployed in about 300 positions inside the detector active region.

Calibration of the neutrino response. In order to provide a direct demonstration of the overall neutrino response of the detector, a calibration by means of a man-made sub-MeV ν -source with activities in the Megacurie range is foreseen. Plans include both electron-neutrino (^{51}Cr) and electron anti-neutrino (^{90}Sr) sources. A tunnel has been installed just below the external steel tank for inserting and retrieving the heavily shielded source containers on steel tracks.

	γ							
Source	^{57}Co	^{139}Ce	^{203}Hg	^{85}Sr	^{54}Mn	^{65}Zn	^{60}Co	^{40}K
Energy (MeV)	0.122	0.165	0.279	0.514	0.834	1.1	1.1, 1.3	1.4

Table 2.1: Calibrations sources: the gamma emitting isotopes.

	β		α	n		
Source	^{14}C	^{214}Bi	^{214}Po	n-p	n+ ^{12}C	n+Fe
Energy (MeV)	0.15	3.2	7.6	2.226	4.94	~ 7.5

Table 2.2: Calibrations sources: the alpha, beta and neutron emitting isotopes.

2.5 Neutrino detection in Borexino

In the Borexino detector, neutrinos are detected by means of electron scattering which can proceed via the charged and neutral current processes:

$$\nu_x + e^- \rightarrow \nu_x + e^- .$$

The charged current interaction, mediated by the charged W^\pm vector bosons, is possible only for electron flavor neutrinos. Instead, the neutral current interaction, mediated by the Z^0 boson, is sensitive to all three flavors of neutrinos, although with a smaller cross section (see Fig. 2.8).

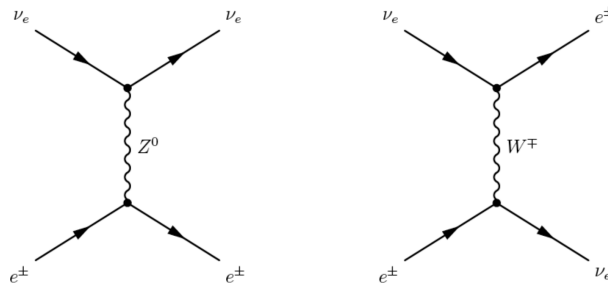


Figure 2.8: Tree-level of Feynman diagrams for ν - e^\pm scattering. All neutrino flavors scatter via the neutral current reaction (left) while only the electron neutrino can interact through a charged current interaction (right).

2.6 ${}^7\text{Be}$ solar neutrino

Due to combination of the two amplitudes, at 1 MeV the cross section of electron neutrinos is about five times larger than that of muon or tau neutrinos. If the electron neutrinos produced by the sun change into muon or tau neutrinos, they will be partly missed by the detector and this will result in a lower rate measurement.

2.5.1 Neutrino scattering cross-section

The overall shape of the neutrino-induced recoil-electron energy spectrum recorded by an ideal detector is given by the differential cross section which, in the frame of the electroweak theory (Ref. [48]), is given by:

$$\frac{d\sigma}{dE} = \sigma_e \left\{ g_l^2 + g_r^2 \left(1 - \frac{E}{E_\nu} \right) - g_l g_r \frac{m_e c^2 E}{E_\nu^2} \right\} \quad \sigma_e = \frac{2G_F^2 m_e}{\pi \hbar^4 c^2} \quad (2.2)$$

$$g_r = \sin^2 \theta_W \sim 0.23 \quad g_l = \begin{cases} \nu_e : & \sin^2 \theta_W + \frac{1}{2} \sim 0.73 \\ \nu_{\mu, \tau} : & \sin^2 \theta_W - \frac{1}{2} \sim -0.27 \end{cases}$$

In Eq. 2.2, the leading constant σ_e is equal to $8.803 \times 10^{-46} \text{ cm}^2$ and the Weinberg mixing angle θ_W is related to the ratio of the masses of the W and Z bosons:

$$\theta_W = \arccos(M_W/M_Z) \sim 28^\circ.$$

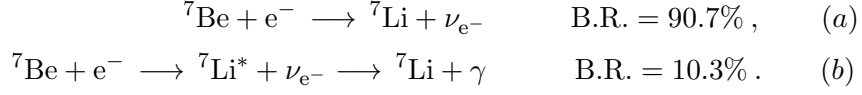
Note that the value of g_l for electron flavor neutrinos leads to an overall larger cross section relative to the other flavor neutrinos; this is due to the fact electron neutrinos may interact via the charged and neutral current interactions, whereas the other flavors can only interact through the neutral current interaction. The total cross section is then given by the integral of the differential cross section from 0 up to E_{\max} :

$$\sigma = \frac{2G_F^2 m_e E_{\max}}{\pi \hbar^4 c^2} \left\{ (g_l^2 + g_r^2) - \left(\frac{g_r^2}{E_\nu} + g_l g_r \frac{m_e c^2}{2E_\nu^2} \right) E_{\max} + g_r^2 \frac{E_{\max}^2}{3E_\nu^2} \right\}. \quad (2.3)$$

2.6 ${}^7\text{Be}$ solar neutrino

The primary goal of Borexino is to extract information about neutrino oscillation parameters and to probe the fusion process in the sun. Borexino is measuring the ${}^7\text{Be}$ neutrinos which are the second most intense flux after that of the primary pp fusion reaction.

${}^7\text{Be}$ neutrinos are produced in a two body electron-capture reaction:



The reactions (a) and (b) result in a monoenergetic 862 keV and 384 keV solar neutrino line, respectively. The reaction (b) is followed by a 477.6 keV gamma emission that is absorbed in the sun and cannot be seen by the detector.

In a neutrino-electron scattering experiment such as Borexino, the neutrino interacts with an electron in a scintillator molecule (typical binding energy of a few eV: without loss of generality, we can assume it to be free) which then produces scintillation light from excitation and ionization of other scintillator molecules. This situation is analogous to Compton scattering and the recoil-electron spectrum is nearly flat with a sharp edge occurring at:

$$E_{\text{max}} = \frac{2E_{\nu}^2}{2E_{\nu} + m_e c^2} \implies E_{\text{max}}(E_{\nu} = 862 \text{ keV}) \sim 667 \text{ keV} .$$

This sharp cut-off (Fig. 2.9) is a distinctive feature of a monoenergetic neutrino source.

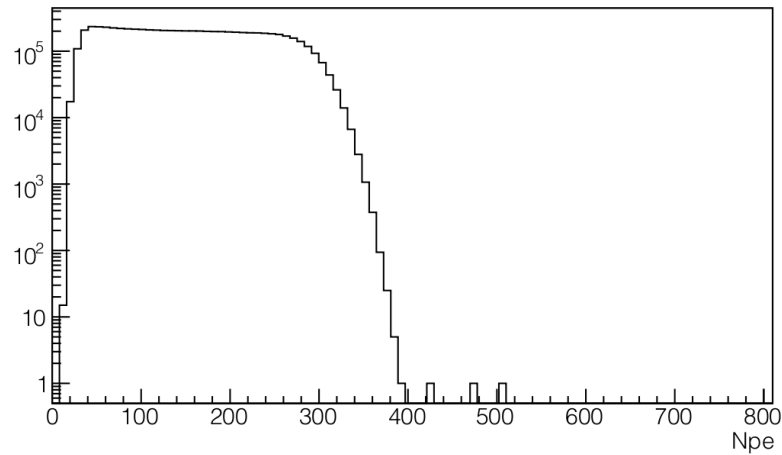


Figure 2.9: Typical ${}^7\text{Be}$ recoil-electron spectrum. The neutrino monoenergetic nature results in a sharp cut-off of the spectrum. N_{pe} is one of the Borexino energy variables.

2.6 ${}^7\text{Be}$ solar neutrino

2.6.1 Seasonal variations

In Čerenkov based detectors it is relatively easy to verify the solar origin of the neutrinos simply by projecting back the light cone from the recoil-electron: the axis of this cone, on average, points towards the neutrino source. In scintillation detectors, the light emission is isotropical and therefore the directional information is lost. However, the solar origin of neutrinos could be probed thanks to the fact that the distance from the earth to the sun varies over the year.

The earth's elliptical orbit around the sun has an eccentricity ϵ of 0.0167 and a semi-major axis, a , of 1.496×10^8 km. For any elliptical orbit, the eccentricity is related to the radii at aphelion and perihelion by:

$$\epsilon = \frac{r_{\text{aph}} - r_{\text{per}}}{r_{\text{aph}} + r_{\text{per}}} = 1 - \frac{2}{1 + \frac{r_{\text{aph}}}{r_{\text{per}}}}.$$

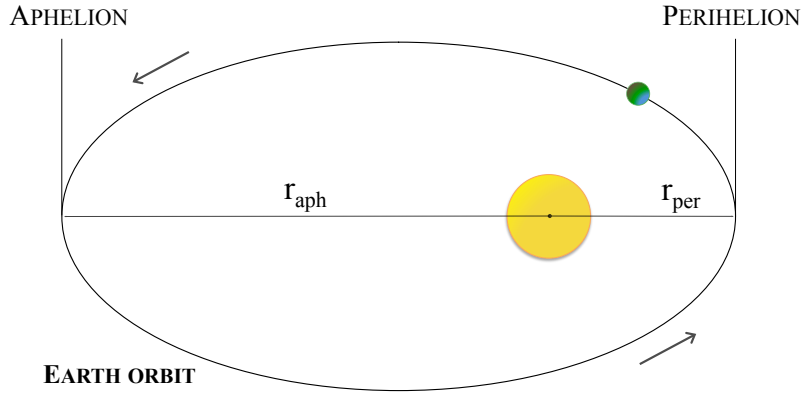


Figure 2.10: Pictorial representation of the earth-sun orbit with eccentricity exaggerated for clarity: the aphelion and perihelion orbital radii are indicated with respect to the center of the sun.

Over the course of one-year period T , the earth-sun distance varies as:

$$L(t) = L_{\text{avg}} \frac{(1 - \epsilon^2)}{1 + \epsilon \cos\left(\frac{2\pi t}{T}\right)} = L_{\text{avg}} \left[1 - \epsilon \cos\left(\frac{2\pi t}{T}\right) \right] + O(\epsilon^2). \quad (2.4)$$

The flux at the earth is inversely proportional to the squared earth-sun distance r , thus, the flux at perihelion and at aphelion will be in the ratio:

$$\Phi_{\text{per}} = \Phi_{\text{aph}} \frac{r_{\text{aph}}^2}{r_{\text{per}}^2} \Rightarrow \left(\frac{r_{\text{aph}}}{r_{\text{per}}} \right)^2 = \left(\frac{1 + \epsilon}{1 - \epsilon} \right)^2 \approx 1.07. \quad (2.5)$$

According to Eq. 2.5, Borexino should observe a 7% difference between the rate around January (perihelion) and the rate around July (aphelion). It is worth to notice that this 7% modulation is expected assuming no neutrino oscillation in Vacuum regime. If there were vacuum oscillation, the expected seasonal variation would generally be greater.

Since $\epsilon \ll 1$, we can ignore terms larger than first order. Assuming the average neutrino rate to be R_{avg} , and the average distance $L_{\text{avg}} = a$, then we can express the time dependent solar neutrino rate $R(t)$ as:

$$R(t) = R_{\text{avg}} \left(\frac{L(t)}{L_{\text{avg}}} \right)^2 = R_{\text{avg}} \left[1 + 2\epsilon \cos\left(\frac{2\pi t}{T}\right) \right]. \quad (2.6)$$

2.7 Radioactive backgrounds in Borexino

The scientific goal of Borexino is to measure rare event rates at low energy, where natural background radiation is large.

The collaboration made an enormous effort in identifying, measuring, and analyzing the sources of background and their contributions. In some cases the required levels of purity were so low that available measurement techniques did not have the needed sensitivity, and new measurement devices such as the Counting Test Facility were developed to meet these needs. The purities and properties of a large number of substances were measured to find suitable construction materials.

The background sources in Borexino can be subdivided in internal and external background. External backgrounds are those in which the radiation originates in the outside environment as well as in materials within the detector close to the fiducial volume. In this context they will include everything except the intrinsic scintillator contamination which actually is the internal background.

Borexino must deal with all types of backgrounds including α , β , γ , n, and μ . Some are easily absorbed like α particles, while others like muons easily penetrate the detector shielding, so they must be tagged and subtracted from the data.

2.7 Radioactive backgrounds in Borexino

The strategy against backgrounds is based on the idea of shielding the fiducial volume from radioactive external activity, by means of high purity materials which absorb the radiation before it reaches the interior. In the case of muons which are largely suppressed by the rock overburden (Fig. 2.3), the shielding itself is used to observe the residual muons as they pass through so the event can be identified (see Sec. 2.7.1).

In Tab. 2.3 results concerning the radioactivity of three different (one for each underground laboratory Hall) rock samples are reported.

The Borexino core activity is more than 13 orders of magnitude below the ambient environment. Table 2.4 shows the major sources of background present in Borexino, the approximate natural activity level encountered in Hall C of the underground labs, the contaminant level which is tolerable by Borexino, the method by which the contaminant is removed and the level actually obtained by Borexino. It can be seen how, in several categories, the Borexino purification system has performed remarkably and exceeded the requirement by an order of magnitude or more. A big challenge for the Borexino experiment was and still is today to deal with the large number of radioactive isotopes that decay with energies in or above the region of interest.

Sample	^{232}Th (Bq/kg)	^{238}U (Bq/kg)	^{40}K (Bq/kg)	^{214}Bi (Bq/kg)
Hall A rock	8.8 ± 0.3	84.7 ± 8.4	224 ± 6	41.9 ± 0.6
Hall B rock	0.25 ± 0.08	5.2 ± 1.3	5.1 ± 1.3	4.2 ± 0.3
Hall C rock	0.27 ± 0.10	8.2 ± 1.7	2.9 ± 1.4	5.1 ± 0.2

Table 2.3: Rock radioactivity at the LNGS underground laboratories (Ref. [49]).

In underground laboratories, the radioactivity levels can vary significantly from the earth's average activity. The earth's crust contains a number of radioactive elements whose relative concentrations vary with location and are dependent on the rock type. Also the atmosphere contains some radioactive elements such as radon, krypton and argon. In particular, the amount of radon can vary widely because it emanates from the ground and depends strongly on local conditions. This naturally occurring radioactivity requires the Borexino detector to be vacuum tight to prevent dirt or air contamination: Borexino can tolerate no more than 10 cm^3 of ambient air in the detector.

2.7.1 External backgrounds

Muons

Although the rock shielding greatly reduces their flux, high energy muons (originating from cosmic ray interactions in the atmosphere) are still able to penetrate into the depth of the Gran Sasso laboratory, where the Borexino experiment is located. The muon flux in Hall C is $1.2 \mu/\text{m}^2/\text{h}$ (Ref. [50, 51]) that is about 4500 muons entering the inner part of the detector in a day.

In Borexino very low intrinsic radiogenic contamination of all detector components needs to be accompanied by the efficient identification of muons and of muon-induced backgrounds. Muons, by spallation processes along their trajectory through the detector, produce unstable nuclei whose decays can mimic the expected signals (i.e. ^{11}C); for isotopes with half-lives longer than a few seconds, the dead time induced by a muon-related veto becomes unacceptably long, unless its application can be restricted to a sub-volume along the muon track. Consequently, not only a high-efficiency muons identification but also a precise track reconstruction is of primary importance for the physics program of the experiment.

A much more problematic contribution to the background comes from high-energy neutrons generated by muons in the interactions with the surrounding rock or with the detector material. The energy of these neutrons may even extend up to the GeV region (Ref. [52]).

In order to reduce such background, a fundamental role is played by an outer water-Čerenkov detector which surrounds the inner detector. The identification of muons is based on the complementarity between outer and inner detectors (see Sec. 2.2). Different methods of muon identification were studied and their veto efficiencies calculated: the overall muon veto efficiency is found to be 99.992% or better. The performances of ad hoc track reconstruction algorithms were tested against muon events of known direction such as those from the CNGS neutrino beam, and the final angular resolution results $\sim 3^\circ - 5^\circ$ while the lateral resolution is $\sim 35 - 50$ cm, depending on the impact parameter of the crossing muon. The strategies adopted to identify muons are reviewed and their efficiency is evaluated and described in Ref. [53].

Neutrons

The neutron flux from the rock walls at LNGS was measured to be $(1.08 \pm 0.02) \times 10^{-6} \text{ cm}^{-2} \text{ s}^{-1}$ for the thermal component and $(1.98 \pm 0.05) \times 10^{-6} \text{ cm}^{-2} \text{ s}^{-1}$ for the epithermal one [$E_n = 5 \times 10^2 - 10^3$ eV] (Ref. [54]). The thermal neutrons have an energy of about 0.025 eV and are primarily produced from fission and (α, n) reactions. The 2 m water

2.7 Radioactive backgrounds in Borexino

shield attenuates the neutron flux by a factor of 10^8 . Fast neutrons ($E_n > 0.5$ eV) have to be moderated before being captured because the relative cross section strongly decreases with energy increasing. Neutrons are best moderated by low A materials, preferably containing a high density of hydrogen. The 2 m water shielding is therefore adequate to effectively reduced the neutron background.

Radon

The underground Gran Sasso labs have a radon activity of 100 Bq/m³ in air and 104 Bq/m³ in water. The radon air activity would reach 2000 Bq/m³ were it not for a continuous venting of the halls with fresh outside air piped in through the highway tunnel. This air supply is essential to maintain safe working conditions. Radon contamination is one of the reasons for which the detector must remain leak tight to air and it is especially dangerous for Borexino because it is more soluble in pseudocumene than in air.

2.7.2 Internal backgrounds

All background sources that are intrinsically linked to the liquid scintillator and generate energy depositions inside the inner vessel are generally ascribed to internal backgrounds.

¹⁴C

On earth surface, ¹⁴C is cosmogenically produced via the reaction $^{14}\text{N}(n, p)^{14}\text{C}$, leading to a relative abundance on ¹⁴C of $\sim 1.2 \times 10^{-12}$ g/g in living organic matter. The β^- decay of ¹⁴C is characterized by $Q = 156$ keV and $\tau_{1/2} = 5730$ y. In old oil reservoirs this contribution has decayed away. The concentration is therefore determined by a few site-dependent underground production mechanisms, initiated by the natural radioactivity of the rocks. In the scintillator procurement for the experiment, the choice of oil batches with lowest ¹⁴C level was a major requirement, as ¹⁴C, chemically identical to ¹²C, cannot be removed by any purification process.

In the neutrino energy window, the acceptable relative abundance is 3×10^{-18} g/g. This very low tolerance is due to the fact that Pseudocumene is a carbon-based scintillator, and a large amount of ¹⁴C would generate signal pile-up. Today, Borexino has reached the needed radiopurity and can feature a 10^{-18} g/g ¹⁴C contamination.

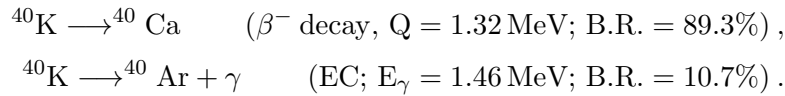
²³⁸U, ²³²Th

Intrinsic scintillator radioactivity is mostly due to radio-isotopes belonging to the natural ²³⁸U and ²³²Th chains. Assuming secular equilibrium, Borexino could not tolerate

concentrations of these elements greater than 10^{-16} g/g. Anyway, thanks to its particular design and to sophisticated purification procedures, Borexino has not only reached but also improved the expected radipurity limits, at the level of there is a 10^{-17} g/g contamination for ^{238}U and of 10^{-18} g/g for ^{232}Th .

^{40}K

Another intrinsic background component in organic material is ^{40}K , which decays with a half life of 1.3×10^9 y via two different channels:



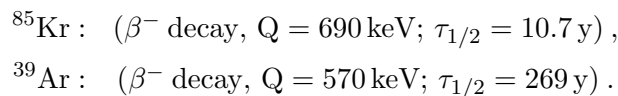
^{40}K has an isotopic abundance of 1.2×10^{-4} g/g with respect to whole natural potassium (K_{nat}) which is present in the earth crust with a 2.4% concentration. Borexino background requirements implied that the scintillator should not exceed a K_{nat} concentration of about 10^{-14} g/g. Today, data show that in Borexino the achieved ^{40}K contamination fulfills this request.

^{222}Rn and its daughters

Radon is a chemically inert gas that shows a high diffusion capability in air and in materials. Underground sites are rich in radon as the isotope is formed within the ^{238}U radioactive chain in secular equilibrium and diffuses away easily. Radon decays with a half life of 3.8 d, but determines the build up of ^{210}Pb , a long-lived nuclide that can be absorbed by metal and plastic surfaces. The two successive fast decays of ^{210}Pb are particularly dangerous: ^{210}Bi (β^- , $Q = 1.2$ MeV) and ^{210}Po (α , $Q = 5.3$ MeV, quenched to ~ 350 keV).

^{85}Kr and ^{39}Ar

The air of the experimental Hall also contains traces of ^{85}Kr (an anthropogenic fission product) and ^{39}Ar (cosmogenic), with activities of ~ 1.1 Bq/m³ and ~ 13 mBq/m³ respectively. The decay processes are the following:



Avoiding air exposure of fluids is also important in order to limit these contaminations.

2.7 Radioactive backgrounds in Borexino

Contaminant	Source	Normal concentrations	Borexino requirements	Reduction method	Borexino achieved
Muons	Cosmic	$200 / (\text{s}\cdot\text{m}^2)$	$10^{-10} / (\text{s}\cdot\text{m}^2)$	Location, OD veto, pulse shape	$< 10^{-10} / (\text{s}\cdot\text{m}^2)$
^{14}C	PC-PPO	10^{-12} g/g	10^{-18} g/g	Old oil, CTF tests, threshold cut	10^{-18} g/g
^{238}U ^{232}Th	Dust	10^{-4} g/g	$< 10^{-16} \text{ g/g}$	Purification	$\sim 10^{-17} \text{ g/g}$ $\sim 10^{-18} \text{ g/g}$
^{210}Po	PPO, Rn	Secular equilibrium with ^{238}U	Secular equilibrium with ^{238}U	Purification, α - β discrimination	0.01 cpd/ton
^{222}Rn	Air	10-100 Bq/l	$< 1 \text{ cpd}/100 \text{ ton}$	N_2 stripping, delayed coincidence	$< 0.02 \text{ cpd}/\text{ton}$
^{85}Kr	N_2	$1 \text{ Bq}/\text{m}^3$	$< 0.01 \text{ ppt}$	N_2 Stripping	$< 0.01 \text{ ppt}$
^{208}Tl	^{232}Th	Secular equilibrium with ^{232}Th	Secular equilibrium with ^{232}Th	Purification, statistical subtraction	$< 28 \text{ cpy}/100 \text{ ton}$

Table 2.4: Sources of background, typical level of the background, maximum tolerable signal level for Borexino, methods by which they are reduced, and what was ultimately achieved in Borexino.

In particular, ^{85}Kr is extremely annoying since its energy spectrum lies exactly in the same energy region of the ^7Be one.

Krypton and argon are usually present in the common liquid nitrogen. Since nitrogen stripping proved to be a successful strategy in purifying the scintillator from these radioactive gases, the collaboration has investigated the product offered by different companies in terms of trace contaminants, and a Low Krypton and Argon Nitrogen (LAKN) has been used in all the purification phases.

At present, Borexino has reached its radiopurity goal of ^{85}Kr and ^{39}Ar contamination < 0.01 ppt.

Surface background

We define as surface background any contamination, intrinsic or acquired, of the nylon of the inner vessel membrane, the only material directly in contact with the scintillator. In ideal conditions there should be no significant contributions of this kind, as the nylon extrusion, the inner vessel assembly and its transportation were performed under the most stringent purity requirements. The main worry is that exposure to radon could lead to a deposition of its daughters and especially of ^{210}Pb .

2.8 Physics goals and achieved results

Since the start of data taking, the Borexino collaboration has released many interesting results. In particular, three recent publications demonstrate the unique characteristics of Borexino: the ^7Be solar neutrino rate measurement with an accuracy better than 5%, the evidence of a null day-night asymmetry with accuracy of $\sim 1.5 \times 10^{-2}$ and, for the first time, the direct measurement of the pep solar neutrino flux. It is also worth mentioning the observation of geo-neutrinos signal and the measurement of ^8B neutrino flux above 3 MeV.

2.8.1 ^7Be solar neutrino flux measurement

In 2008, we reported a direct measurement of the ^7Be solar neutrino flux with combined statistical and systematic errors of 10% (Ref. [55]). Following a campaign of detector calibrations and thanks to a fourfold increase in solar neutrino exposure, we recently presented a new ^7Be neutrino flux measurement with a total uncertainty less than 5%. For the first time, the experimental uncertainty is smaller than the theoretical uncertainty coming from the Standard Solar Model prediction of the ^7Be neutrino flux (Ref. [18]).

2.8 Physics goals and achieved results

The new result is based on the analysis of 740.7 live days (after software cuts) in the period from May 16, 2007 to May 8, 2010, corresponding to a 153.6 ton·y fiducial exposure. During the first 1.6 years of Borexino operation, the energy and position reconstruction algorithms were tuned, and their performances estimated, using intrinsic activities such as ^{14}C , ^{210}Po , and ^{11}C . The first deployed source calibrations were carried out in 4 campaigns between October 2008 and July 2009. Encapsulated radioactive sources, including ^{57}Co , ^{139}Ce , ^{203}Hg , ^{85}Sr , ^{54}Mn , ^{65}Zn , ^{40}K , ^{60}Co , and ^{222}Rn , were placed inside the scintillator volume using a rod-based source deployment system. Using seven CCD (Charge Coupled Device) cameras mounted within the PMTs array, the positions of the sources could be determined with a precision better than 2 cm. Thanks to these calibration campaigns there has been a significant decrease in the uncertainties associated with the detector energy response and the fiducial volume, by factors of 4.6 and 2.2, respectively, relative to Ref. [55]. Our best value for the interaction rate of 862 keV ^7Be solar neutrinos in Borexino today is:

$$46.0 \pm 1.5(\text{stat}) \pm_{-1.6}^{+1.5}(\text{syst}) \text{ cpd}/100 \text{ ton} , \quad (2.7)$$

where we remind that 1 ton of pseudocumene contains $(3.307 \pm 0.003) \times 10^{29}$ target electrons. If the neutrinos are assumed to be purely ν_e , this corresponds to an 862 keV ^7Be solar neutrino flux of $(2.78 \pm 0.13) \times 10^9 \text{ cm}^{-2}\text{s}^{-1}$. The corresponding flux prediction from the SSM is $(4.48 \pm 0.31) \times 10^9 \text{ cm}^{-2}\text{s}^{-1}$, which, if all the neutrinos remained ν_e , would yield an interaction rate of 74.0 ± 5.2 counts/(day·100 ton) in Borexino: the observed interaction rate is 5.0σ lower. The ratio of the measured to the predicted ν_e -equivalent flux is 0.62 ± 0.05 . Under the assumption that the reduction in the apparent flux is the result of ν_e oscillation to ν_μ or ν_τ (which also undergo electron elastic scattering interactions, but with a cross section about 4.5 times lower than ν_e at this energy), we find P_{ee} : 0.51 ± 0.07 at 862 keV. The improved constraint on the low energy solar P_{ee} is shown in Fig. 2.12. and a detailed discussion about this result can be found in Ref. [1].

2.8.2 The day-night asymmetry measurement

Matter-enhanced neutrino oscillations in the earth may induce regeneration of the ν_e flavor eigenstate of solar neutrinos during the night in some regions of the oscillation parameter space. Thus, real-time solar neutrino experiments like Borexino, may either detect or exclude different solar neutrino interaction rates during the day and night. Solar neutrino day-night asymmetry measurements are sensitive to both ν_e appearance and disappearance.

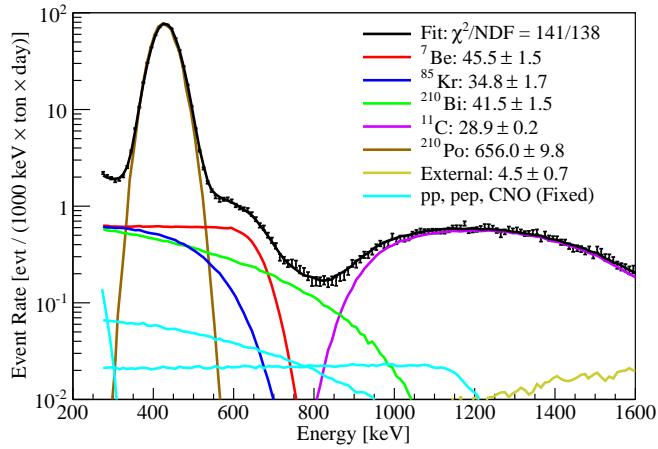


Figure 2.11: A Monte Carlo based fit over the energy region 270-1600 keV to a spectrum from which some, but not all, of the α events have been removed using a pulse shape analysis cut, and in which the event energies were estimated using the number of photon detected by the PMT array. The fitted event rates refer to the total rate of each species, independently of the fit energy window.

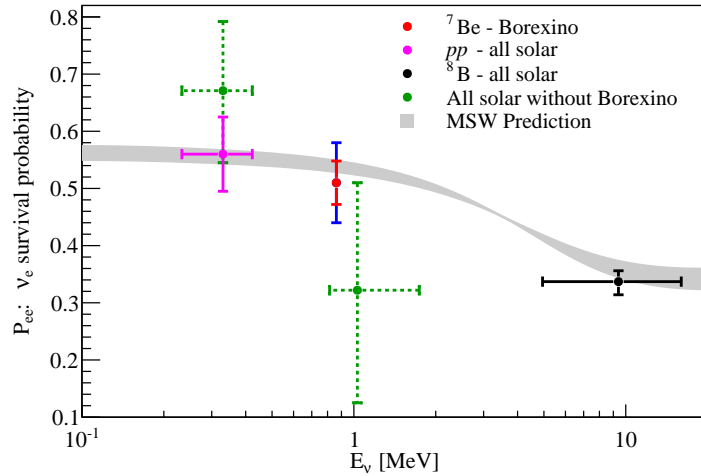


Figure 2.12: The global experimental constraints on the low energy solar P_{ee} . For the ${}^7\text{Be}$ point, which shows the current result, the inner (red) error bars show the experimental uncertainty, while the outer (blue) error bars show the total (experimental + SSM) uncertainty. The remaining points were obtained following the procedure in Ref. [56], wherein the survival probabilities of the low energy (pp), medium energy, and high energy (${}^8\text{B}$) solar neutrinos are obtained, with minimal model dependence, from a combined analysis of the results of all solar neutrino experiments. To illustrate Borexino's effect on the low energy P_{ee} measurements, the green (dashed) points are calculated without using the Borexino data. The MSW-LMA prediction is also shown for comparison; the band defines the 1σ range of the mixing parameter estimate in Ref. [7], which does not include the latest Borexino result.

2.8 Physics goals and achieved results

The data used in this analysis were collected between May 16th, 2007 and May 8th, 2010 and correspond to 740.88 live days after applying the data selection cuts. We define "day" and "night" using θ_z , the angle between the vertical z-axis of the detector (positive upward) and the vector pointing to the detector from the sun. The distance the neutrinos cross within the earth is small for negative $\cos\theta_z$ during "day" (~ 1.4 km LNGS overburden) and ranges up to 12,049 km for positive $\cos\theta_z$ during "night" (earth diameter).

The day-night asymmetry (A_{DN}) of the ${}^7\text{Be}$ count rate is defined as:

$$A_{\text{DN}} = 2 \frac{R_{\text{N}} - R_{\text{D}}}{R_{\text{N}} + R_{\text{D}}} = \frac{R_{\text{diff}}}{\langle R \rangle}, \quad (2.8)$$

where R_{N} and R_{D} are the ${}^7\text{Be}$ neutrino interaction rates during the night and the day, respectively, R_{diff} is their difference, and $\langle R \rangle$ is their mean. A strong constraint on A_{DN} can be set by making the reasonable assumption that the main backgrounds that limit the sensitivity (${}^{85}\text{Kr}$ and ${}^{210}\text{Bi}$, Ref. [1]) are the same during day and night. With this assumption, A_{DN} is obtained by subtracting the day and night spectra (normalized to the day live time) following the second term in Eq. 2.8 and then searching for a residual component having the shape of the electron recoil spectrum due to ${}^7\text{Be}$ neutrinos. We find:

$$A_{\text{DN}} = 0.001 \pm 0.012(\text{stat}) \pm 0.007(\text{syst}). \quad (2.9)$$

The details of this analysis are reported in Ref. [2].

2.8.3 ${}^8\text{B}$ neutrino flux measurement

In 2010, the Borexino collaboration released the measurement of ν_e elastic scattering from ${}^8\text{B}$ solar neutrinos with 3 MeV electron energy threshold (Ref. [4]). Borexino was the first experiment to succeed in suppressing all major backgrounds above the 2.614 MeV from the decay of ${}^{208}\text{Tl}$ to a rate below that of electron scattering from solar neutrinos. This allowed to reduce the kinetic energy threshold for scattered electrons by ${}^8\text{B}$ solar neutrinos to 3 MeV, the lowest so far reported for the electron scattering channel. Since Borexino also detected low-energy solar ${}^7\text{Be}$ neutrinos (see Sec. 2.8.1), that was the first time that a single experiment could measure simultaneously both branches of the solar pp-cycle in the same target. A complete description of the analysis can be found in Ref. [4]. The resulting count rate with $E > 3$ MeV is:

$$0.217 \pm 0.038(\text{stat}) \pm 0.008(\text{syst}) \text{ cpd}/100 \text{ ton} . \quad (2.10)$$

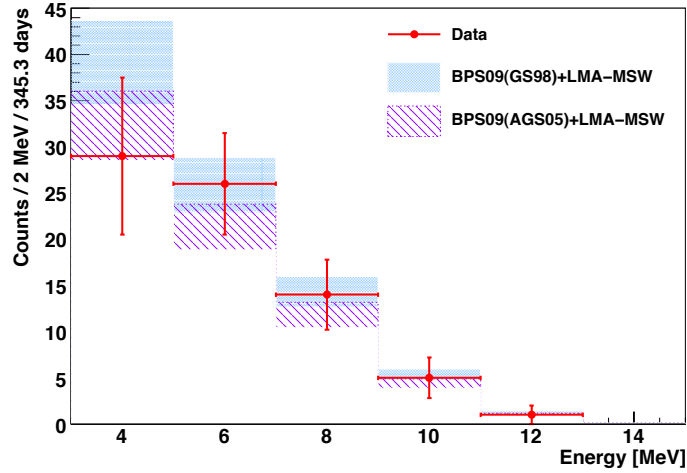


Figure 2.13: Comparison of the final electron energy spectrum after data selection and background subtraction (red dots) to Monte Carlo simulations (blue) of oscillated ^8B interactions, with amplitude from the Standard Solar Models BPS09(GS98) (Ref. [57, 58, 15], high metallicity) and BPS09(AGS05) (Ref. [57, 58, 16], low metallicity), and from the MSW-LMA neutrino oscillation model.

The analogous count rate with 5 MeV energy threshold is:

$$0.134 \pm 0.022(\text{stat}) \begin{matrix} +0.008 \\ -0.007 \end{matrix}(\text{syst}) \text{ cpd}/100 \text{ ton} . \quad (2.11)$$

The final energy spectrum (Fig. 2.13), after all cuts and residual background, is in agreement with the scenario which combines the standard solar model BPS09(GS98) (Ref. [57, 58]), and the prediction of the MSW-LMA solution. Moreover, we obtain $\langle P_{ee} \rangle = 0.29 \pm 0.10$ at the mean energy of 8.9 MeV for ^8B neutrinos. As for today, Borexino is the only experiment which can probe the MSW-LMA solution both in vacuum- and in matter-dominated regimes.

2.8.4 Pep neutrino flux measurement

In late 2011, the Borexino collaboration achieved the necessary sensitivity to provide evidence (Ref. [3]) of the rare signal from pep neutrinos and to place the strongest constraint on the CNO neutrino flux to date. This is the very first observation of solar neutrinos in the 1.0-1.5 MeV energy range and, until then, only fluxes from the pp chain have been measured (^7Be , ^8B , and, indirectly, pp).

2.8 Physics goals and achieved results

The detection of pep and CNO neutrinos is really challenging, as their expected interaction rates are few counts per day in a 100 ton target, ~ 10 times lower than that of ${}^7\text{Be}$ solar neutrinos. The electron recoil energy spectrum from pep neutrino interactions in Borexino is a Compton-like shoulder with end point of 1.22 MeV. The energy spectrum of neutrinos from the CNO cycle is the sum of three continuous spectra with end point energies of 1.19 (${}^{13}\text{N}$), 1.73 (${}^{15}\text{O}$) and 1.74 MeV (${}^{17}\text{F}$), close to the pep neutrino energy. The total CNO flux is similar to that of the pep neutrinos but its predicted value is strongly dependent on the inputs to the solar modeling, being 40% higher in the High Metallicity (GS98, Ref. [15]) than in the Low Metallicity (AGSS09, Ref. [17]) solar model (Ref. [18]).

Results from solar neutrino experiments are consistent with the MSW-LMA model (Ref. [59, 21, 60]), which predicts, for increasing energy, a transition from vacuum-dominated to matter-enhanced oscillations, resulting in an energy dependent ν_e survival probability, P_{ee} . Instead, non-standard neutrino interaction models formulate P_{ee} curves that deviate significantly from MSW-LMA, particularly in the 1-4 MeV transition region. From our analysis we extract: $P_{ee} = 0.62 \pm 0.17$, for $E_\nu = 1.44$ MeV.

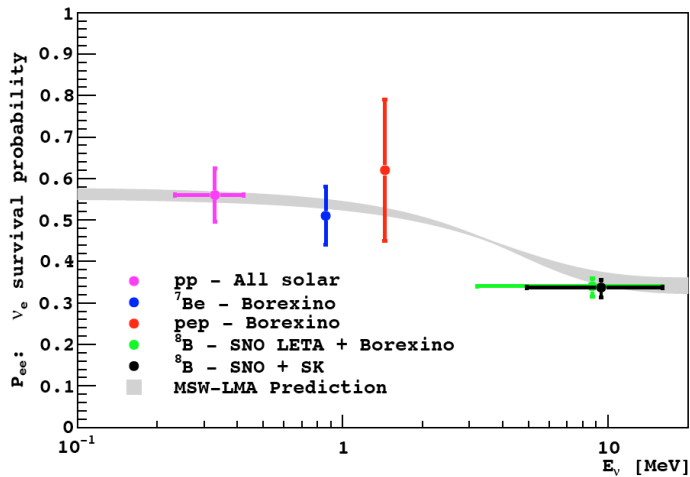


Figure 2.14: Electron neutrino survival probability as a function of energy. The red point corresponds to the Borexino pep measurement. The pp and ${}^7\text{Be}$ measurements of P_{ee} given in Ref. [1] are also shown. The ${}^8\text{B}$ measurements of P_{ee} were obtained from Borexino (Ref. [4]), SNO (Ref. [61, 34, 35, 37]), KamiokaNDE and Super KamiokaNDE (Ref. [31, 32, 33]), as indicated in the legend. The MSW-LMA prediction band is the 1σ range of the mixing parameters given in Ref. [7].

An ideal probe to test these competing hypotheses is the mono-energetic 1.44 MeV pep neutrino, which belong to the pp chain and whose predicted flux by the Standard Solar Model has one of the smallest uncertainties (1.2%) due to the solar luminosity constraint. The detection of neutrinos resulting from the CNO cycle has important implications in astrophysics, as it would be the first direct evidence of the nuclear process that is believed to fuel massive stars ($> 1.5 M_{\odot}$). Furthermore, its measurement may help to resolve the solar metallicity problem (see Ref. [18, 62]).

Some of the results so far obtained by the Borexino collaboration analysis are summarized in Tab. 2.5 and Fig. 2.14.

Neutrino source	Interaction rate [counts/(day·100 ton)]	Solar- ν flux [$10^8 \text{ cm}^{-2} \text{ s}^{-1}$]	Data/SSM ratio
pep	$3.1 \pm 0.6(\text{stat}) \pm 0.3(\text{syst})$	1.6 ± 0.3	1.1 ± 0.2
CNO	< 7.4	< 7.2	< 1.4

Table 2.5: The best estimates for the pep and CNO solar neutrino interaction rates. For the results in the last two columns, the errors are added in quadrature. Total fluxes have been obtained assuming MSW-LMA. The last column gives the ratio between our measurement and the High Metallicity Standard Solar Model (Ref. [18]).

2.8.5 Geo-neutrino observation

In spring 2010, the Borexino collaboration presented an observation of the geo-neutrino signal (Ref. [63]). Geo-neutrinos are electron anti-neutrinos ($\bar{\nu}_e$) produced in β decays of ^{40}K and of several nuclides in the chains of long-lived radioactive isotopes ^{238}U and ^{232}Th . Geo- $\bar{\nu}_e$ are direct messengers of the abundances and distribution of radioactive elements within the earth. By measuring their flux and spectrum it is possible to infer the distribution of long-lived radioactivity in the earth and to constraint the radiogenic contribution to the total heat balance of our planet.

Borexino detects anti-neutrinos via the inverse neutron β -decay ($\nu_e + p \rightarrow e^+ + n$) with a threshold of 1.806 MeV. Some $\bar{\nu}_e$ from the ^{238}U and ^{232}Th series are above threshold while those from ^{40}K decays are below threshold as can be seen in Fig. 2.15. The inverse β reaction produces out one prompt and one delayed event whose time and spatial coincidence offers a clean and unmistakable signature of $\bar{\nu}_e$ detection. This analysis relies on data collected between December 2007 and December 2009, corresponding to a lifetime of 537.2 days. The fiducial exposure after cuts is 252.6 ton·y and the main background is represented by $\bar{\nu}_e$ from far reactors.

2.8 Physics goals and achieved results

A total of 21 $\bar{\nu}_e$ candidates pass all the software selection cuts. Among those, fifteen candidates are in the geo- $\bar{\nu}_e$ energy window (see Fig. 2.16). The very good signal-to-background ratio and the clear separation of the two $\bar{\nu}_e$ sources (geo-neutrinos and reactor $\bar{\nu}_e$) permit a clear identification of the number of events belonging to each source, and allow to establish observation of the geo-neutrinos.

Our best estimates are $N_{\text{geo}} = 9.9_{-3.4}^{+4.1} \left({}_{-8.2}^{+14.6} \right)$ and $N_{\text{react}} = 10.7_{-3.4}^{+4.3} \left({}_{-8.0}^{+15.8} \right)$ at 68.3% C.L. (99.73% C.L.). Scaling the best estimate of N_{geo} with the fiducial exposure, we obtain the measurement for the geo-neutrinos rate: $3.9_{-1.3}^{+1.6} \left({}_{-3.2}^{+5.8} \right)$ events/(100 ton·y), to be compared with typical predictions of $N_{\text{geo}} \sim 2.5$ events/(100 ton·y) from BSE¹-based earth models (Ref. [64, 65]).

By studying the profile of the log-likelihood with respect to N_{geo} , we calculated that the null hypothesis for geo-neutrinos can be rejected at 99.997% C.L. that means that we establish observation of geo-neutrinos at 4.2σ .

¹BSE is Bulk Silicate Earth

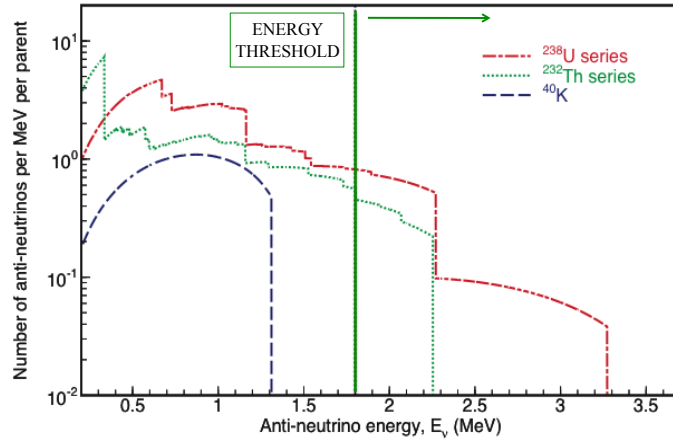


Figure 2.15: The theoretical spectrum of geo-neutrinos incident on terrestrial neutrino experiments.

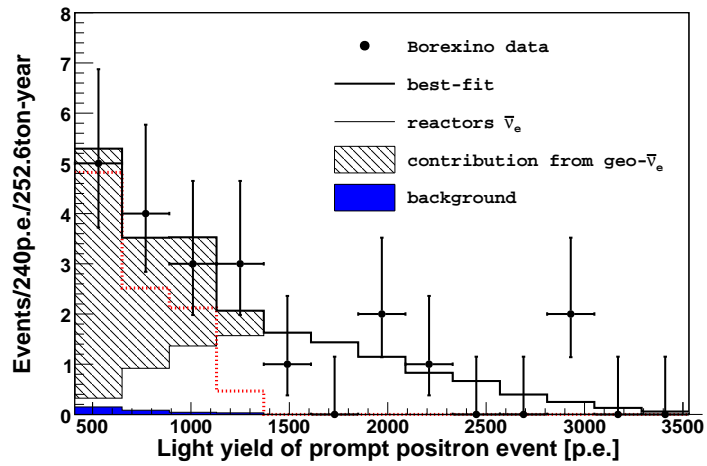


Figure 2.16: The light yield spectrum for the positron prompt events of the 21 $\bar{\nu}_e$ candidates and the best fit obtained with the unbinned likelihood analysis. The red dotted line describes the geo- $\bar{\nu}_e$ signal resulting from another fitting procedure. The conversion factor is approximately 500 p.e./MeV (Ref. [63].)

Chapter 3

Toward the global analysis: the method

The work presented in this thesis is the result of several global analysis performed on different neutrino data-sets.

All the analyses are carried out by building a χ^2 -based comparison of the experimental results coming from the different solar, reactor, accelerator and atmospheric neutrino experiments (see Sec. 3.2), with the respective theoretical expectations, calculated as a function of the oscillation parameters (Δm_{21}^2 , θ_{12} , θ_{13}) and of the SSM neutrino fluxes (Φ_i).

The individual analyses differ, for example, in the input data (including cases before and after the recent announcement of the Borexino ${}^7\text{Be}$ and A_{DN} measurements), in the different constraints placed on the neutrino fluxes (e.g. with or without the luminosity constraint), in the number of neutrino fluxes that are treated as free variables, and in the different assumptions made about future solar neutrino experiments.

The main goal is to understand the implications of present and future results of Borexino on the physics of neutrino and on the astrophysics of the sun.

In this contest, a reference work was previously done by John Bahcall and Carlos Peña Garay, and reported in the paper “A roadmap to solar neutrino fluxes, neutrino oscillation parameters and tests for new physics” (Ref. [66]).

The experiments other than Borexino that we take into account in the analysis are Homestake, GALLEX/GNO, SAGE, Super Kamiokande, SNO and KamLAND.

The analysis method can be summarized in three computational steps:

1. **Calculation of the P_{ee}** , the survival probability of an electron neutrino, at each experiment site, as a function of $\frac{\Delta m_{21}^2}{4E}$, $\tan^2 \theta_{12}$ and $\sin^2 \theta_{13}$ parameters.

3.1 Survival probability computation

2. **Calculation of the expected results** for each solar or reactor neutrino experiments.
3. **χ^2 calculation.** The theoretical expectations derived in step 1 and 2 are compared with the experimental results and the χ^2 is calculated taking into account both theoretical and experimental errors.

3.1 Survival probability computation

Neutrino flavor oscillations induced by ν mass and mixing are today well established. In particular, for what concerns solar neutrinos, we now know that, depending on the mass and mixing parameters, the dominant flavor conversion can occur either in vacuum (see Sec. 1.5.1) or in matter (see Sec. 1.5.3). The calculation of the survival probability for solar neutrinos requires therefore to propagate the neutrino mass eigenstates from the sun core to the earth, taking into account both vacuum and matter terms.

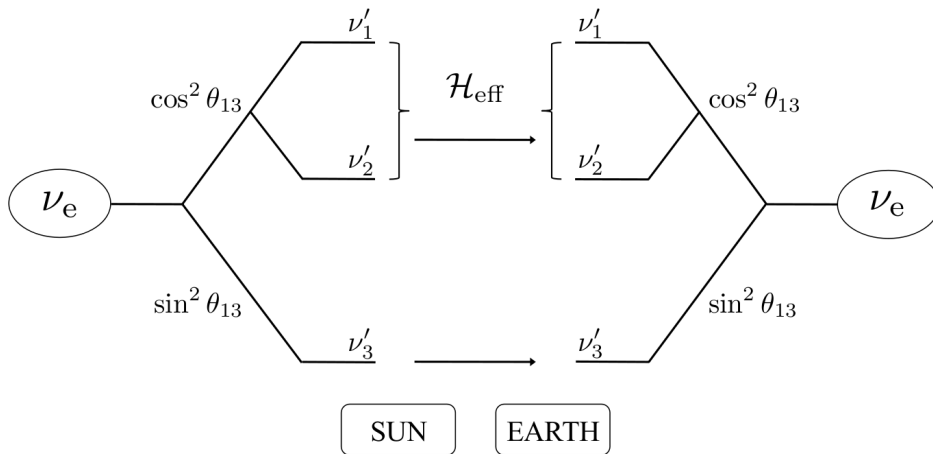


Figure 3.1: Scheme of neutrino flavor eigenstate evolution. Propagation of an electron neutrino from the sun core to the earth.

Assuming the standard three-neutrino framework and the energy range of solar neutrinos, it is possible to perform an effective three-flavor analysis by reducing (Ref. [67, 68]) the traditional Hamiltonian to a 2×2 matrix: the *effective Hamiltonian*, \mathcal{H}_{eff} .

$$\mathcal{H}_{\text{eff}} = \begin{pmatrix} -\frac{\Delta m_{21}^2}{4E} \cos 2\theta_{12} + \frac{\sqrt{2}}{2} G_F n_e \cos^2 \theta_{13} & \frac{\Delta m_{21}^2}{4E} \sin 2\theta_{12} \\ \frac{\Delta m_{21}^2}{4E} \sin 2\theta_{12} & \frac{\Delta m_{21}^2}{4E} \cos 2\theta_{12} - \frac{\sqrt{2}}{2} G_F n_e \cos^2 \theta_{13} \end{pmatrix}. \quad (3.1)$$

The effective Hamiltonian for three-neutrino propagation in matter can be conveniently written in the familiar form of Eq. 3.1 and its action over the relevant two-neutrino subsystem can be summarized as in Fig. 3.1.

As seen in Eq. 1.38 of Sec. 1.5.3, the survival probability of an electron neutrino can be written as:

$$P_{ee}^{3\nu} = \sin^4 \theta_{13} + \cos^4 \theta_{13} P_{ee}^{2\nu}, \quad (3.2)$$

where $P_{ee}^{2\nu} = |\langle \nu_e | \mathcal{H}_{eff} | \nu_e \rangle|^2$.

In order to proceed in a three-flavor analysis, we first have to compute the survival probability in the two-neutrino mixing case; the third flavor will then enter via the fourth powers in cosinus and sinus of θ_{13} (Eq. 3.2), as well as via the $\cos^2 \theta_{13}$ factor of Eq. 3.1.

In scheme Fig. 3.1, ν'_i ($i=1,2,3$) is an intermediate basis defined via two rotations, $\mathcal{R}(\theta_{13})$ and $\mathcal{R}(\theta_{23})$, respect to the usual flavor basis (Ref. [67, 68]). Using this new ‘‘primed’’ basis, the neutrino propagation from the sun core to a detector in the earth is thought as if the original ν_e can take two paths: the $\nu_e \rightarrow \nu'_1$ and the $\nu_e \rightarrow \nu'_2$ intermediate transitions.

We know (Ref. [69]) that, in the two-neutrino mixing case, the survival amplitude for a solar electron neutrino of energy E can be written as:

$$A_{ee} = \sum_{i=1,2}^2 A_{ei}^S A_{ie}^E \exp \left[-i \frac{1}{2E} m_i^2 (L - r) \right]. \quad (3.3)$$

Here, A_{ei}^S is the amplitude of the transition $\nu_e \rightarrow \nu_i$ (being ν_i the pure i -mass eigenstate) from the production point to the sun surface; A_{ie}^E is the amplitude of the transition $\nu_i \rightarrow \nu_e$ from the earth surface to the detector. The propagation in vacuum from the sun to the surface of the earth is given by the exponential: L is the averaged distance between the center of the sun and the surface of the earth while r is the distance between the neutrino production point (see Sec. 3.1.1) and surface of the sun.

3.1 Survival probability computation

The corresponding survival probability $P_{ee}^{2\nu}$ is then given by:

$$P_{ee}^{2\nu} = P_{e1}^S P_{1e}^E + P_{e2}^S P_{2e}^E + 2 \cos \xi \sqrt{P_{e1}^S P_{e2}^S P_{1e}^E P_{2e}^E}. \quad (3.4)$$

where $P_{ei}^S = |A_{ei}^S|^2$ and $P_{ie}^E = |A_{ie}^E|^2$. Unitarity implies $P_{1e}^E + P_{2e}^E = 1$ and $P_{e1}^S + P_{e2}^S = 1$ so it is possible to derive an expression of the survival probability as a function of P_{e1}^S and P_{2e}^E only.

P_{e1}^S (hereafter called P^S) is the probability that an electron neutrino produced in the sun becomes a neutrino mass eigenstate ν_1 , while P_{2e}^E (hereafter called P^E) is the probability that a neutrino propagating in vacuum as mass eigenstate ν_2 is detected on earth as an electron neutrino. In other words,

$$P_{ee}^{2\nu} = P^S (1 - P^E) + (1 - P^S) P^E + 2 \cos \xi \sqrt{P^S (1 - P^E) (1 - P^S) P^E}. \quad (3.5)$$

The phase ξ is given by:

$$\xi = \frac{\Delta m_{21}^2}{2E} (L - r) + \delta,$$

where δ contains the phases due to propagation in the sun and in the earth and can be safely neglected. In the evaluation of both P^S and P^E , the effect of coherent interaction with the sun and earth matter must be taken into account.

Starting from the considerations done so far, it is helpful to recover more familiar expressions for the survival probability.

- For $\Delta m^2/E < 5 \times 10^{-17}$ eV, the matter effect suppresses flavor transitions both in the sun and in the earth. Consequently, the probabilities P^S and P^E are simply the projections of the ν_e state onto the mass eigenstates and the survival probability $P_{ee}^{2\nu}$ is expressed via the standard formula:

$$P_{ee}^{\text{vac}} = 1 - \sin^2 2\theta_{12} \sin^2 \left[\frac{\Delta m_{21}^2}{4E} (L - r) \right], \quad (3.6)$$

which describes the oscillations on the way from the surface of the sun to the surface of the earth. This probability is symmetric under the change of octant and the change of mass sign so it is possible to take $\Delta m_{21}^2 > 0$ and $0 < \theta_{12} < \frac{\pi}{2}$ without loss of generality.

Since the earth-sun distance changes during an orbital period T (see Sec. 2.6.1), one should consider $L = L(t)$ rather than a constant $L = L_{\text{avg}}$ value. In particular:

$$L(t) = L_{\text{avg}} \left[1 - \epsilon \cos \left(\frac{2\pi t}{T} \right) \right].$$

Averaging Eq. 3.6 over the earth-sun distance $L(t)$ the final expression of $P_{ee}^{2\nu}$ becomes:

$$\langle P_{ee}^{\text{vac}} \rangle = 1 - \sin^2 2\theta_{12} \left[1 - \cos \left(\frac{\Delta m_{21}^2}{2E} L_{\text{avg}} \right) J_0 \left(\epsilon \frac{\Delta m_{21}^2}{2E} L_{\text{avg}} \right) \right], \quad (3.7)$$

where $\epsilon = 0.0167$ is the terrestrial orbit eccentricity and J_0 is the Bessel- J_0 function.

- For $\Delta m^2/E > 10^{-14}$ eV, the last term of Eq. 3.5 vanishes and the incoherent MSW survival probability is recovered: P^S and P^E must be obtained by solving the equation of the neutrino states in the sun and in the earth matter respectively.

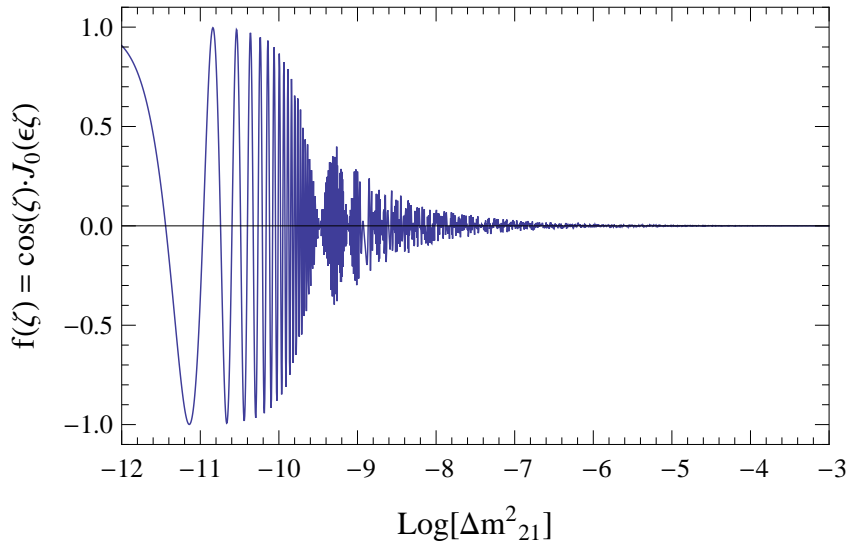


Figure 3.2: The oscillating term $f(\zeta)$ of Eq. 3.8 as a function of Δm_{21}^2 , being $\zeta = \frac{\Delta m_{21}^2}{2E} L_{\text{avg}}$. The curve is obtained by assuming $E = 1$ MeV and $\tan^2 \theta_{12} = 1$.

Figure 3.2 shows the trend analysis of the oscillating term:

$$f(\zeta) = \cos(\zeta) \cdot J_0(\epsilon \zeta), \quad \zeta = \frac{\Delta m_{21}^2}{2E} L_{\text{avg}}. \quad (3.8)$$

3.1 Survival probability computation

The curve is obtained by assuming a typical solar neutrino energy $E = 1$ MeV and $\tan^2 \theta_{12} = 1$. It can be noticed that the variation of the distance earth-sun is not negligible in case of $\Delta m_{21}^2 \leq 10^{-7} \text{ eV}^2$ (i.e. in the Quasi-Vacuum and Vacuum regimes) while it averaged out to zero for $\Delta m_{21}^2 \gg 10^{-7} \text{ eV}^2$, i.e., in the MSW region.

In conclusion, from a practical point of view, the survival probability is computed by dealing separately P^S and P^E . These two quantities are evaluated for each set of oscillation parameters $\frac{\Delta m_{21}^2}{4E}$, $\tan^2 \theta_{12}$ and $\sin^2 \theta_{13}$.

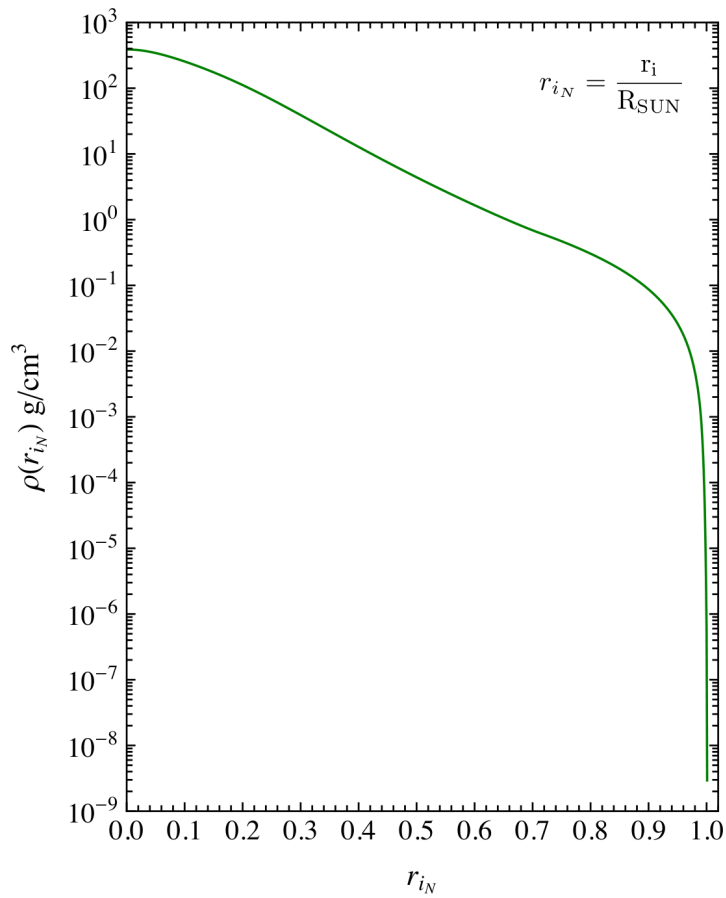


Figure 3.3: Solar density profile as a function of the normalized solar radius r_{iN} (Ref. [70, 71, 72, 73, 74]).

3.1.1 Survival probability: the sun contribution

The propagation of the survival probability of electron neutrinos in the Sun, the P^S , is evaluated by using the effective Hamiltonian of Eq. 3.1.

The code built to this purpose uses as input the sun radial density distribution $\rho(r)$, (Fig. 3.3), as given by the Standard Solar Model (Ref. [70, 71, 72, 73, 74]). The sun is divided in about 1000 shells in which the density $\rho(r_i)$ is assumed to be reasonably constant. All the r_i radii are normalized respect to the radius of the sun R_{SUN} : the normalized radius is named r_{i_N} .

For each set of θ_{13} , $\tan^2 \theta_{12}$ and $\frac{\Delta m_{21}^2}{4E}$ parameters and for each solar neutrino source, the code computes $\mathcal{H}_{\text{eff}}[\rho(r_i)]$ and iterates for all r_i greater than that of the neutrino production point.

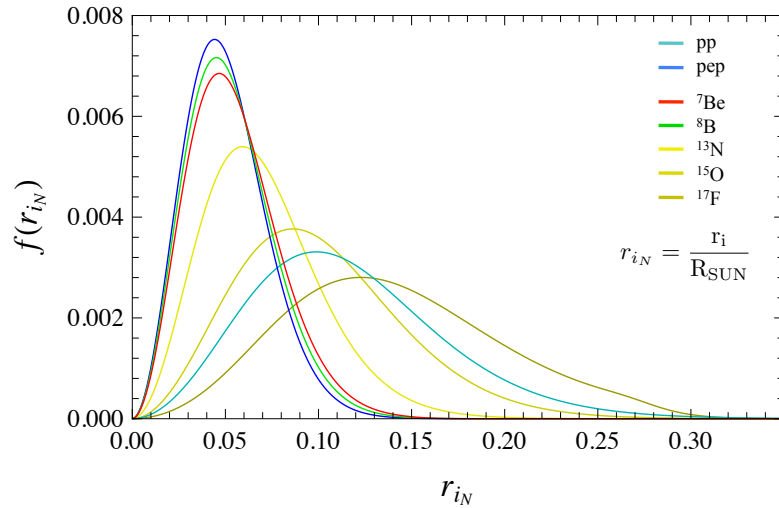


Figure 3.4: Production points distribution for some of the solar neutrinos as function of the normalized solar radius r_{i_N} . In cyan, the pp neutrinos; in blue, the pep neutrinos; in red, the ${}^7\text{Be}$ neutrinos; in green, the ${}^8\text{B}$ neutrinos; in yellow scale, the CNO neutrinos.

For each solar neutrino source, in order to obtain P^{S} , we sum the contribution of all the neutrino production volumes. This is performed by integrating the neutrino conversion probability over all the neutrino radii, starting in $r_{i_N} = 0$, $\vartheta = 0$, weighted for the SSM 1D production points distribution $f(r_{i_N})$ of Fig. 3.4, and using the spherical symmetry on the remaining part of the angle ϑ which lies in the plane perpendicular to the trajectory.

3.1.2 Survival probability: the earth contribution

The calculation of P^{E} is notoriously difficult since the electron density in the earth is not a simple function of the radius, and the P_{ee} has to be averaged over given intervals

3.1 Survival probability computation

of time. The method we adopt in computing P^E consists in propagating the effective Hamiltonian in terrestrial shells characterized by a constant density, and then weighting the P_{ee} for the *solar exposure* of the trajectory corresponding to the nadir angle θ_z (Ref. [75]). From a practical point of view, to calculate the neutrino regeneration probability, we consider small segments of a circumference string (see Fig. 3.5) that is we select shells in which the earth density can be assumed constant. We integrate numerically the evolution equation in earth matter using the earth density profile (Fig. 3.6) given in the Preliminary Reference Earth Model (PREM, Ref. [76]). The density is symmetrical about the midpoint of the diameter \overline{AB} , so the propagation of the effective Hamiltonian can be limited to only half of \overline{AB} .

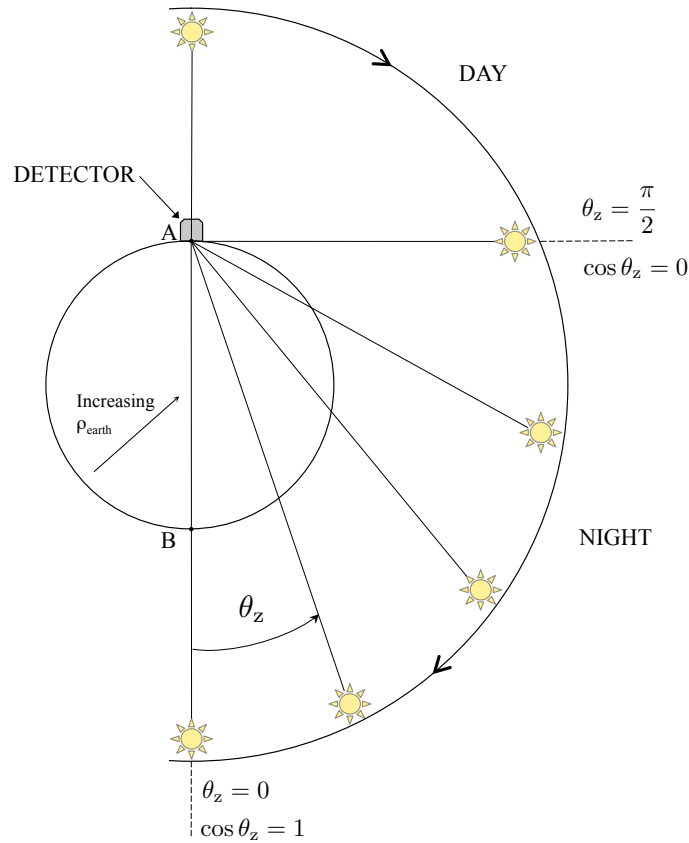


Figure 3.5: Pictorial representation of the earth: day and night period are defined as function of the nadir angle θ_z .

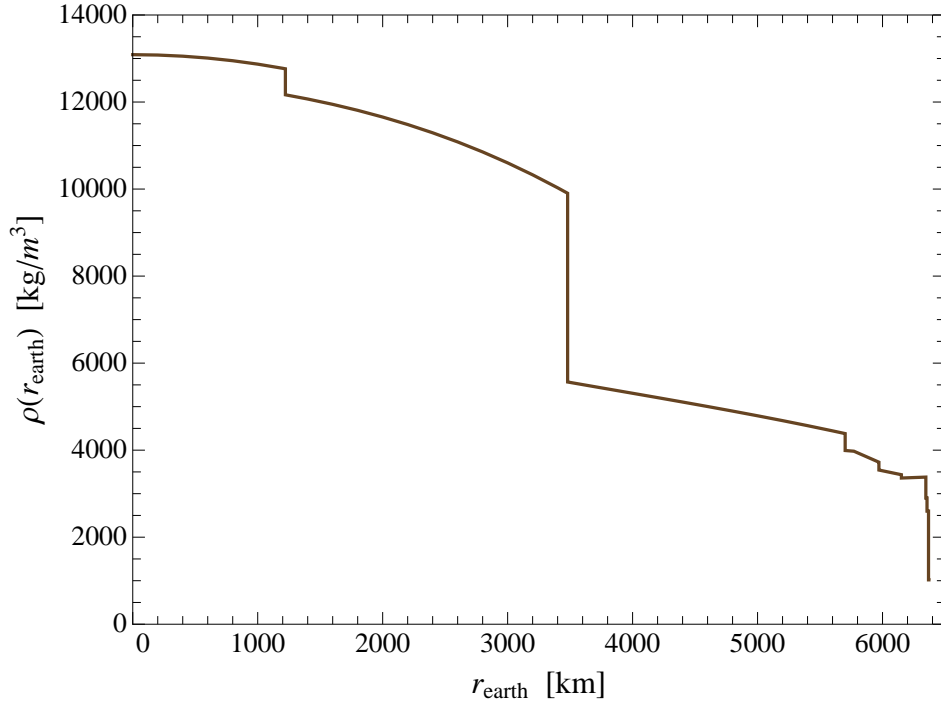


Figure 3.6: Earth density profile according to the Preliminary Reference Earth Model (PREM, Ref. [76]).

For each angular bin then, the P^E has to be weighted for the exposure correspondent to the latitude of the experiment site. In Fig. 3.7, it is shown the solar exposure for the SNO experiment (Lat. 46.50° ; location: Sudbury, CA), the Borexino and GALLEX/GNO experiments (Lat. 42.19° ; location: LNGS, L'Aquila, IT), the Super Kamiokande and KamLAND experiments (Lat. 36.42° ; location: Kamioka, JP).

For all experiments except for Borexino, we use the ideal zenith exposure. In the Borexino case, it is possible to use the experimental exposure function, weighted by the real live time: the comparison of the experimental exposure respect to the expected theoretical function is reported in Fig. 3.8.

Finally, the probability P^E , as previously for P^S , is given as a function of $\sin^2\theta_{13}$, $\tan^2\theta_{12}$ and $\frac{\Delta m_{21}^2}{4E}$. Three separated outputs are generated for the different latitudes of the real-time experiments sites.

3.1 Survival probability computation

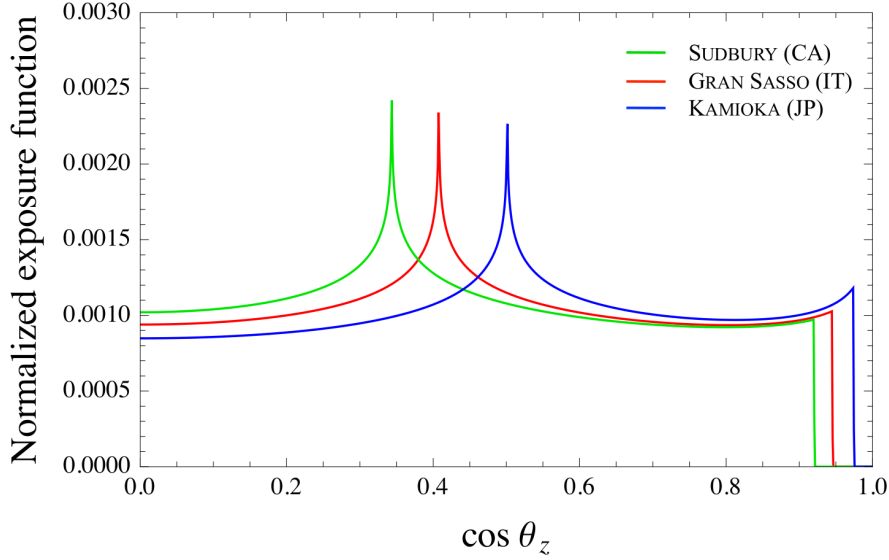


Figure 3.7: Annual average of the solar exposure as a function of the nadir angle θ_z . In green, the theoretical solar exposure at Sudbury, CA (Lat. 46.50°); in red, the theoretical solar exposure at L'Aquila, IT (Lat. 42.19°); in blue, the theoretical solar exposure at Kamioka, JP (Lat. 36.42°).

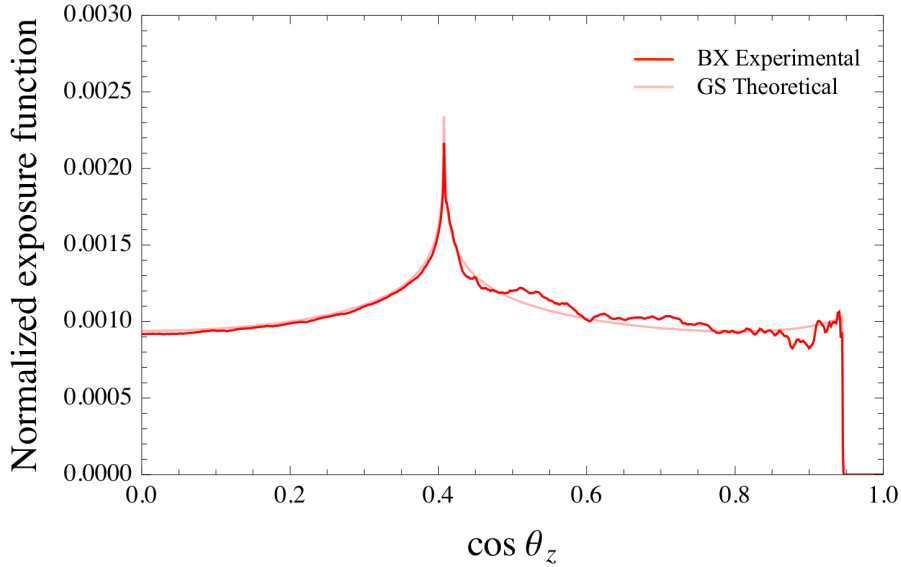


Figure 3.8: Comparison between the expected solar exposure (light red) and the experimental solar exposure (red) for the Borexino experiment. The red curve is obtained by weighting the Gran Sasso solar exposure for the real live time of the experiment.

The latitudes of the Homestake (South Dakota, US, Lat. $\sim 44^\circ$) and SAGE (Baksan, RU, Lat. $\sim 43^\circ$) experiments differ for less than 2° from that of the GALLEX/GNO experiment (LNGS, L'Aquila, IT, Lat. $\sim 42^\circ$). We verified that the relative analyses were not sensitive to such a small angular change and we chose the Gran Sasso theoretical exposure as common exposure function for the three radiochemical experiments.

3.2 Experimental input data

As already mentioned, in this Ph.D. thesis we use up-to-date neutrino experimental results. More precisely, we include data coming from Borexino, Homestake, GALLEX/GNO, SAGE, Super Kamiokande, SNO, and KamLAND experiments.

A detailed discussion about the solar experiments, their techniques and their results has been given in Sec. 1.6. Here a short summary follows. The radiochemical experiments contributions enter the analysis with the Homestake chlorine results (Ref. [25]) and the gallium data. The latter is an average of the latest results from SAGE (Ref. [30]) and the joint analysis of GALLEX/GNO data (Ref. [29]).

The Borexino experiment contributes with the ${}^7\text{Be}$ neutrino interaction rate, its related A_{DN} measurement (Ref. [1, 2]) and the pep neutrino rate (Ref. [3]). Moreover, the ${}^8\text{B}$ neutrino rate above 3 MeV and the spectral shape associated (Ref. [4]) are also included.

For what concerns the SNO experiment, we include the results coming from the Low Energy Threshold Analysis (LETA, Ref. [35]) and Phase III data (Ref. [77]). In LETA analysis, the SNO collaboration performs a signal extraction fit in which the free parameters directly describe the total ${}^8\text{B}$ neutrino flux, the energy-dependent survival probability P_{ee} and the A_{DN} measurement.

The Super Kamiokande experiment is included in the analysis with its observed ${}^8\text{B}$ event rate in phase I (Ref. [31]) and phase III (Ref. [33]).

Finally, for what concerns the reactor experiments, we include as input to our analysis the published result on the $\bar{\nu}_e$ survival probability from the KamLAND collaboration (Ref. [38]).

Contributions from atmospheric, reactor (CHOOZ experiment only), and long-baseline (LBL) accelerator experiments are relevant only for what concerns the θ_{13} determination. For non-solar neutrino data we refer to, and directly use, the results of the analysis done by M. Gonzalez-Garcia *et al.*, reported in Ref. [78]. This analysis includes the electron neutrino appearance as well as the anti-neutrino data from the MINOS long-baseline experiment, and it is in good agreement with other similar analyses performed by different group as in Ref. [79].

3.3 Computation of the expected results

3.3 Computation of the expected results

Starting from the two components of the survival probability so far calculated (P^E and P^S), the theoretical predictions for each experiment relevant quantities are evaluated as a function of the free parameters of the fit: the oscillation parameters $\sin^2 \theta_{13}$, $\tan^2 \theta_{12}$, and Δm_{21}^2 .

Regarding the radiochemical experiments (i.e. Homestake and the gallium experiments), we compute the theoretical prediction of the rate (in SNU¹) for solar neutrinos whose energy lies above the experiment threshold.

For the Borexino experiment, we evaluate the expected rate, normalized to that of the non-oscillating case for ${}^7\text{Be}$, pep and ${}^8\text{B}$ solar neutrino. Moreover, discriminating between day and night P^E contribution, we compute the potential ${}^7\text{Be}$ signal for a day-night asymmetry. The shape of the expected ${}^8\text{B}$ recoil energy spectrum is also evaluated in a 5 bin energy distribution: 3-5 MeV, 5-7 MeV, 7-9 MeV, 9-11 MeV, and 11-13 MeV.

For what concerns the Super Kamiokande experiment, the hep and ${}^8\text{B}$ expected rates are normalized to the non-oscillating case and the spectral shapes are calculated for both Phase I and Phase III, according to the day-night energy format of Ref. [31, 33].

Concerning the SNO experiment, the expected total rates in case of neutral current and charged current interactions are evaluated.

In general, the rate is computed taking into account all possible neutrino contributions, that is assuming that not only neutrino from the pp chain but also from the CNO cycle are emitted by our sun.

The cross section of each experiment is evaluated according to Ref. [80, 81]. At this level we also include the experiment energy resolution therefore a convolution between resolution and cross section is needed.

3.4 The statistical approach

In this work, the constraints on the parameters of the global analysis are obtained by fitting the theoretical prediction to the experimental data via χ^2 -method.

The parameter estimation is obtained by finding the minimum of the χ^2 -function and by tracing iso- $\Delta\chi^2$ contours around it. We adopt the convention of calling “*allowed region*” at $(1 - \alpha)\%$ C.L. or at $n\text{-}\sigma$, the subset of the parameter space obeying to the inequality:

$$\Delta\chi^2 \leq l(m), \quad (3.9)$$

where the set of $l(m)$ values depends and varies according to the number m of parameters

¹Solar Neutrino Unit: 1 SNU = 10^{-36} captures/atom/sec.

involved in the estimation i.e. according to the degrees of freedom (d.o.f.) of the fit. Table 3.1 reports some statistical common values of $l(m)$ as defined in Ref. [7].

From a practical point of view, if $R_{\text{EXP}}^{i,A}$ is the set of results of the i measurement actually obtained by the A experiment, and $R_{\text{THEO}}^{i,A}(\Delta m_{21}^2, \tan^2 \theta_{12}, \sin^2 \theta_{13}, \Phi_{\nu,A})$ is the corresponding set of theoretical predictions, then the χ^2 of the experiment A is defined as it follows:

$$\chi_A^2 = \left[R_{\text{EXP}}^{i,A} - R_{\text{THEO}}^{i,A}(\Delta m_{21}^2, \theta_{12}, \theta_{13}, \Phi_{\nu,A}) \right] \sigma_{ij}^{-2} \left[R_{\text{EXP}}^{j,A} - R_{\text{THEO}}^{j,A}(\Delta m_{21}^2, \theta_{12}, \theta_{13}, \Phi_{\nu,A}) \right] \quad (3.10)$$

The error matrix σ_{ij} includes both the theoretical and experimental errors as well as the cross-correlations between errors on the different parameters.

The resulting χ^2 is then marginalized over Δm_{21}^2 , $\tan^2 \theta_{12}$ and $\sin^2 \theta_{13}$: in this way we obtain the χ^2 projection for each parameter of the fit.

n- σ	(1 - α) %	m = 1	m = 2	m = 3
1σ	68.27	1.00	2.30	3.53
	90.00	2.71	4.61	6.25
	95.00	3.84	5.99	7.82
2σ	95.45	4.00	6.18	8.03
	99.00	6.63	9.21	11.34
3σ	99.73	9.00	11.83	14.16

Table 3.1: $l(m)$ values corresponding to a $(1-\alpha)$ coverage probability and to $n - \sigma$, for joint estimation of m parameters (Tab. 33.2 of Ref. [7]).

Chapter 4

Analysis of Borexino data

The main topic developed in this chapter is the impact of the Borexino measurements in the scenario of the global analysis of neutrino data. From this perspective, we separately study each piece of information coming from the Borexino experiments. As explained in Chap. 3, this study is performed through a fit which takes into account the experimental errors, their cross correlations (if any) and the related theoretical errors, associated to the SHP11 solar model (Ref. [18]).

Even if Borexino was designed for the real-time detection of ${}^7\text{Be}$ solar neutrinos at 862 keV, it turned out to be a very powerful experiment being able to detect also the higher energy ${}^8\text{B}$ and pep neutrinos. A detailed description of the main Borexino results is given in Sec. 2.8, while a schematic list of the Borexino observables, together with their reference papers, is given in Tab. 4.1.

We present the global analysis of the Borexino data following the detector's history: at first, the ${}^7\text{Be}$ result only is analyzed, then the ${}^8\text{B}$ results (both the total rate above 3 MeV and the relative spectral shape) are introduced. The day-night asymmetry measurement and the latest pep neutrino rate are afterwards included.

All the analysis are performed assuming the high metallicity hypothesis (Tab. 1.2) of the SHP11 standard solar model.

Even though today the actual oscillations solution is established (Ref. [38]) to belong to the Large Mixing Angle MSW regime, we carry out the analysis in an enlarged range of parameters in order to study the full Borexino potential: we want to consider all the possible oscillation solutions either in the Mikheyev-Smirnov-Wolfenstein regime or in the Vacuum regime, without relying on any other solar or reactor experiments results and without assuming CPT invariance.

We let Δm_{21}^2 vary between 10^{-12} eV² and 10^{-3} eV² in a 1801 points grid (200 points per decade) while the mixing angle θ_{12} is studied by letting $\tan^2 \theta_{12}$ vary between 10^{-4}

4.1 The berillium contribution

Observable	NoD ^a	Release	References
⁷ Be rate,	1	2011	[1]
⁷ Be signal A _{DN} ,	1	2011	[2]
<i>pep</i> neutrino rate,	1	2011	[3]
⁸ B total rate, ^b	1	2010	[4]
⁸ B spectral shape	5		

^a NoD is the Number of Data we add to our global analysis.

^b ⁸B total rate above 3 MeV.

Table 4.1: Summary of the Borexino experimental data used as input to the global analysis.

and 10, in a 1001 points grid (again, 200 points per decade). Although the analysis has been performed for different θ_{13} values, we directly report only the plots concerning the $\theta_{13}=0$ analysis and we report the complete list of the fit outputs in Tab. A.1 of the Appendix.

Here and in the following chapter we will use some acronyms in referring to the possible oscillation solutions (Sec. 1.8). In particular, we will refer to the Large Mixing Angle solution as LMA, to the Small Mixing Angle as SMA and to the LOW solution as LOW. The Quasi-Vacuum, the Vacuum solutions will be respectively indicated with QV and VAC.

4.1 The berillium contribution

The Borexino collaboration recently presented a new ⁷Be neutrino flux measurement with a total uncertainty below 5% (Ref. [1]). The best value for the interaction rate of 862 keV ⁷Be solar neutrinos is:

$$46.0 \pm 1.5(\text{stat}) \begin{matrix} +1.5 \\ -1.6 \end{matrix}(\text{syst}) \text{ cpd}/100 \text{ ton} .$$

For the first time, the experimental uncertainty (4.8%) is smaller than the theoretical uncertainty (about 7% according to Ref. [18]).

Before studying the effect of the inclusion of the ${}^7\text{Be}$ neutrino flux measurement in the fit, it is interesting to evaluate how this result compares with the expectation inferred from a global analysis of the data coming from the other solar neutrino experiments, together with the high-metallicity SHP11 neutrino fluxes predictions (Ref. [18]), and the Kamland experiment. A complete description of this global analysis is given in Sec. 5.3 while details on the data we include and the SHP11 model can be found in Tab. 5.1 and Tab. 1.2 respectively.

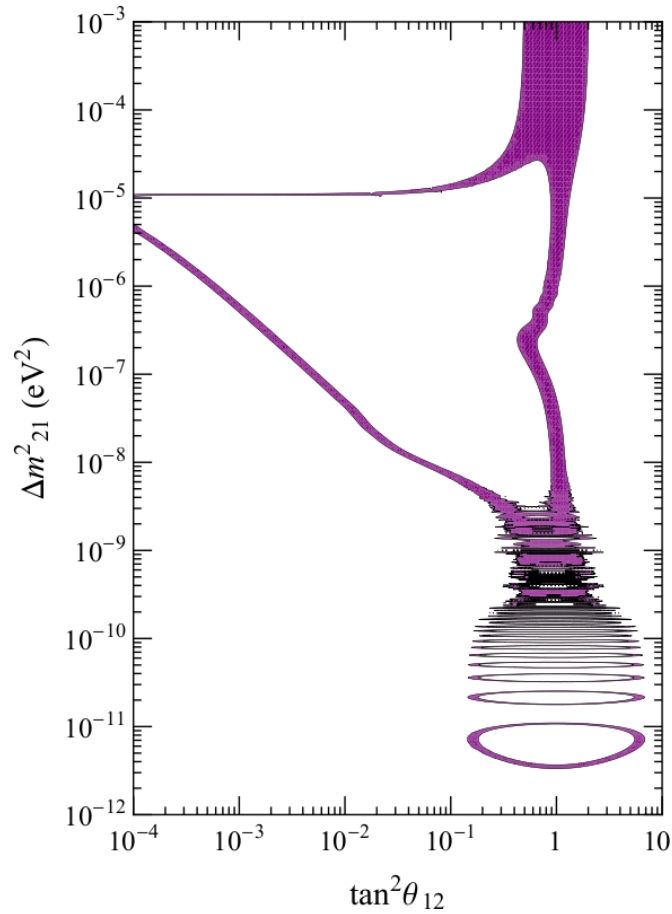


Figure 4.1: Iso-contours for the current Borexino ${}^7\text{Be}$ neutrino flux result [1] at $\pm 1\sigma$ experimental error only.

We consider as oscillation parameters the best fit coming from the analysis reported in Sec. 5.3, and we let them vary within 1σ , that is:

$$\Delta m_{21}^2 = 7.50^{+0.18}_{-0.22} \times 10^{-5} \text{ eV}^2 \quad \text{and} \quad \tan^2 \theta_{12} = 0.462^{+0.037}_{-0.033}.$$

4.1 The berillium contribution

If all the neutrinos remained ν_e , the prediction from the SHP11 model would yield an interaction rate of 74.0 ± 5.2 cpd/100 ton for the ${}^7\text{Be}$ neutrinos in Borexino.

Assuming the high metallicity SHP11 neutrino fluxes with their relative errors, we get the expected rate of:

$$47.7 \pm 3.4 \text{ cpd/100 ton.}$$

This value is perfectly consistent with the actual Borexino result.

Starting from the rate calculations described in Sec. 3.3, it is possible to plot the iso-contours lines in the $\tan^2 \theta_{12} - \Delta m_{21}^2$ space for any Borexino result.

After computing the survival probabilities P^S and P^E as discussed in Sec. 3.1, the expected rate is evaluated considering several factors related to the nature and to the energy of the ${}^7\text{Be}$ neutrino emission. First of all, we take into account the smearing of the berillium line: even if it is a monochromatic emission, it cannot be assumed as a perfect delta due to the Doppler thermal shift (Ref. [82]). A second aspect we consider is the branching ratio of the decay: of all the ${}^7\text{Be}$ electron capture, only the 90.7% results in the emission of a 862 keV electron neutrino. Finally, we obviously take into account the cross section of the process, convolved with the detector resolution.

Figure 4.1 shows the iso-contours lines for the maximum and minimum flux allowed at 1σ (experimental error only) by the latest Borexino ${}^7\text{Be}$ measurement: the coloured region indicates the fraction of the space of parameters authorized at 68.27% C.L.. Unfortunately, the impact of the actual Borexino ${}^7\text{Be}$ result is smoothed out by the fact that the ${}^7\text{Be}$ neutrino flux prediction has a relatively large theoretical error. This effect becomes evident when the theoretical error is added to the analysis and the χ^2 -computation is performed: the plot in Fig. 4.2 shows the allowed regions ($d.o.f. = 2$) at 68,27% C.L., 95.45% C.L. and 99.73% C.L., reported in pink, green and blue color respectively.

The χ^2 -fit clearly indicates that when including its ${}^7\text{Be}$ result only, the Borexino experiment cannot be significant in discriminating the allowed regions of the space of parameters ($\tan^2 \theta_{12}, \Delta m_{21}^2$): all the possible theoretical solutions are allowed at 1σ .

The damping in the QV region ($10^{-10} \text{ eV}^2 \leq \Delta m_{21}^2 \leq 10^{-7} \text{ eV}^2$) can be ascribable to several factors. However, the main sources of this phenomenon can be identified in:

1. the neutrino line width and energy resolution;
2. the averaging over the earth orbit.

The ${}^7\text{Be}$ neutrino energy smearing was deeply studied by J. Bahcall. In Ref. [82], the ${}^7\text{Be}$ line shape is found to be asymmetric: on the low-energy side, the line shape is Gaussian with a half-width at half-maximum of 0.6 keV and, on the high-energy side, the line shape is exponential with a half-width at half-maximum of 1.1 keV.

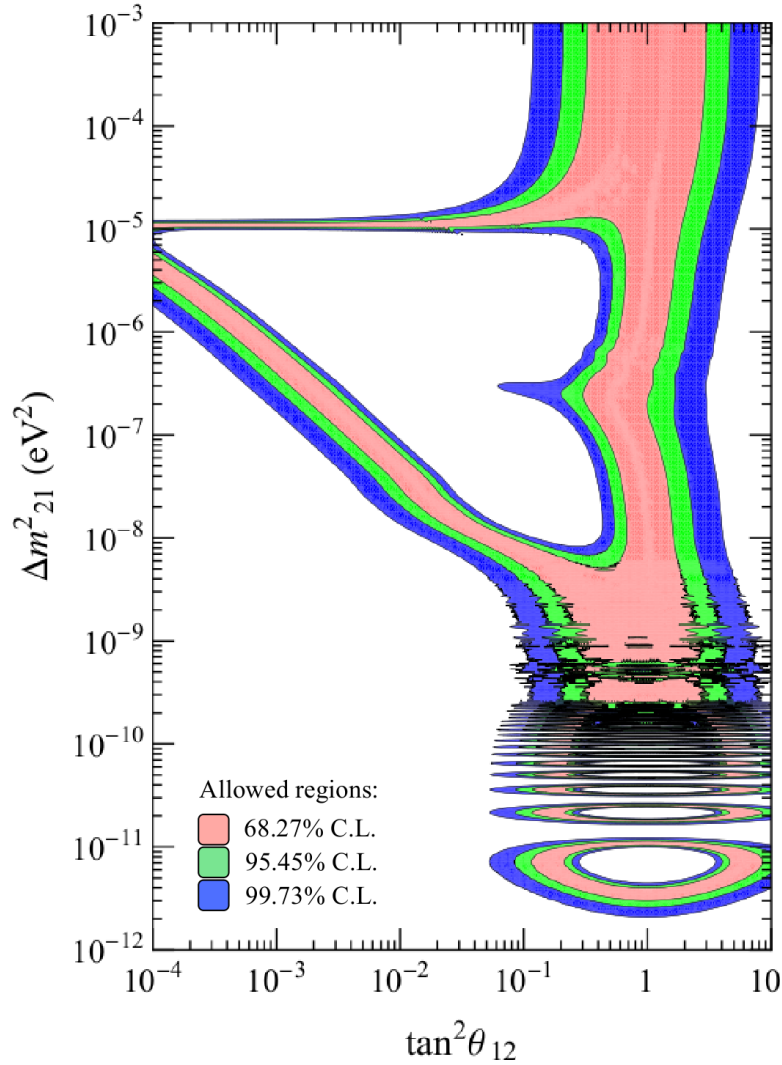


Figure 4.2: The Borexino ${}^7\text{Be}$ measurement impact in the $\tan^2\theta_{12} - \Delta m_{21}^2$ space, assuming $\theta_{13}=0$. Allowed regions ($d.o.f. = 2$) at 68.27% C.L. (pink), 95.45% C.L. (green) and 99.73% C.L. (blue).

4.2 The boron contribution

Even if its main goal was the detection of the ${}^7\text{Be}$ solar neutrinos, the Borexino experiment quickly revealed to be a powerful instrument, being able to measure not only the designed target but also other solar neutrino signals. In particular, in 2010, the Borexino collaboration released the measurement of the ν_e -e elastic scattering of ${}^8\text{B}$ solar neutrinos, with a 3 MeV electron energy threshold (see Sec. 2.8.3). The resulting counting rate was: $0.217 \pm 0.038(\text{stat}) \pm 0.008(\text{syst})$ cpd/100 ton, that is $0.217 \pm 17.9\%$ cpd/100 ton.

4.2 The boron contribution

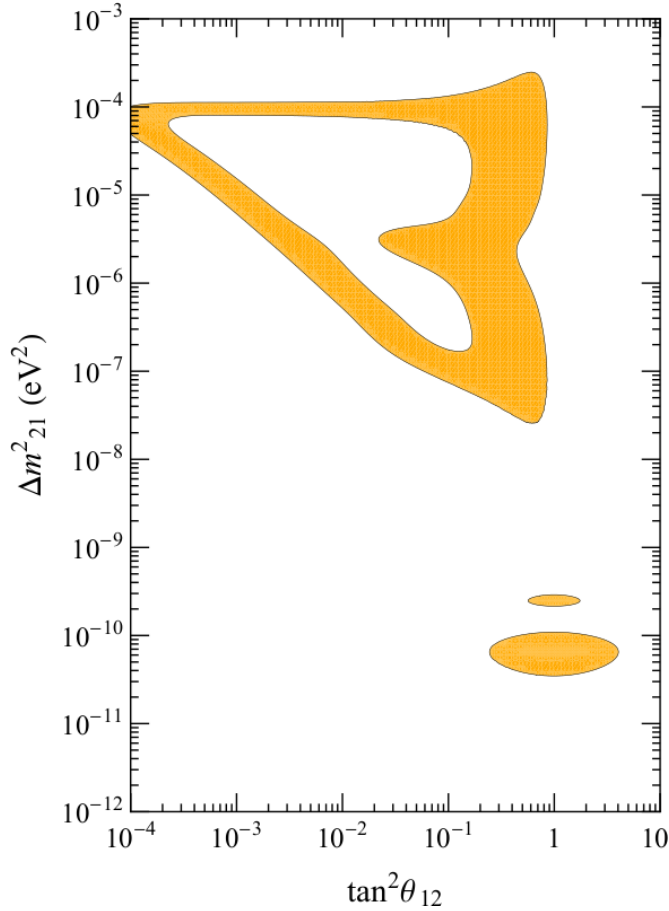


Figure 4.3: Iso-contours for the current Borexino ${}^8\text{B}$ neutrino flux result [4] at $\pm 1\sigma$ experimental error only. Electron energy threshold at 3 MeV.

The evaluation of the expected ${}^8\text{B}$ rate is similar to the one described in the previous section but, in addition, we take into account the theoretical spectral shape of ${}^8\text{B}$ neutrinos which dominates over all the other smearing sources.

In Fig. 4.3, the iso-contours of the minimum and maximum ${}^8\text{B}$ flux, allowed at 1σ (experimental error only) by the Borexino ${}^8\text{B}$ total rate ($E_{\text{thr}} = 3 \text{ MeV}$) measurement are indicated. As it was for the ${}^7\text{Be}$ case, the coloured region defines the fraction of the space of parameters that is authorized at 68.27% C.L. by this experimental rate only.

While going to the χ^2 analysis, it has to be considered that beryllium and boron neutrinos are strictly correlated. The two neutrinos in fact, derive from the same section of the solar pp chain (see Sec. 1.3.1); in particular, branch III (the ${}^8\text{B}$ branch) cannot exist if branch II (the ${}^7\text{Be}$ branch) has not happened first.

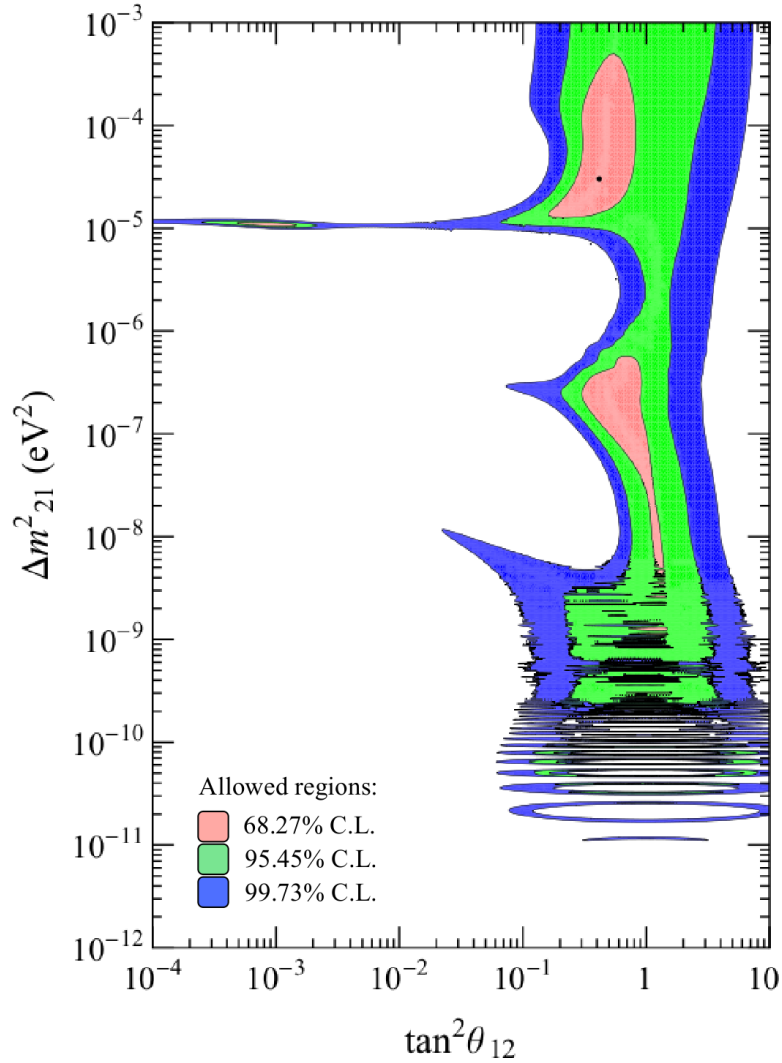


Figure 4.4: The Borexino ${}^7\text{Be}$ and ${}^8\text{B}$ (total flux above 3 MeV only) measurements impact in the $\tan^2\theta_{12} - \Delta m_{21}^2$ space. Allowed regions ($d.o.f. = 2$) at 68.27% C.L. (pink), 95.45% C.L. (green) and 99.73% C.L. (blue).

The theoretical correlation between ${}^7\text{Be}$ and ${}^8\text{B}$ fluxes was numerically computed in Ref. [57] as $\rho = 0.887$ for the high-metallicity hypothesis and $\rho = 0.878$ for the low-metallicity hypothesis. This effect is taken into account by evaluating a combined χ^2 of the berillium and boron rate. As explained in Sec. 3.4, the correlation between the two results is included at the level of the error matrix.

In Fig. 4.4, the fit of the ${}^7\text{Be}$ and ${}^8\text{B}$ neutrino fluxes is reported: all the possible oscillation solutions except the lowest Δm_{21}^2 Vacuum regime are still allowed at 1σ . At this level, the best fit for the oscillation parameters is found in the LMA region.

4.2 The boron contribution

4.2.1 The boron spectral shape contribution

The shape of the expected ${}^8\text{B}$ recoil energy spectrum is another information that can be extracted from the ${}^8\text{B}$ analysis. The experimental spectrum is indeed presented in Ref. [4] in terms of five energy bins: 3-5 MeV, 5-7 MeV, 7-9 MeV, 9-11 MeV, and 11-13 MeV.

For each energy interval, we evaluate the expected bin content. Due to the low statistics, the uncertainties are very large and the ${}^8\text{B}$ spectral shape alone cannot add any significant constraint to the oscillation solution.

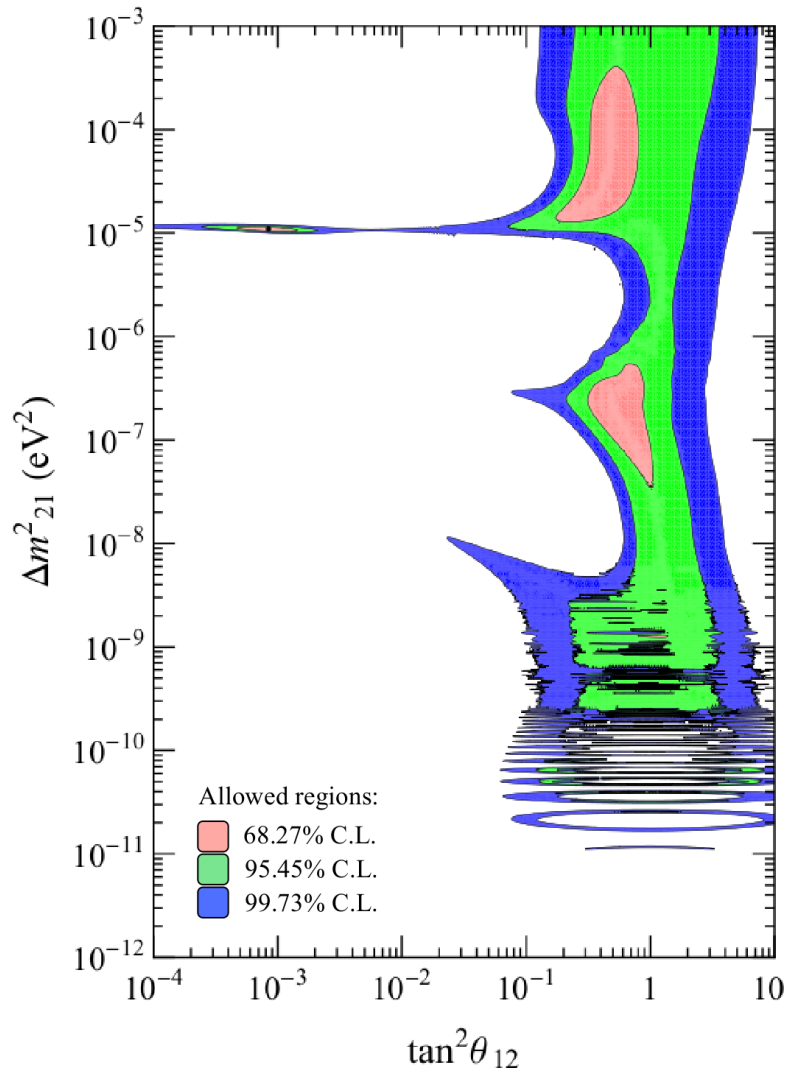


Figure 4.5: The Borexino ${}^7\text{Be}$ and ${}^8\text{B}$ (total rate above 3 MeV and spectral shape) measurements impact in the $\tan^2\theta_{12} - \Delta m^2_{21}$ space, assuming $\theta_{13}=0$. Allowed regions ($d.o.f. = 2$) at 68.27% C.L. (pink), 95.45% C.L. (green) and 99.73% C.L. (blue).

Anyhow, a separate χ^2 for the boron spectral shape is computed and then added to that of the previous beryllium-boron total rate analysis.

Figure 4.5 reports the status of the $n\text{-}\sigma$ allowed region after the inclusion of the ${}^8\text{B}$ spectral shape. The 1σ ($\Delta\chi^2 = 2.3$) region is depicted in pink, the 2σ ($\Delta\chi^2 = 6.18$) region in green and the 3σ ($\Delta\chi^2 = 11.83$) allowed region in blue.

In comparison with Fig. 4.4, the general shape of the allowed regions seems unchanged after the ${}^8\text{B}$ energy spectrum inclusion. Nevertheless, it can be noticed that the best fit of the oscillation parameters now belongs to the SMA solution. This fact should not surprise and it can be easily understood by looking at Fig. 4.6 where the χ^2 -profile of the Δm_{21}^2 parameter is reported. From this plot, as from Fig. 4.4 and 4.6, it is clear that either the LMA, the SMA, the LOW and the VAC solutions have similar χ^2 minima within about 1σ ($\Delta\chi^2 = 1$). Thus, the Δm_{21}^2 best fit value can easily flip from one solution to the other for small perturbations of the fit.

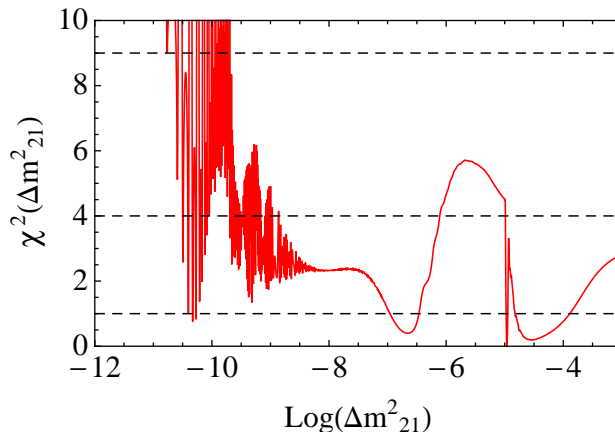


Figure 4.6: χ^2 -profile of the Δm_{21}^2 parameter in the Borexino ${}^7\text{Be}$ and ${}^8\text{B}$ (total rate and spectral shape) neutrino results analysis. The black dashed lines indicate the 1σ [$\chi^2(\Delta m_{21}^2) = 1$], 2σ [$\chi^2(\Delta m_{21}^2) = 4$] and 3σ [$\chi^2(\Delta m_{21}^2) = 9$] levels.

4.3 The Day-Night asymmetry contribution

As already discussed in Sec. 2.8.2, a generic feature of the matter-enhanced neutrino oscillations is the potential for the regeneration of the ν_e flavor eigenstate when solar neutrinos propagate through the earth, during the night. This feature may yield a non-zero day-night asymmetry (A_{DN}) in a region of the oscillation parameter space which depends on the energy spectrum of the detected solar neutrinos.

4.3 The Day-Night asymmetry contribution

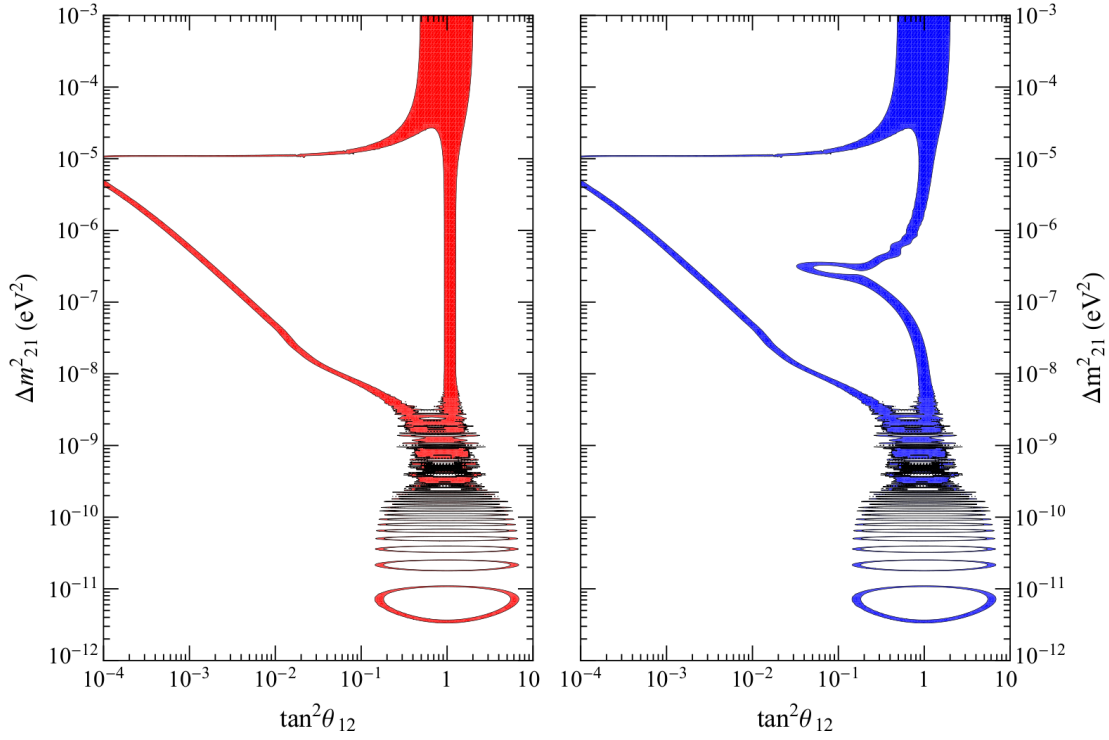


Figure 4.7: Iso-contours for the current Borexino ${}^7\text{Be}$ neutrino flux at $\pm 1\sigma$, experimental error only, during day (red, panel left) and night (blue, panel right).

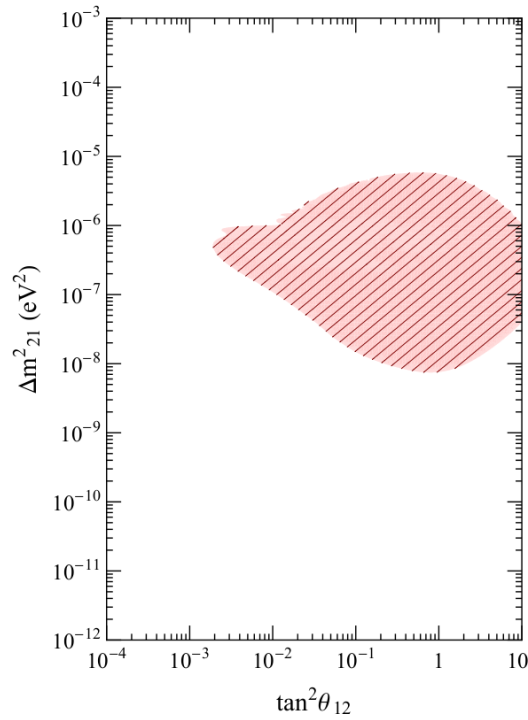


Figure 4.8: Iso-contours for the Day-Night asymmetry of the current Borexino ${}^7\text{Be}$ signal at $\pm 1\sigma$ experimental error only. The coloured-dashed region is the one excluded by the A_{DN} .

In particular, for Borexino A_{DN} should be ~ 0 in the LMA region, while it should be > 0 in the LOW region.

The Borexino collaboration have searched for a day-night asymmetry (Ref. [2]) in the interaction rate of 862 keV ${}^7\text{Be}$ solar neutrinos. The result is $A_{\text{DN}} = 0.001 \pm 0.012(\text{stat}) \pm 0.007(\text{syst})$, and it is consistent with zero and therefore with the prediction of the LMA-MSW neutrino oscillation scenario.

According to Ref. [2], we define day-night asymmetry the ratio:

$$A_{\text{DN}} = 2 \frac{N - D}{N + D} \quad (4.1)$$

where N and D are the rate expected during night and during day respectively. For each set of oscillation parameter Δm_{21}^2 , $\tan^2 \theta_{12}$ and $\sin^2 \theta_{13}$, we compute the expected value of A_{DN} and we compare, via χ^2 -fit, the latter result with the A_{DN} experimentally obtained by Borexino.

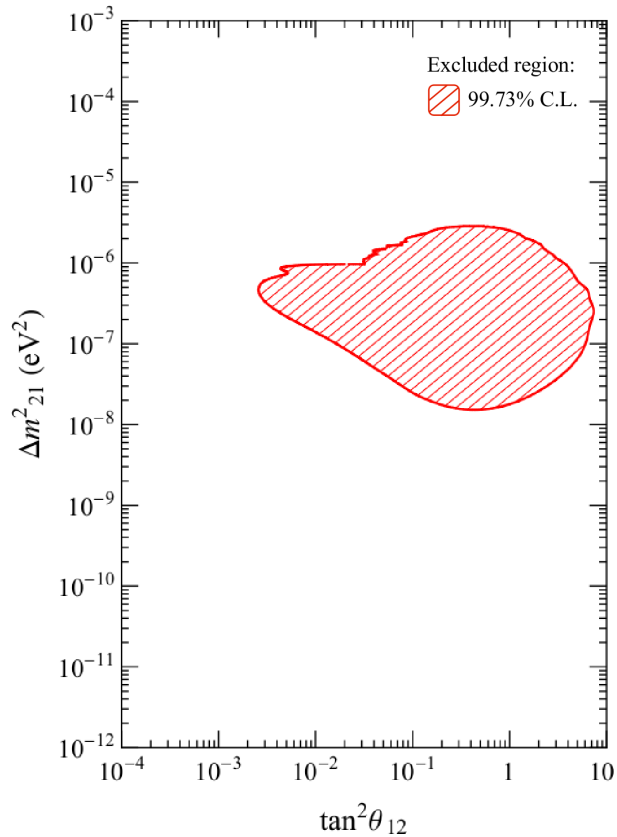


Figure 4.9: The Borexino day-night asymmetry impact in the $\tan^2 \theta_{12} - \Delta m_{21}^2$ space, assuming $\theta_{13}=0$. Excluded region at 99.73% C.L. ($d.o.f. = 2$).

4.3 The Day-Night asymmetry contribution

In Fig. 4.1 we already reported the iso-contours of the actual ${}^7\text{Be}$ Borexino result (Ref. [1]), averaged over a full day measurement. In Fig. 4.7 we report the iso-contours of the actual Borexino ${}^7\text{Be}$ result (Ref. [1]) at $\pm 1\sigma$ in the case of a day-only detection (red, left panel) and a night-only detection (blue, right panel). A clear difference can be seen in the LOW region of oscillation parameters, due to earth regeneration effects.

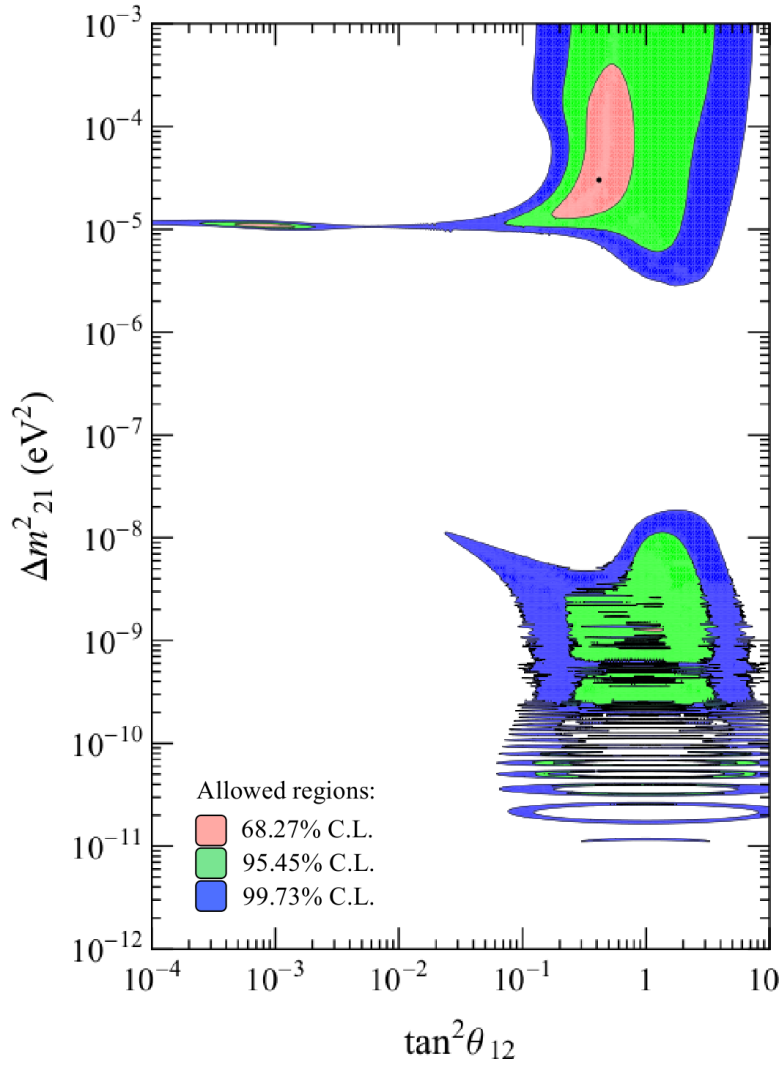


Figure 4.10: The Borexino day-night asymmetry, ${}^7\text{Be}$ and ${}^8\text{B}$ measurements impact in the $\tan^2 \theta_{12} - \Delta m_{21}^2$ space, assuming $\theta_{13}=0$. Allowed regions ($d.o.f. = 2$) at 68.27% C.L. (pink), 95.45% C.L. (green) and 99.73% C.L. (blue).

In Fig. 4.8 we report the iso-contours for the Borexino day-night asymmetry at $\pm 1\sigma$, considering the experimental error only. The preferred $\tan^2 \theta_{12} - \Delta m_{21}^2$ region is the complement to the coloured-dashed one. Taking into account not only the experimental error but also the theoretical one, we perform the χ^2 -analysis. In Fig. 4.9, we chose to represent the effect of the Borexino A_{DN} measurement in guise of excluded region of the oscillation parameters at 99.73% C.L. (dashed red).

The impact of this result in the Borexino only global analysis is really impressive: the A_{DN} measurement alone rules out the LOW oscillation parameter region at more than 8.5σ . This can be easily verified once we add the A_{DN} fit result to the χ^2 of the beryllium-boron analysis (^8B spectral shape included) described in Sec. 4.2.1.

In Fig. 4.10, the impact of the Borexino results so far examined is reported at 68.27% C.L. ($\Delta\chi^2 = 2.3$, pink), 95.45% C.L. ($\Delta\chi^2 = 6.18$, green) and 99.73% C.L. ($\Delta\chi^2 = 11.83$, blue).

After the A_{DN} inclusion, the LOW solution is no longer acceptable and the allowed (at 68.27% C.L.) oscillation solutions are now the SMA, the LMA, the QV and the VAC. At this stage, the best fit for the oscillation parameters lies in the LMA sector (see Fig. 4.11), although the SMA, QV and VAC χ^2 minima are very similar to the LMA one.

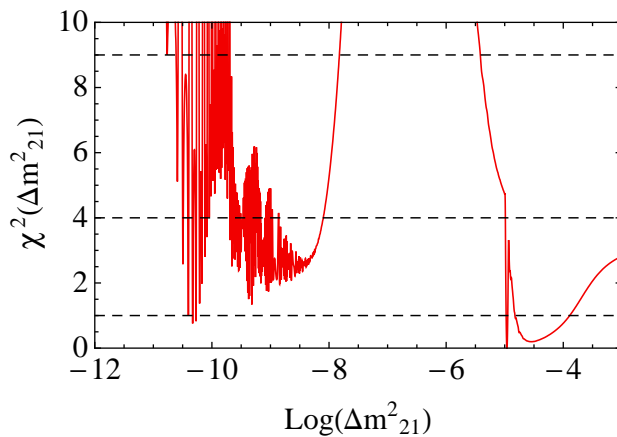


Figure 4.11: χ^2 -profile of the Δm_{21}^2 parameter in the Borexino ^7Be , A_{DN} and ^8B (total rate and spectral shape) neutrino results analysis. The black dashed lines indicate the 1σ [$\chi^2(\Delta m_{21}^2)=1$], 2σ [$\chi^2(\Delta m_{21}^2)=4$] and 3σ [$\chi^2(\Delta m_{21}^2)=9$] levels.

4.4 The pep contribution

In 2011, the Borexino collaboration has provided evidence (see Sec. 2.8.4) of the rare signal from pep neutrinos: this is the very first observation of solar neutrinos in the 1.0-1.5 MeV energy range. The best estimate for the pep neutrino interaction rate is: $3.1 \pm 0.6(\text{stat}) \pm 0.3(\text{syst})$ cpd/100 ton, that is $3.1 \pm 21.6\%$ cpd/100 ton.

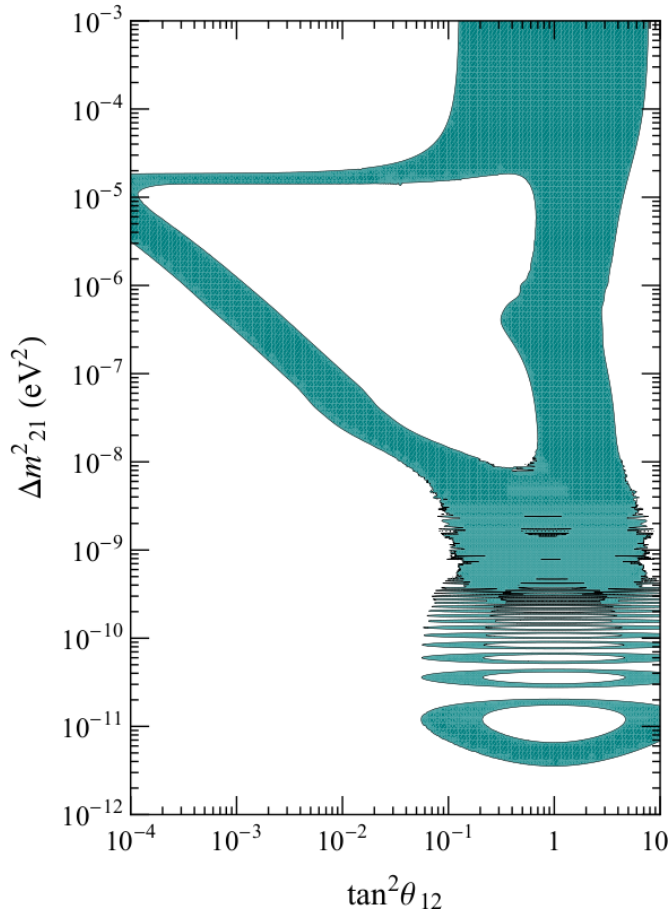


Figure 4.12: Iso-contours for the current Borexino pep neutrino flux result [3] at $\pm 1\sigma$ experimental error only.

In Fig. 4.12 the iso-contours of the minimum and maximum pep neutrino flux, allowed at 1σ by the Borexino pep interaction rate measurement are indicated. As in the previous cases, the coloured region defines the fraction of the space of parameters that is authorized at 68.27% C.L. by this experimental rate only.

As it was for the ${}^7\text{Be}$ expected rate computation, since the pep neutrinos are monochromatic, we have to deal with the smearing of oscillations in the QV region, due to the neutrino line width, energy resolution and to the averaging over the earth orbit.

For what concerns the pep neutrino energy smearing, a study by J. Pantaleone, reported in Ref. [83], found the half-width at half-maximum of the pep neutrino line to be 1.3 keV.

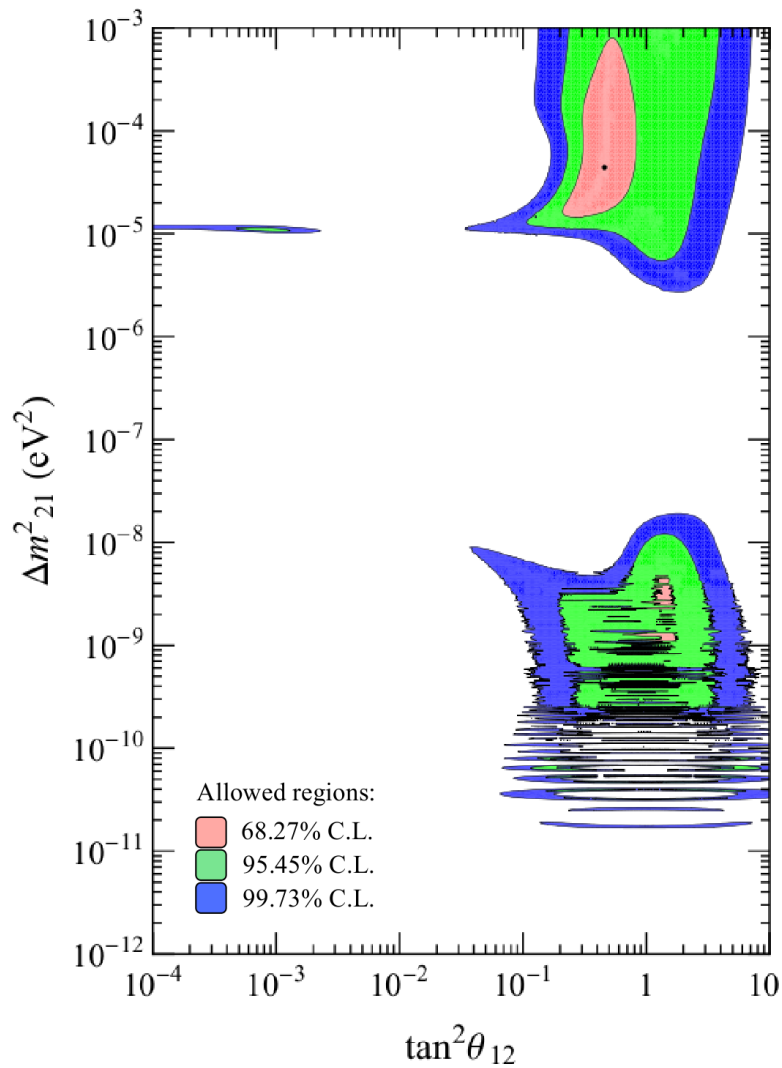


Figure 4.13: The Borexino final impact in the $\tan^2 \theta_{12} - \Delta m_{21}^2$ space, assuming $\theta_{13}=0$. Allowed regions ($d.o.f. = 2$) at 68.27% C.L. (pink), 95.45% C.L. (green) and 99.73% C.L. (blue).

4.5 Conclusions

The experimental error associated to the pep neutrino measurement is quite large ($> 20\%$) so we do not expect that it can strongly change the χ^2 analysis. However, the inclusion of the pep result has the merit of ruling out the thin 3σ region which connected the SMA to the LMA oscillation solution, and of reducing the significance of the SMA solution itself: see Fig. 4.11 and compare with 4.14.

4.5 Conclusions

In the previous sections, various Borexino results were separately introduced and analyzed. The plot presented in Fig. 4.13, represents the final result of the analysis of neutrino data coming from the Borexino experiment alone. After marginalizing over the different oscillation parameters, the best fit ($\pm 1\sigma$, $\Delta\chi^2 = 1$) results are:

$$\Delta m_{21}^2 = 4.4_{-2.6}^{+14.8} \times 10^{-5} \text{ eV}^2, \quad \tan^2 \theta_{12} = 0.46_{-0.18}^{+0.19}. \quad (4.2)$$

It is clear how the uniqueness of the Borexino experiment allows to explore, with only neutrino data, the whole space of parameters from the Just-So to the MSW regime, for θ_{12} belonging either to the first or to the second octant.

A clear output of this study is the rejection of the LOW solution in the MSW scenario: thanks to the day-night asymmetry measurement, the Borexino experiment is able to rule out the LOW mass regime at more than 8.5σ .

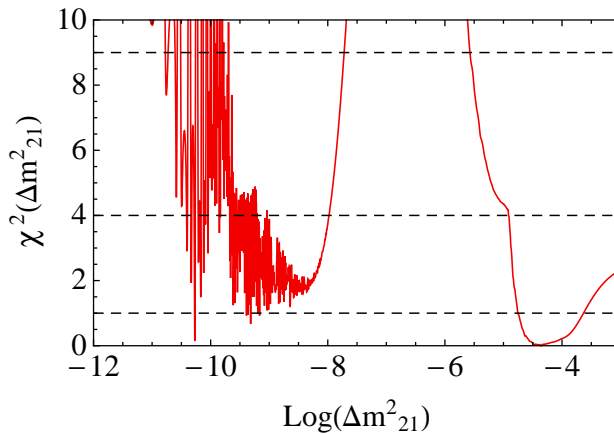


Figure 4.14: χ^2 -profile of the Δm_{21}^2 parameter in the Borexino results analysis. The black dashed lines indicate the 1σ [$\chi^2(\Delta m_{21}^2) = 1$], 2σ [$\chi^2(\Delta m_{21}^2) = 4$] and 3σ [$\chi^2(\Delta m_{21}^2) = 9$] levels.

The LMA-MSW region is clearly favoured but also the SMA, the QV and the VAC regions are allowed within 2σ (cf. Fig. 4.14).

We made the exercise of studying an improved ^8B result and we verified that a reduced experimental error ($\approx 10\%$) in the definition of the total flux and a consequent better definition of the spectral shape would yield the rejection of the SMA region at 99.73% C.L..

Borexino could also provide a measurement of the seasonal variations of the ^7Be solar neutrino signal (Sec. 2.6.1). At present, some studies on this topic are in progress and, as soon as possible, their results will be included in this Borexino alone analysis.

Finally, we would like to stress that even if all the plots reported in this chapter are produced assuming $\theta_{13}=0$, the whole analysis chain was performed for 4 different values of $\sin^2 \theta_{13}$ in the enlarged space of parameter (Δm_{21}^2 : $[10^{-12}, 10^{-3}]$; $\tan^2 \theta_{12}$: $[10^{-4}, 10]$) and for 26 different values in the MSW space of parameters (Δm_{21}^2 : $[10^{-8}, 10^{-3}]$; $\tan^2 \theta_{12}$: $[10^{-3}, 1]$). Both the grids cover the $0.000 \leq \sin^2 \theta_{13} \leq 0.049$ interval.

Being an experiment designed for solar neutrinos detection, Borexino is not strongly sensitive to the variations of the θ_{13} parameter: the results does not significantly change by assuming $\theta_{13}=0$ or $\theta_{13} \neq 0$. All the different outputs of the χ^2 -analysis are reported in Tab. A.1 of the Appendix.

Chapter 5

Global analysis of data from neutrino experiments

In this chapter we focus on the global analysis of data coming from the different types of neutrino experiments. The contributions of solar, reactors and accelerators experiments are presented and progressively included into the analysis.

Regarding solar neutrinos, we first analyze separately the impact of the results from the Homestake, GALLEX/GNO, SAGE, SNO and Super Kamiokande experiments, assuming the SHP11 standard solar model with high metallicity as discussed in Sec. 1.3.3. The analysis procedure is the same used for the Borexino only case and it is reported in Chap. 3. We then study the analysis of solar neutrino data without and with Borexino, and, after having independently analyzed the KamLAND results, we also perform a combined analysis of the solar plus KamLAND data. This combination is also used in the so-called *free-fluxes analysis* (Sec. 5.6) to derive constraints on some of the standard solar model parameters: the fluxes of ${}^7\text{Be}$, ${}^8\text{B}$, CNO and pp solar neutrinos.

In Tab. 5.1, the used experimental observables are summarized together with their reference papers, and the exact number of data (NoD) they introduce into the global analysis.

For what concerns contributions from atmospheric (SK I+II+III), reactor (CHOOZ experiment only), and accelerator experiments (MINOS + LBL), we remind (see Sec. 3.2) that we directly use the function $\chi^2_{\text{terrestrial}}(\theta_{13})$ resulting from the analysis performed by Gonzalez-Garcia, Maltoni and Salvado and reported in Ref. [78]. Hereafter, we refer to this latter contribution as the *terrestrial contribution*.

The analysis which includes the solar, KamLAND and terrestrial contributions is simply called *global analysis*.

Experiment	Observable	NoD ^a	Release	References
Homestake	Total Rate	1	1998	[25]
	Total Rate	1	2009	[30]
SAGE	Total Rate		2010	[29]
GALLEX/GNO	Total Rate	1	2011	[1]
			2011	[2]
BOREXINO	<i>pep</i> neutrino rate, ⁸ B total rate, ^b ⁸ B spectral shape	1	2011	[3]
		1	2010	[4]
		5		
SNO	P _{ee} and ⁸ B signal ADN	1	2009	[77]
		5	2010	[35]
Super Kamiookande	⁸ B observed event rate in phase I ⁸ B observed event rate in phase III	42	2006	[31]
		42	2011	[33]
KamLAND	P($\bar{\nu}_e \rightarrow \bar{\nu}_e$)	6	2011	[38]

^a For each experiment, NoD is the Number of Data we introduced into our global analysis.

^b ⁸B total rate above 3 MeV.

^c NC is Neutral Current.

Table 5.1: Summary of the solar and reactor experimental data used as input to the global analysis reported in this Ph.D. thesis.

We calculate the overall χ^2 by fitting all available neutrino data that is solar (101 entries) plus KamLAND (KL, 6 entries) plus terrestrial (80 entries) data. Therefore, our analysis counts a maximum of 187 entries and formally the analysis χ^2 can be written in the form (Ref. [66]):

$$\begin{aligned} \chi_{\text{global}}^2 = & \chi_{\text{solar}}^2(\Delta m_{21}^2, \tan^2 \theta_{12}, \sin^2 \theta_{13}, \{f_{\text{Be}}, f_{\text{B}}, f_{\text{CNO}}\}) + \\ & + \chi_{\text{KL}}^2(\Delta m_{21}^2, \tan^2 \theta_{12}, \sin^2 \theta_{13}) + \chi_{\text{terrestrial}}^2(\sin^2 \theta_{13}). \end{aligned} \quad (5.1)$$

Depending upon the case we consider, in χ_{solar}^2 analysis there can be as many as 6 free parameters, including Δm_{21}^2 , $\tan^2 \theta_{12}$, $\sin^2 \theta_{13}$ and the reduced fluxes f_{Be} , f_{B} , f_{CNO} (see Sec. 5.6).

Being aware of the strong KamLAND Δm_{21}^2 constraint, we decided to exclude the so-called Vacuum region and to focus instead on all the MSW oscillation scenarios. At this stage, we reduce the investigated range of parameters and let Δm_{21}^2 , $\tan^2 \theta_{12}$ and $\sin^2 \theta_{13}$ free to vary between:

$$10^{-8} \leq \Delta m_{21}^2 \text{ (eV}^2\text{)} \leq 10^{-3}, \quad 10^{-3} \leq \tan^2 \theta_{12} \leq 1 \quad \text{and} \quad 0.000 \leq \sin^2 \theta_{13} \leq 0.049.$$

The θ_{13} analysis of the KamLAND data and of the solar, solar plus KamLAND, terrestrial contribution and overall data-sets are reported at the end of each respective paragraph.

Since single solar experiments do not have significant sensitivity¹ to θ_{13} , for what concerns the radiochemical, SNO and Super Kamiokande experiments we directly report the result and the plot obtained by assuming the limit case $\theta_{13} = 0$ only. Anyway, the analysis has been performed for 26 different values of θ_{13} and a complete list of the results can be found in Tab. A.2, A.3, and Tab. A.4 of the Appendix.

5.1 Analysis of solar neutrino data

In the last years, the real-time solar neutrino experiments have appreciably improved their analysis techniques and, moreover, there has been a consistent gain in statistics. This yields better defined results and, consequently, a better definition of the allowed regions of the space of parameters. Here we quickly analyze the impact of the radiochemical, the SNO and the Super Kamiokande experiments in enhancing or disfavoring any of the MSW oscillation regimes.

¹The χ^2 -projection over θ_{13} are not statistically significant: all the θ_{13} values we analyze are allowed within 1σ .

5.1 Analysis of solar neutrino data

The combination of the solar neutrino experimental results other than Borexino (the solar-without-Borexino data set) is then accomplished with a three-flavor neutrino oscillation analysis by constructing a joint χ^2 -fit.

The outcome of the Borexino only analysis (Chap. 4) is finally added to the intermediate solar χ^2 (solar-with-Borexino data set) and, after marginalizing over $\sin^2\theta_{13}$, we obtain the allowed $\tan^2\theta_{12} - \Delta m_{21}^2$ region by solar global analysis and the corresponding best fit values for the oscillation parameters.

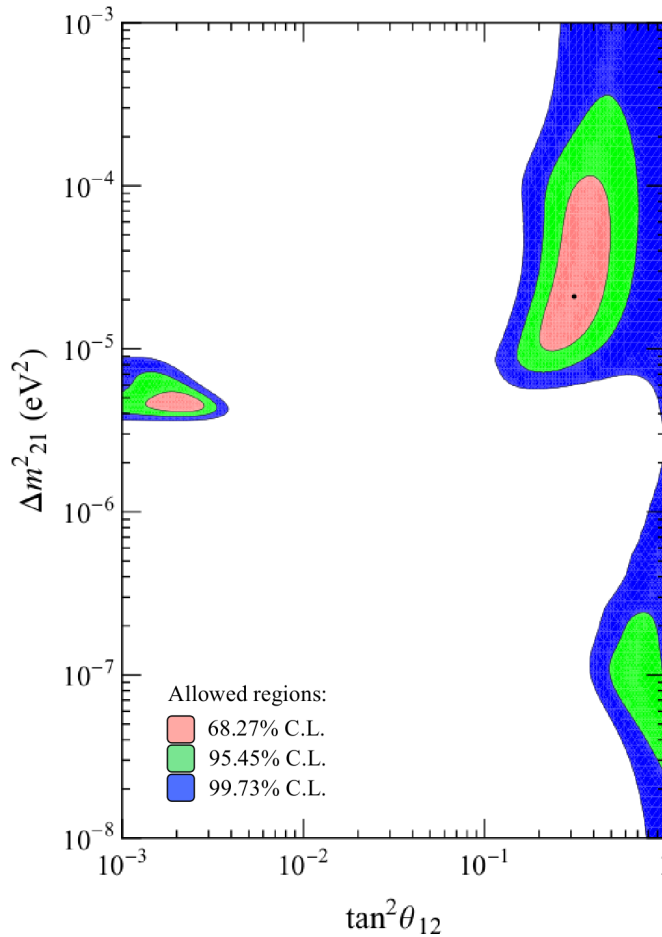


Figure 5.1: The joint Homestake, GALLEX/GNO and SAGE analysis in the $\tan^2\theta_{12} - \Delta m_{21}^2$ space, assuming $\theta_{13}=0$. Allowed regions ($d.o.f. = 2$) at 68.27% C.L. (pink), 95.45% C.L. (green) and 99.73% C.L. (blue).

5.1.1 Analysis of radiochemical data

After the completion of the gallium solar neutrino experiments (GALLEX: 1991-1997; GNO: 1998-2003; SAGE: 1990-2007), the availability of new technical information (i.e. the calibration of the GALLEX counters in the frame of the GNO experiment) permitted to improve the precision of the results (Ref. [29, 30]).

In order to perform a χ^2 -fit, once the survival probabilities P^S and P^E (Sec. 3.1) are computed, we first have to evaluate the expected rate on earth for each of the 8 solar neutrino sources, taking into account the different experimental energy thresholds. We remind that at this step, we assume the high metallicity hypothesis of the SHP11 standard solar model (Tab. 1.2).

The employed procedure is analogous to that used in the Borexino ${}^7\text{Be}$ case (Sec. 4.1): we computed the expected rates considering the several factors related to the energy of the various neutrino emissions (cross sections, energy resolutions, spectral shape...). By comparing the theoretical expectations with the experimental results, together with the theoretical and experimental errors, we obtain the χ^2 -analysis reported in Fig. 5.1. Once again, the allowed regions at 68,27% C.L., 95.45% C.L. and 99.73% C.L., are depicted in pink, green and blue color respectively.

The global analysis of the radiochemical results does not exclude any of the MSW oscillation solutions: LMA, LOW and SMA are allowed at least at 2σ . In particular, the SMA and the LMA oscillation solutions are allowed at 1σ and the best fit ($\pm 1\sigma$, $\Delta\chi^2 = 1$) of this branch of the solar analysis lies in the LMA sector:

$$\Delta m_{21}^2 = 2.1_{-0.9}^{+5.0} \times 10^{-5} \text{ eV}^2, \quad \tan^2 \theta_{12} = 0.31_{-0.08}^{+0.11}.$$

The radiochemical experiments alone do not prefer any particular θ_{13} value: the projection of the χ^2 over the $\sin^2 \theta_{13}$ parameter is not significant and therefore we do not report any upper limit for $\sin^2 \theta_{13}$.

5.1.2 Analysis of SNO data

In order to study the SNO impact in the selection of the oscillation parameters space, we chose to follow the same procedure adopted by the SNO collaboration in Ref. [35]. We analyze the data from the three phases of SNO by including the results on the low energy threshold analysis of phase I and phase II (SNO-LETA, Ref. [35]), in combination with the rates from phase III (Ref. [77]).

In Ref. [35], the SNO collaboration performs a fit in which the neutrino signal is described by six parameters: the $\phi({}^8\text{B})$ total neutrino flux; the coefficients c_0 , c_1 , c_2 through which they extract a quadratic expansion of the daytime P_{ee} as a function

5.1 Analysis of solar neutrino data

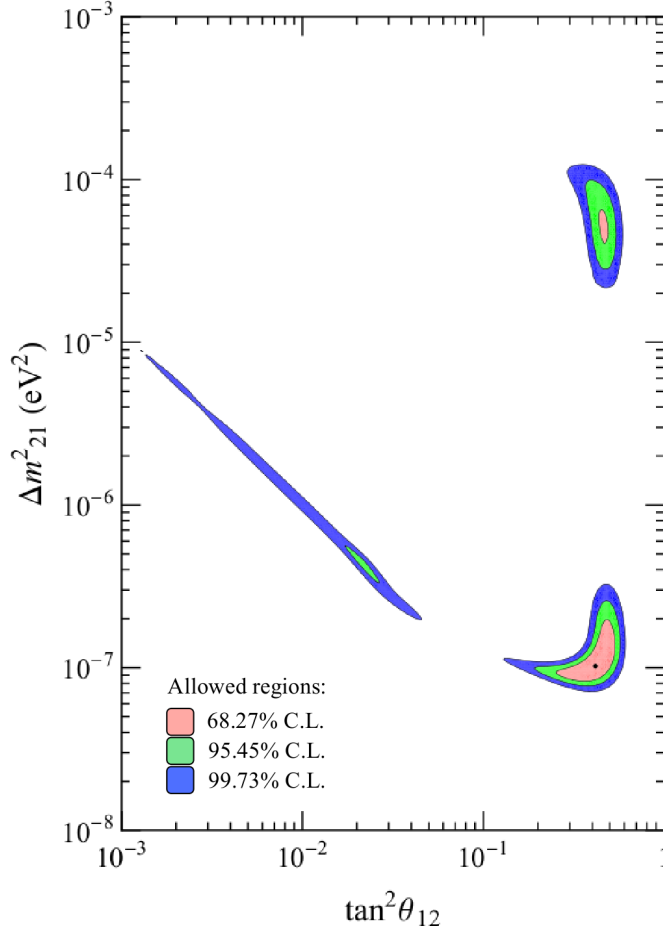


Figure 5.2: The analysis of SNO data in the $\tan^2 \theta_{12} - \Delta m_{21}^2$ space, assuming $\theta_{13}=0$. Allowed regions ($d.o.f. = 2$) at 68.27% C.L. (pink), 95.45% C.L. (green) and 99.73% C.L. (blue).

of E , around $E_\nu = 10$ MeV; the coefficients a_0 , a_1 which define a linear expansion of the day-night asymmetry around $E_\nu = 10$ MeV. Thanks to this parametrization, it is possible to reduce correlations between c_0 (the constant term of the quadratic P_{ee}) and the higher order terms by expanding all functions around the detected ${}^8\text{B}$ spectrum peak near 10 MeV.

For what concerns the SNO-LETA (Ref. [35]), we evaluate the theoretical expectations for the coefficients of the polynomial survival probability and day/night asymme-

try. In order to do this, it is necessary to take into account the sensitivity of the SNO detector (i.e. the energy dependence of the cross sections and the reaction thresholds) so that the parameterization of the model prediction at each point in the MSW plane samples the neutrino energy spectrum in the same manner and over the same range as the data.

For each set of Δm_{21}^2 , $\tan^2 \theta_{12}$ and $\sin^2 \theta_{13}$ parameters, we then calculate the χ^2 value by comparing the predicted polynomial parameters (c_0 , c_1 , c_2 , a_0 , and a_1) to the actual SNO results, taking into account all uncertainties and correlations declared by the SNO collaboration. The SNO rates from phase III are treated as a separate data-set, with the same approach used for the radiochemical experiments.

If we perform the global analysis over these data, we can observe (Fig. 5.2) that the SNO experiment alone rules out the SMA solution while both the LMA and the LOW solutions are allowed at 1σ . The best fit ($\pm 1\sigma$, $\Delta\chi^2 = 1$) belongs to the LOW solution² and we find:

$$\Delta m_{21}^2 = 1.02_{-0.13}^{+0.38} \times 10^{-7} \text{ eV}^2, \quad \tan^2 \theta_{12} = 0.417_{-0.091}^{+0.075}.$$

As it was in the radiochemical and Borexino case, the SNO experiment alone does not prefer any particular θ_{13} value and the χ^2 -projection over $\sin^2 \theta_{13}$ is not really significant.

5.1.3 Analysis of Super Kamiokande data

In our global analysis we also include the solar neutrino measurement carried out by the Super Kamiokande experiment. In particular, we analyze the data coming from SK phase I and phase III.

Since Super Kamiokande is able to measure ^8B and hep neutrinos, we adapt the procedure we used in computing the Borexino boron expectation and we calculate the total rate foreseen by the SHP11 standard solar model neutrino fluxes prediction. The whole analysis chain starts with the survival probabilities computation (P^S and P^E at Kamioka latitude) and continues with the ^8B and hep total rates evaluation, taking into account the respective cross sections, energy resolutions and spectral shapes.

Finally, by comparing the theoretical expectations with the experimental results, together with the theoretical and experimental errors (both statistics and systematics), we obtain the χ^2 -analysis we report in Fig. 5.3.

²In September 2011, during the 12th International Conference on Topics in Astroparticle and Underground Physics (TAUP 2011), the SNO collaboration released (Ref. [37]) a combined analysis of all three phases of solar neutrino data with the SNO detector. From this analysis, it results that the LMA region is slightly favoured, even if SNO data alone cannot distinguish between the LMA and the LOW regions. We performed a quick analysis and we verified that the replacement of the old SNO results with their newest does not modify any of our global analysis conclusions.

5.1 Analysis of solar neutrino data

As it was in the SNO case, Super Kamiokande alone disfavours the SMA region while allows, at least at 2σ , the LMA and LOW solutions. The best fit definitely belongs to the LMA solution and we find:

$$\Delta m_{21}^2 = 5.1_{-1.1}^{+3.0} \times 10^{-5} \text{ eV}^2, \quad \tan^2 \theta_{12} = 0.556_{-0.061}^{+0.071}.$$

Also Super Kamiokande is not sensitive to θ_{13} variation and its $\chi^2(\sin^2 \theta_{13})$ profile is not very significant.

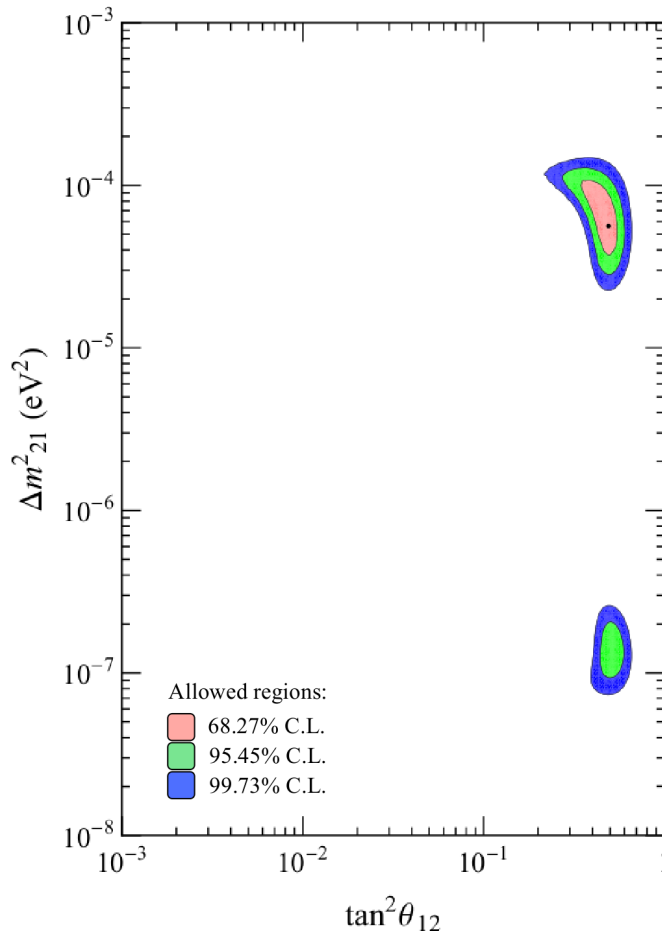


Figure 5.3: The analysis of SK data only in the $\tan^2 \theta_{12} - \Delta m_{21}^2$ space, assuming $\theta_{13}=0$. Allowed regions ($d.o.f. = 2$) at 68.27% C.L. (pink), 95.45% C.L. (green) and 99.73% C.L. (blue).

We want to emphasize that our analysis is in good agreement with the result obtained by the Super Kamiokande collaboration and reported in Ref. [33], where it is shown that the energy spectrum and the time variation of the solar neutrino flux measured by SK favor only the LMA solution at 95% C.L.; it must be said though that this result is achieved by constraining the ^8B neutrino flux to the SNO NC flux and the hep neutrino flux to the standard solar model prediction. The plot in Fig. 5.3 does not include any supplementary constraint and, for this reason, shows allowed region in the LOW regime at 95.45% C.L..

5.1.4 Analysis of all solar neutrino data

After having analyzed the single experiments, we can finally proceed with the actual solar global analysis.

At this stage of the analysis, χ^2_{solar} is a function of the three oscillation parameters only: Δm_{21}^2 , $\tan^2 \theta_{12}$ and $\sin^2 \theta_{13}$. With the same previous strategies, we combine the results obtained for each experiment, and we build a joint χ^2 -fit through which we are able to perform a three-flavor oscillation analysis. The $\tan^2 \theta_{12} - \Delta m_{21}^2$ allowed regions are therefore obtained after marginalization of the χ^2_{solar} with respect to the undisplayed parameter $\sin^2 \theta_{13}$.

In Fig. 5.4, we show the $\tan^2 \theta_{12} - \Delta m_{21}^2$ space of parameters as defined by all the solar experiment without Borexino. The best fit for the oscillation parameters belong to the LMA-MSW region and they are:

$$\Delta m_{21}^2 = 5.4_{-1.1}^{+1.7} \times 10^{-5} \text{ eV}^2, \quad \tan^2 \theta_{12} = 0.479_{-0.042}^{+0.035}, \quad \text{and} \quad \sin^2 \theta_{13} = 0.011_{-0.029}^{+0.029},$$

with a minimum $\chi^2_{solar}/\text{ndf}$ ratio of 94.2/89. For the sake of illustration, we extrapolated the lower 1σ bound to the unphysical region $\sin^2 \theta_{13} < 0$; details on the fit results can be found in Tab. A.6 of the Appendix.

From Fig. 5.4 it can be noticed that the solar-without-Borexino data exclude at more than 3σ the SMA-MSW regime while a small portion of the LOW solution is still allowed at 99.73% C.L..

We define the actual χ^2_{solar} as the combination of this latter result with the outcome of the Borexino only global analysis. By combining these two contributions, we obtain an analysis that takes into account the experimental errors (the systematic and statistical errors summed in quadrature) and the theoretical errors in the total count rates, including the correlation of the ^7Be and ^8B theoretical fluxes. It also includes the bin-to-bin correlations in the uncertainties in the predicted ^8B neutrino recoil spectrum resulting from the uncertainties in the predicted neutrino spectrum, and from energy

5.1 Analysis of solar neutrino data

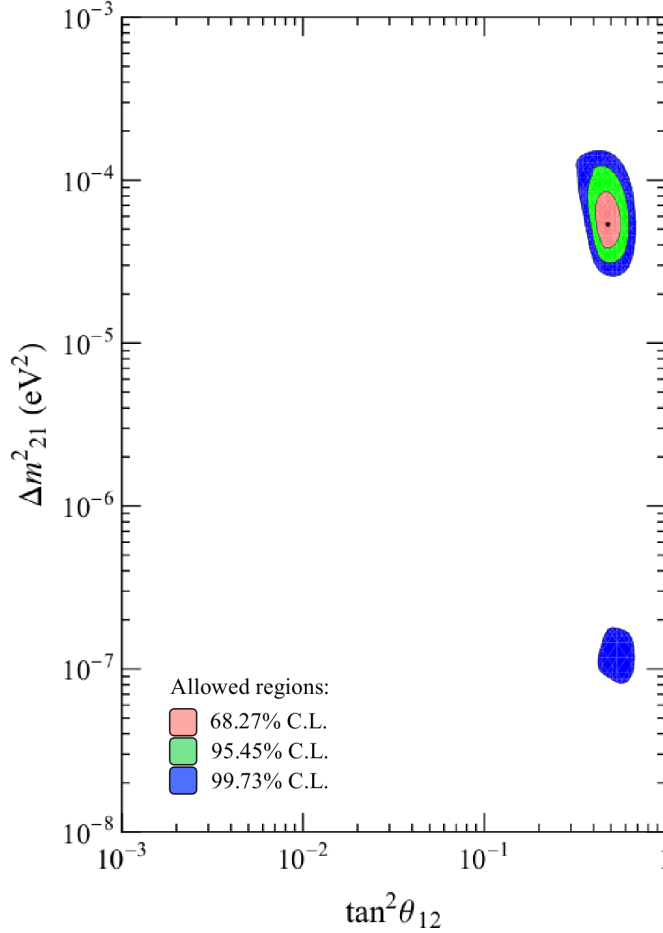


Figure 5.4: The global analysis of the solar neutrino data without the Borexino contribution, in the $\tan^2 \theta_{12} - \Delta m_{21}^2$ space, after marginalization over $\sin^2 \theta_{13}$. Allowed regions ($d.o.f. = 3$) at 68.27% C.L. (pink), 95.45% C.L. (green) and 99.73% C.L. (blue).

threshold uncertainties and energy resolution in the experiments.

In Fig. 5.5, we show the $n\text{-}\sigma$ allowed regions, in the same convention as before.

The LMA region is only slightly modified and the new best fit point is:

$$\Delta m_{21}^2 = 5.4_{-1.1}^{+1.7} \times 10^{-5} \text{ eV}^2, \quad \tan^2 \theta_{12} = 0.468_{-0.044}^{+0.031}, \quad \text{and} \quad \sin^2 \theta_{13} = 0.011_{-0.030}^{+0.030}.$$

with a minimum χ^2_{solar}/ndf ratio of 94.6/98. For the sake of illustration, we extrapolated the lower 1σ bound to the unphysical region $\sin^2 \theta_{13} < 0$.

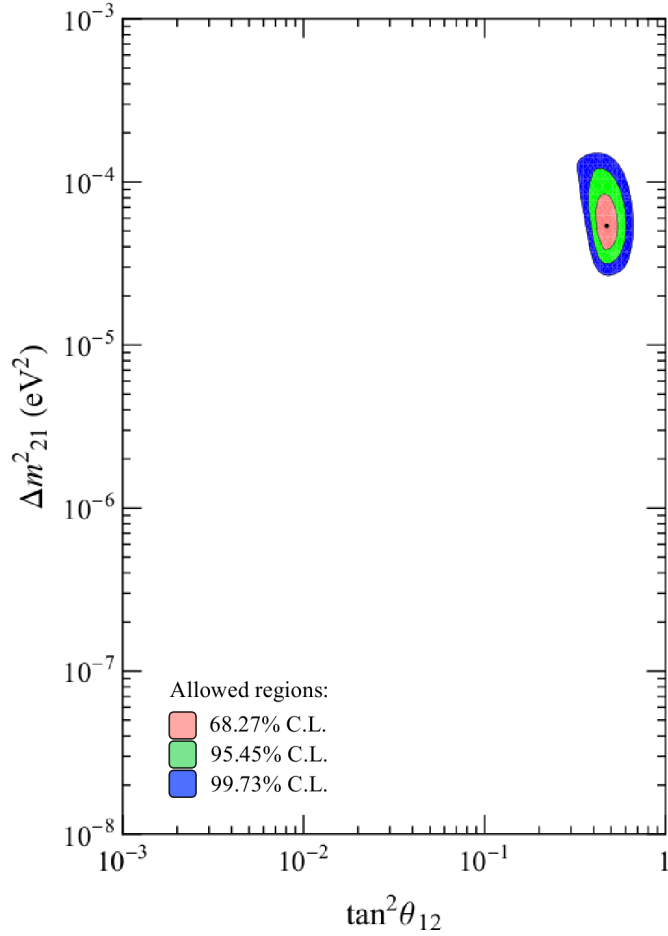


Figure 5.5: The global analysis of all the available solar data, in the $\tan^2 \theta_{12} - \Delta m_{21}^2$ space, after marginalization over $\sin^2 \theta_{13}$. Allowed regions ($d.o.f. = 3$) at 68.27% C.L. (pink), 95.45% C.L. (green) and 99.73% C.L. (blue).

An essential difference is that now the LOW region is strongly excluded at $\Delta\chi^2 \gg 190$. Therefore, after the inclusion of the Borexino day-night data, solar neutrino data alone can single out the LMA solution with very high confidence (see Fig. 5.6), without the inclusion of anti-neutrino data that is without relying on CPT symmetry.

The origin of this powerful result is mainly due to the precise Borexino day-night asymmetry measurement (Ref. [2]). In fact, the measured asymmetry alone, in agreement with the prediction of MSW-LMA neutrino oscillations, disfavours at more than 8.5σ MSW oscillations with mixing parameters in the LOW region.

Finally, it is worth to notice that even if single solar neutrino experiments do not have significant sensitivity to $\sin^2 \theta_{13}$ variation, this is not the case of the combination

5.1 Analysis of solar neutrino data

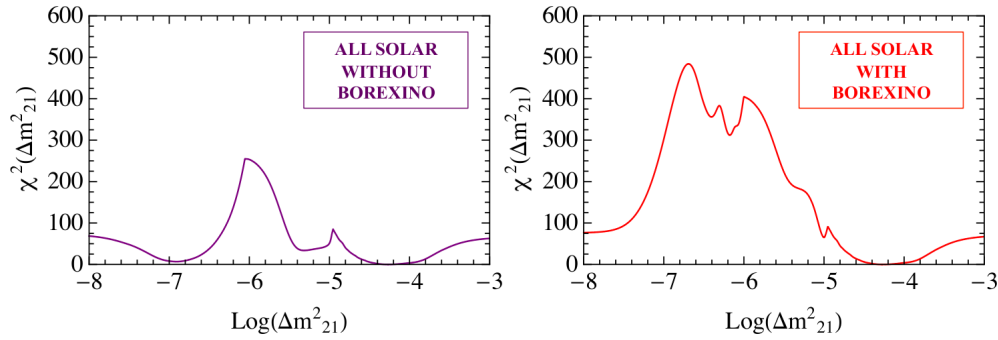


Figure 5.6: Comparison of the χ^2 -profile for Δm_{21}^2 , obtained by the global analysis of all available solar data without and with the Borexino contribution, marginalized over $\tan^2 \theta_{12}$ and $\sin^2 \theta_{13}$.

of all solar neutrino experiments together (Fig. 5.7). In fact, for increasing values of θ_{13} a slight tension arises among different data-sets and, in particular, between the SNO and radiochemical data. These two experiments, probing respectively the high and low energy part of the solar neutrino spectrum, exhibit different correlation properties between the two mixing parameters θ_{12} and θ_{13} : for increasing values of θ_{13} , the SNO and gallium experiments tend to prefer higher and lower values of $\tan^2 \theta_{12}$, respectively, worsening the good agreement currently reached at $\theta_{13} \simeq 0$. Therefore, a "collective" effect of different experiments is responsible for the solar neutrino constraints on $\sin^2 \theta_{13}$ (Ref. [84]).

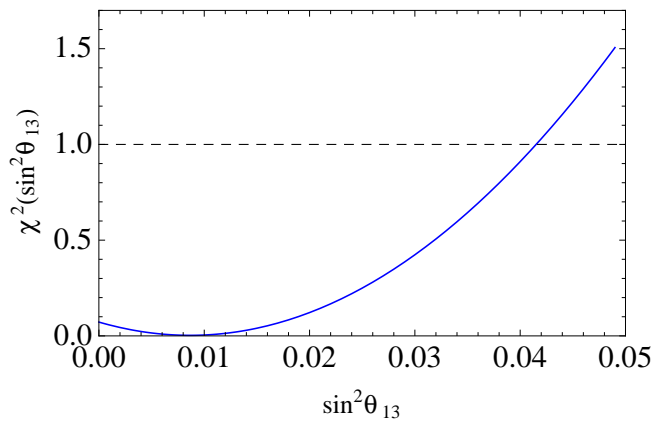


Figure 5.7: χ^2 -profile for $\sin^2 \theta_{13}$, obtained by the global analysis of all available solar data. The dashed line indicates the 1σ [$\chi^2(\sin^2 \theta_{13}) = 1$] level.

5.2 Analysis of KamLAND anti-neutrino data

The KamLAND experiment mainly analyzes the anti-neutrinos from reactors. In studying the KamLAND impact in the neutrino oscillation scenario, we follow the procedure adopted by the KamLAND collaboration in Ref. [38]. We analyze the data-set which includes data acquired following a radiopurity upgrade, and amounts to a total exposure of 3.49×10^{32} target-proton-year. In order to compare KamLAND results with those we have seen so far, we assume the CPT invariance.

Reference [38] reports a parametric expression of the survival probability as well as the observed values, with the relative uncertainties (statistical and background estimates only, uncorrelated). Hence, we can directly perform the χ^2 -fit.

Figure 5.9 shows the n - σ allowed regions by the KamLAND results only: assuming CPT invariance, the LMA results is singled out at more than 99.73% C.L.. Figure 5.8 shows the $\chi^2(\sin^2 \theta_{13})$ profile of the global analysis of KamLAND only data. It can be noticed that even if there is a well-defined minimum in $\sin^2 \theta_{13} = 0.029$, the $\sin^2 \theta_{13} = 0$ value is within the 1σ acceptance window. The best fit obtained after marginalizing

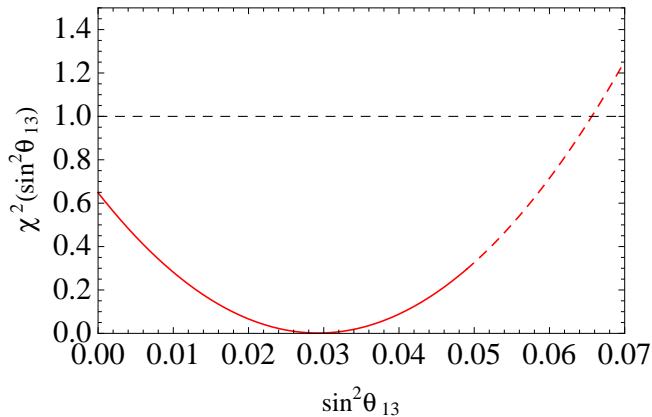


Figure 5.8: χ^2 -profile for $\sin^2 \theta_{13}$, obtained by the global analysis of KamLAND data. The red solid part is the actual result of our analysis while the red dashed line is an analytic extrapolation. The black dashed line indicates the 1σ [$\chi^2(\sin^2 \theta_{13}) = 1$] level.

over the three oscillation parameters is:

$$\Delta m_{21}^2 = 7.50_{-0.20}^{+0.19} \times 10^{-5} \text{ eV}^2, \quad \tan^2 \theta_{12} = 0.437_{-0.060}^{+0.073}, \quad \text{and} \quad \sin^2 \theta_{13} = 0.029_{-0.034}^{+0.034},$$

with a minimum χ_{KL}^2/ndf ratio of 1.8/3. Again, for the sake of illustration, we extrapolated the lower 1σ bound to the unphysical region $\sin^2 \theta_{13} < 0$.

5.2 Analysis of KamLAND anti-neutrino data

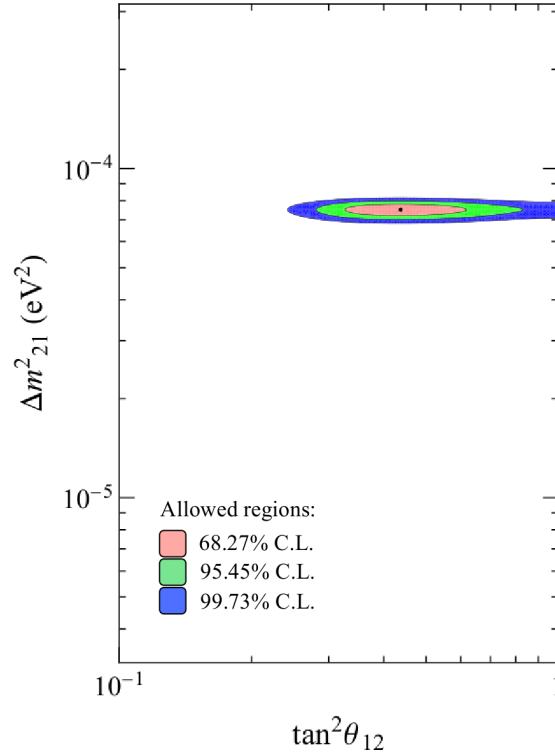


Figure 5.9: The analysis of KamLAND reactor data, in the $\tan^2 \theta_{12} - \Delta m_{21}^2$ space, after marginalization over $\sin^2 \theta_{13}$. Allowed regions ($d.o.f. = 3$) at 68.27% C.L. (pink), 95.45% C.L. (green) and 99.73% C.L. (blue).

It is also interesting to compare the behaviour of solar experiments and KamLAND in the $\tan^2 \theta_{12} - \Delta m_{21}^2$ space of parameters, for different $\sin^2 \theta_{13}$ values. It is well known that solar data are mostly sensitive to the precise value of CC/NC event as determined by Super Kamiokande and SNO and provide a strong constraint on the $\tan^2 \theta_{12}$ parameter; on the other hand, KamLAND defines Δm_{21}^2 to be in the LMA range. Looking at the plots in Fig. 5.10, we can see that while the results show a constant agreement in Δm_{21}^2 , there appears to be a mismatch in the favored value of $\tan^2 \theta_{12}$ as determined from KamLAND compared to the one from solar neutrinos.

As it was pointed out in Ref. [85, 79] and widely discussed in the literature, this tension can be accommodated by a non-zero value of θ_{13} . This happens because the solar component can be fitted with a higher value of $\tan^2 \theta_{12}$ provided that a non-zero θ_{13} is included and, conversely, the KamLAND spectrum can be well fitted with a smaller value of $\tan^2 \theta_{12}$; therefore the best fit values for solar and KamLAND analysis agree

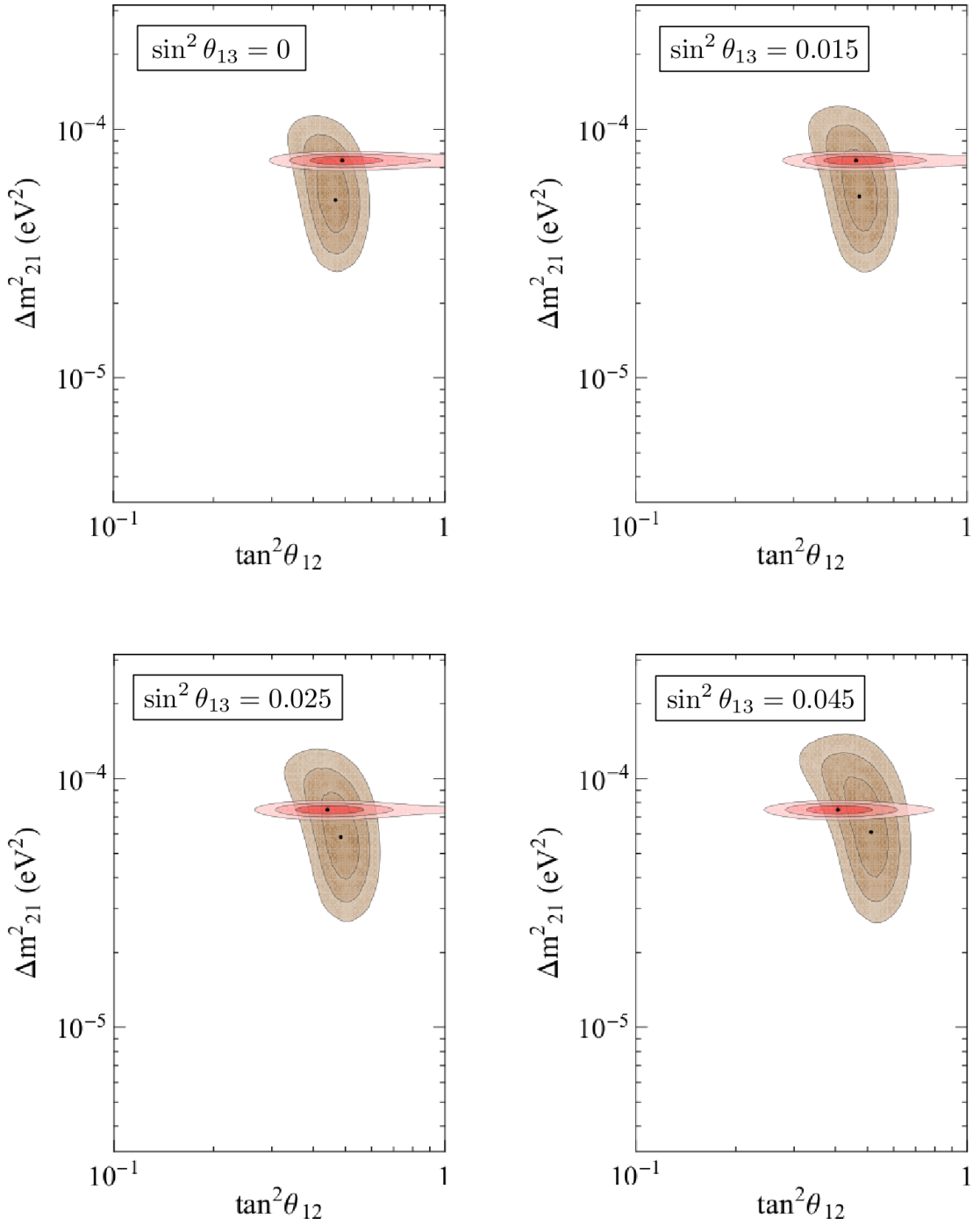


Figure 5.10: The analysis of solar (brown scale) vs KamLAND reactor (red scale) data, in the $\tan^2 \theta_{12} - \Delta m^2_{21}$ space, assuming $\sin^2 \theta_{13} = 0$ (top, left), $\sin^2 \theta_{13} = 0.015$ (top, right), $\sin^2 \theta_{13} = 0.025$ (bottom, left) and $\sin^2 \theta_{13} = 0.045$ (bottom, right). Allowed regions ($d.o.f. = 2$) at 68.27% C.L., 95.45% C.L. and 99.73% C.L. are pictured in growing lighter scale.

5.3 Joint analysis of solar and KamLAND data

better for $\theta_{13} \neq 0$. This behavior, the famous hint of $\theta_{13} > 0$, is clearly visible in the the four panels of Fig. 5.10 where the global analysis of the solar data (brown scale) and the KamLAND reactor data (red scale) are plotted at different $\sin^2 \theta_{13}$ values: $\sin^2 \theta_{13} = 0$ (top, left), $\sin^2 \theta_{13} = 0.015$ (top, right), $\sin^2 \theta_{13} = 0.025$ (bottom, left) and $\sin^2 \theta_{13} = 0.045$ (bottom, right). Allowed regions at 68.27% C.L., 95.45% C.L. and 99.73% C.L. are pictured in growing lighter scale.

5.3 Joint analysis of solar and KamLAND data

After having analyzed both the KamLAND and the single solar experiments, the next logical step is the combined analysis of the solar plus KamLAND data-set.

We accomplish this study by directly summing (there are no correlations between the solar and KamLAND sets of data) the two χ^2 -outcomes:

$$\chi_{\text{solar+KL}}^2 = \chi_{\text{solar}}^2(\Delta m_{21}^2, \tan^2 \theta_{12}, \sin^2 \theta_{13}) + \chi_{\text{KL}}^2(\Delta m_{21}^2, \tan^2 \theta_{12}, \sin^2 \theta_{13})$$

If we consider the solar without the Borexino data-set, the best fit point for the oscillation parameters lies in the LMA region and results to be:

$$\Delta m_{21}^2 = 7.50_{-0.22}^{+0.18} \times 10^{-5} \text{ eV}^2, \quad \tan^2 \theta_{12} = 0.462_{-0.033}^{+0.037}, \quad \text{and} \quad \sin^2 \theta_{13} = 0.023_{-0.018}^{+0.015}.$$

with a minimum $\chi_{\text{solar+KL}}^2/\text{ndf}$ ratio of 97.4/95.

As we expect, once included the Borexino results, the situation does not change significantly: the best fit point still belongs to the LMA regime and it is only slightly modified in the $\tan^2 \theta_{12}$ sector.

$$\Delta m_{21}^2 = 7.50_{-0.21}^{+0.18} \times 10^{-5} \text{ eV}^2, \quad \tan^2 \theta_{12} = 0.457_{-0.025}^{+0.038}, \quad \text{and} \quad \sin^2 \theta_{13} = 0.023_{-0.018}^{+0.014}.$$

The minimum $\chi_{\text{solar+KL}}^2/\text{ndf}$ ratio is 97.8/104.

The plot in Fig. 5.11 reports the allowed regions by the all solar (Borexino included) plus KamLAND global analysis. These results are in perfect agreement with those obtained from different global analysis (e.g. Ref. [38, 35]).

For what concerns θ_{13} , as we could observe in Fig. 5.10, the apparently mismatch between the solar and KamLAND allowed regions can be accomodated by assuming $\theta_{13} \neq 0$. Indeed, the χ^2 -fit prefers a non-zero θ_{13} solution the combination of the solar and KamLAND results actually states $\sin^2 \theta_{13} > 0$ at more than 1σ (Fig. 5.12).

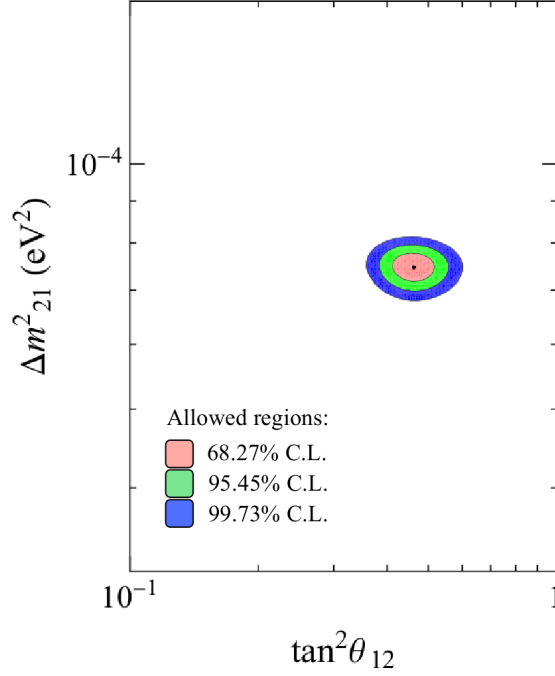


Figure 5.11: The analysis of the joint solar (Borexino included) and KamLAND dataset, in the $\tan^2 \theta_{12} - \Delta m_{21}^2$ space, after marginalization over $\sin^2 \theta_{13}$. Allowed regions ($d.o.f. = 2$) at 68.27% C.L. (pink), 95.45% C.L. (green) and 99.73% C.L. (blue).

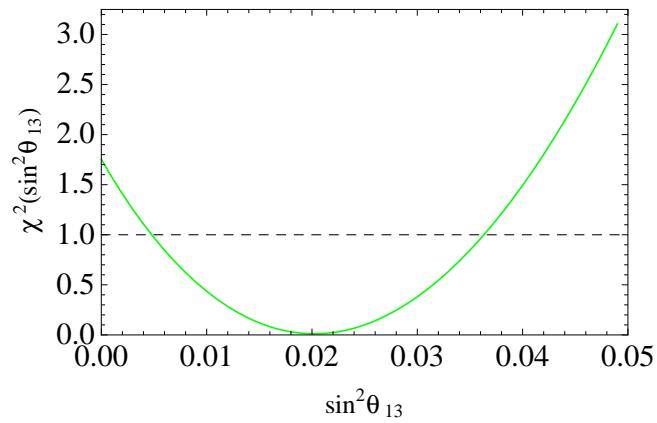


Figure 5.12: χ^2 -profile for $\sin^2 \theta_{13}$, obtained by the joint analysis of solar and KamLAND data. The black dashed line indicates the 1σ [$\chi^2(\sin^2 \theta_{13}) = 1$] level.

5.4 Terrestrial neutrino sources contribution

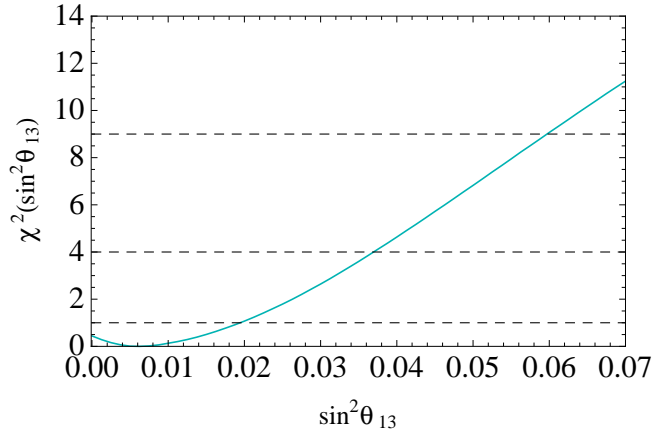


Figure 5.13: χ^2 -profile for $\sin^2 \theta_{13}$, obtained by the analysis of the atmospheric, reactor (CHOOZ) and accelerator (MINOS, LBL) data in Ref. [78]. The black dashed lines indicate the 1σ [$\chi^2(\sin^2 \theta_{13}) = 1$], 2σ [$\chi^2(\sin^2 \theta_{13}) = 4$] and 3σ [$\chi^2(\sin^2 \theta_{13}) = 9$] levels.

5.4 Terrestrial neutrino sources contribution

The contribution from atmospheric (SK I+II+III), reactor (CHOOZ experiment only), and accelerator experiments (MINOS + LBL), the so-called *terrestrial contribution*, is the last result we want to include in our global analysis of neutrino data.

This piece of information is directly taken from Ref. [78] and consists in a function $\chi^2_{\text{terrestrial}}(\theta_{13})$ resulting from the analysis over the data set above mentioned.

In their paper, Gonzalez-Garcia, Maltoni and Salvado states that the 1σ range for $\sin^2 \theta_{13}$ as determined from the joint analysis of atmospheric, CHOOZ, MINOS and LBL data is:

$$\sin^2 \theta_{13} = 0.006^{+0.012}_{-0.007},$$

where the lower 1σ bound to the unphysical region $\sin^2 \theta_{13} < 0$ is also indicated.

For this analysis, it is $\chi^2_{\text{terrestrial}}/\text{ndf}$ ratio of $64.7/80$ ³. Figure 5.13 shows the $\chi^2_{\text{terrestrial}}$ -profile for $\sin^2 \theta_{13}$ and the 68.27% C.L., 95.45% C.L., and 99.73% C.L..

³M. Maltoni, private communication (2011)

5.5 Global analysis of neutrino data

The results of our global analysis of solar and KamLAND plus the *terrestrial* contribution are summarized in Fig. 5.14, where we show the allowed regions of the $\tan^2 \theta_{12} - \Delta m_{21}^2$ space of parameters. Those regions correspond to the analysis done in the framework of the SHP11 Standard Solar Model and are obtained after marginalization of χ_{global}^2 with respect to the undisplayed parameter $\sin^2 \theta_{13}$.

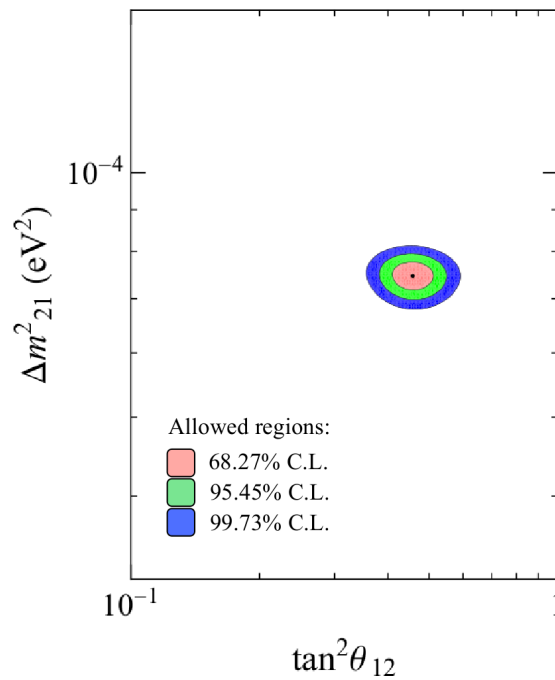


Figure 5.14: The global analysis of solar (Borexino included), KamLAND and *terrestrial* (atmospheric, CHOOZ, MINOS, LBL) data-set in the $\tan^2 \theta_{12} - \Delta m_{21}^2$ space, after marginalization over $\sin^2 \theta_{13}$. Allowed regions (*d.o.f.* = 3) at 68.27% C.L. (pink), 95.45% C.L. (green) and 99.73% C.L. (blue).

Since in Eq. 5.1 we define:

$$\chi_{global}^2 = \chi_{solar}^2 + \chi_{KL}^2 + \chi_{terrestrial}^2,$$

we sum the results of the two partial χ^2 -analysis (solar+KL and terrestrial), we compute the absolute minimum and we marginalized over the oscillation parameters in order to obtain the usual $\tan^2 \theta_{12} - \Delta m_{21}^2$ plot and the uncertainties of each parameter.

5.6 The free-fluxes analysis

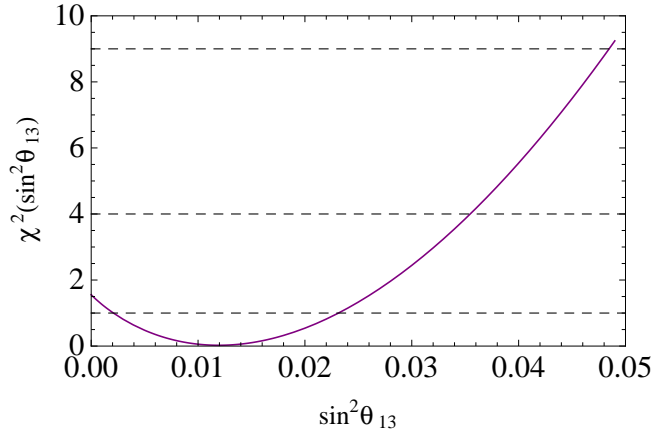


Figure 5.15: χ^2 -profile for $\sin^2 \theta_{13}$, obtained by the global analysis of neutrino data. The black dashed lines indicate the 1σ [$\chi^2(\sin^2 \theta_{13}) = 1$], 2σ [$\chi^2(\sin^2 \theta_{13}) = 4$] and 3σ [$\chi^2(\sin^2 \theta_{13}) = 9$] levels.

Figure 5.14 shows the allowed regions in the $\tan^2 \theta_{12} - \Delta m_{21}^2$ space of parameters while Fig. 5.15 shows the $\sin^2 \theta_{13}$ -profile from the χ^2_{global} analysis. From this latter plot, it is clear that the combination of all the data coming from neutrino and anti-neutrino experiment prefers a $\theta_{13} \neq 0$ value within 1σ .

Hence, if one considers a global analysis of neutrino data coming from the solar, reactors, and accelerators experiments, the best-fit for the neutrino oscillation parameters belongs to the LMA region and, within the 1σ bound, it is:

$$\Delta m_{21}^2 = 7.50^{+0.17}_{-0.23} \times 10^{-5} \text{ eV}^2, \quad \tan^2 \theta_{12} = 0.457^{+0.031}_{-0.033}, \quad \text{and} \quad \sin^2 \theta_{13} = 0.013^{+0.010}_{-0.011}.$$

The final minimum $\chi^2_{global}/\text{ndf}$ ratio is 163.2/184. These values are in very good agreement with other global analysis performed by different groups (Ref. [38, 78]).

5.6 The free-fluxes analysis

All the analysis described so far were performed under the assumption that the expected neutrino fluxes were the ones predicted by the high-metallicity hypothesis of the SHP11 standard solar model (Tab. 1.2), including their estimated (and correlated) uncertainties.

The so-called *solar metallicity controversy* was introduced in Sec. 1.3.3 as a debate arisen because some calculations (Ref. [17, 16]) show a new (lower) metallicity values in the sun and in its core. It follows that modified input abundances might cause a significant change in the prediction of the neutrino fluxes which would be more or less relevant depending on the particular source.

The best way to approach the study of the Standard Solar Model parameters and to look deeper into the low/high metallicity controversy is to analyze the data by leaving $\Phi(^7\text{Be})$, $\Phi(^8\text{B})$ and $\Phi(\text{CNO})$ as free parameters of the fit.

In order to do so, we follow the usual convention and we define the reduced fluxes (or astrophysical factors) by the parameters f_{Be} , f_{B} and f_{CNO} , where f_i is the ratio of the true flux to the flux predicted by the SHP11 model (Ref. [18]). Thus, in beryllium and boron case, the reduced fluxes are:

$$f_{\text{Be}} = \frac{\Phi(^7\text{Be})}{\Phi(^7\text{Be})_{\text{SHP11}}} \quad \text{and} \quad f_{\text{B}} = \frac{\Phi(^8\text{B})}{\Phi(^8\text{B})_{\text{SHP11}}}. \quad (5.2)$$

Similarly, we define the reduced ^{13}N , ^{15}O and ^{17}F neutrino fluxes via a common parameter f_{CNO} . According to Ref. [86], different limiting cases in the relative weights of the ^{13}N , ^{15}O and ^{17}F should not affect the accuracy of our results; thus we take:

$$f_{\text{CNO}} = \frac{\Phi(^{15}\text{O})}{\Phi(^{15}\text{O})_{\text{SHP11}}} = \frac{\Phi(^{13}\text{N})}{\Phi(^{13}\text{N})_{\text{SHP11}}} = \frac{\Phi(^{17}\text{F})}{\Phi(^{17}\text{F})_{\text{SHP11}}}. \quad (5.3)$$

SOLAR NEUTRINO FLUXES - SHP11

ν Flux	High Metallicity	Low Metallicity	Difference %
^7Be	5.00(1 ± 0.07)	4.56(1 ± 0.07)	8.8
^8B	5.58(1 ± 0.14)	4.59(1 ± 0.14)	17.7
^{13}N	2.96(1 ± 0.14)	2.17(1 ± 0.14)	26.7
^{15}O	2.23(1 ± 0.15)	1.56(1 ± 0.15)	30.0
^{17}F	5.52(1 ± 0.17)	3.40(1 ± 0.16)	38.4

Table 5.2: Extract of Tab. 1.2. Some of the neutrino fluxes as predicted by the SHP11 Solar model (Ref. [18]) having as input the GS98 high metallicity solution (Ref. [15]) and the AGSS09 low metallicity solution (Ref. [17]). The percentage difference among the two predictions is indicated. The fluxes are given in units of $10^9(^7\text{Be})$, $10^8(^{13}\text{N}, ^{15}\text{O})$, and $10^6(^8\text{B}, ^{17}\text{F}) \text{ cm}^{-2} \text{ s}^{-1}$. Asymmetric uncertainties have been averaged.

5.6 The free-fluxes analysis

Table 5.2 reports the fluxes of ${}^7\text{Be}$, ${}^8\text{B}$ and CNO neutrinos as predicted by the SHP11 Solar model, having as input the GS98 high metallicity solution (Ref. [15]) and the AGSS09 low metallicity solution (Ref. [17]). The complete list of SHP11 solar neutrino fluxes can be found in Tab. 1.2.

Another key step in our analysis is to include the luminosity constraint (Ref. [87, 88]), which implements the conservation of energy during the fusion of light elements in the sun. Each neutrino flux is associated with a specific amount of energy released to the star and therefore a particular linear combination of the solar neutrino fluxes is proportional to the solar luminosity. One can write the luminosity constraint as:

$$\frac{L_{\odot}}{4\pi (\text{A.U.})^2} = \sum_i \alpha_i \Phi_i, \quad (5.4)$$

where L_{\odot} is the solar luminosity measured at the earth's surface, 1 A.U. is the average earth-sun distance, and the coefficient α_i is the amount of energy provided to the star by nuclear fusion reactions associated with each of the solar neutrino fluxes, Φ_i . The coefficients α_i are accurately calculated in Ref. [87].

If the standard solar model describes with a relatively good approximation the actual solar properties, then the luminosity constraint can be conveniently written in two dimensionless forms (Ref. [66]).

The *strongform* uses both f_{Be} and f_{CNO} and it is:

$$f_{\text{pp}} = 1.09 - 0.08 f_{\text{Be}} - 0.01 f_{\text{CNO}}. \quad (5.5)$$

The *weakform* concerns only f_{Be} and it is defined as:

$$f_{\text{pp}} = 1.08 - 0.08 f_{\text{Be}}. \quad (5.6)$$

Our main goals are to give a quantitative estimation of the f_{Be} , f_{B} , f_{CNO} parameters and to study the impact of the Borexino results in determining these parameters. All the analysis, reported in the next paragraphs, were carried out assuming $\theta_{13} = 0$.

5.6.1 Berillium and boron fluxes as free parameters

Taking into account all the definitions given so far, we can easily evaluate the expectation of f_{Be} and f_{B} values in case of high or low metallicity hypothesis.

If one assumes the high-metallicity hypothesis (Ref. [15, 18]), then the theoretical

berillium and boron reduced fluxes have central values equal to 1 by construction, and errors estimated as:

$$f_{\text{Be}} = 1.00 \pm 0.07 \quad \text{and} \quad f_{\text{B}} = 1.00 \pm 0.14 . \quad (5.7)$$

Instead, in case of low-metallicity hypothesis (Ref. [17, 16, 18]), the theoretical fluxes are:

$$f_{\text{Be}} = 0.91 \pm 0.06 \quad \text{and} \quad f_{\text{B}} = 0.82 \pm 0.11 . \quad (5.8)$$

We now discuss how these expectations compare with the experimental data. In this branch of the analysis, we compute a new χ^2_{solar} which is now defined as:

$$\chi^2_{\text{solar}} = \chi^2_{\text{solar}}(\Delta m_{21}^2, \tan^2 \theta_{12}, \sin^2 \theta_{13}, f_{\text{Be}}, f_{\text{B}})$$

In particular, we let f_{Be} and f_{B} free to vary between

$$0.5 < f_{\text{Be}} < 1.6 \quad \text{and} \quad 0.71 < f_{\text{B}} < 1.14 ,$$

while we fix the remaining neutrino fluxes to the values predicted by the high metallicity version of the SHP11 model. We impose the weak form of the luminosity constant (Eq. 5.6), we computed the χ^2_{solar} in the usual way and we obtain the final χ^2 by summing the KamLAND contribution (in case of $\sin \theta_{13} = 0$).

When the fit is performed on the KamLAND and solar-without-Borexino data-set, the constraint on berillium is very weak and the best value for f_{Be} and f_{B} are found to be:

$$f_{\text{Be}} = 0.76^{+0.22}_{-0.21} \quad \text{and} \quad f_{\text{B}} = 0.90^{+0.02}_{-0.02} .$$

This is due to the fact that ${}^7\text{Be}$ flux is very poorly constrained by any solar experiment other than Borexino.

Once Borexino is included with its current measurements, the situation changes dramatically and the best fit values for f_{Be} and f_{B} result:

$$\begin{aligned} f_{\text{Be}} = 0.95^{+0.05}_{-0.04} &\quad \longrightarrow \quad \Phi_{\text{Be}} = (4.75^{+0.26}_{-0.22}) \times 10^9 \nu \text{ cm}^{-2} \text{ s}^{-1} , \\ f_{\text{B}} = 0.90^{+0.02}_{-0.02} &\quad \longrightarrow \quad \Phi_{\text{B}} = (5.02^{+0.17}_{-0.19}) \times 10^6 \nu \text{ cm}^{-2} \text{ s}^{-1} . \end{aligned}$$

The effect of Borexino in the determination of f_{Be} can be clearly seen in Fig. 5.16 where the allowed region for f_{Be} and f_{B} are shown for the fit performed without (left panel) and with (right panel) the Borexino results.

For what concerns f_{B} , the best fit value obtained with the two data-sets does not

5.6 The free-fluxes analysis

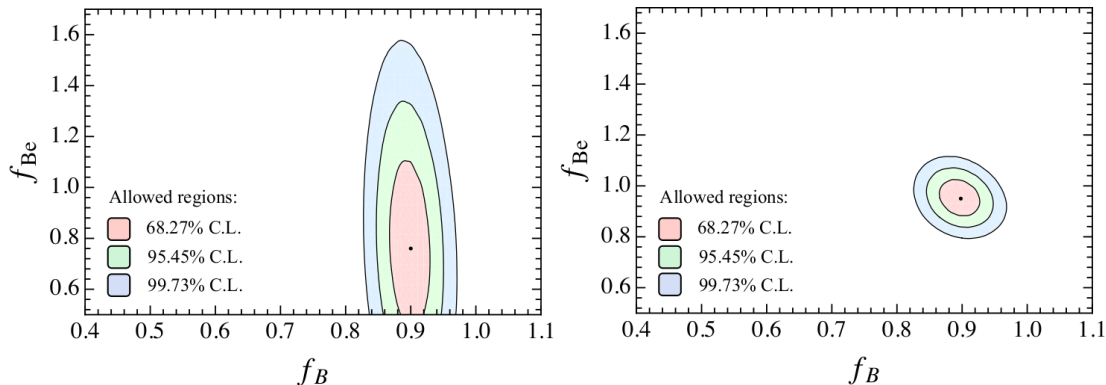


Figure 5.16: The global analysis of solar (without Borexino, on the left; Borexino included, on the right) and KamLAND results in the $f_{\text{Be}}-f_{\text{B}}$ space, after marginalizing over Δm_{21}^2 and $\tan^2 \theta_{12}$, in the $\theta_{13}=0$ case. Allowed regions at 68.27% C.L. (light pink), 95.45% C.L. (light green) and 99.73% C.L. (light blue).

change significantly since the ${}^8\text{B}$ flux is mainly determined by the results of the SNO and Super Kamiokande experiments.

The best fit for the oscillation parameters Δm_{21}^2 and $\tan^2 \theta_{12}$ are found to be:

$$\Delta m_{21}^2 = 7.50_{-0.23}^{+0.17} \times 10^{-5} \text{ eV}^2, \quad \tan^2 \theta_{12} = 0.452_{-0.034}^{+0.029},$$

fully compatible with those obtained in Sec. 5.5 by fixing all the fluxes to the SHP11 Standard Solar Model predictions.

It is interesting to compare the result of the global analysis on solar (Borexino included) plus KamLAND results, with the theoretical expectations for f_{Be} and f_{B} .

From Fig. 5.17 it is clear that solar neutrino data cannot discriminate between the low or high metallicity hypothesis in the solar model: both the 1σ theoretical range of low and high metallicity models lies in the 3σ allowed region by the current solar plus KamLAND data.

At present, no experimental results could help in disentangling between the two metallicity scenarios: the theoretical error on ${}^7\text{Be}$ and ${}^8\text{B}$ is as large as their experimental precision. An improvement in the determination of the different solar parameters is needed.

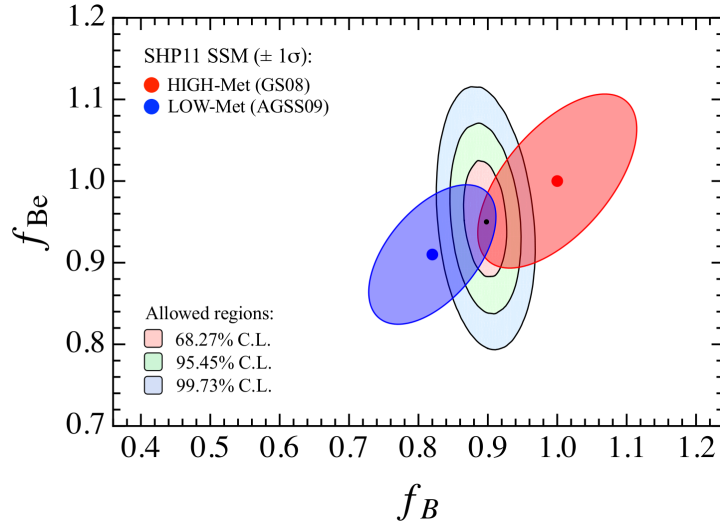


Figure 5.17: The 1σ theoretical range of high (red) and low (blue) metallicity model for f_{Be} and f_{B} , compared to the 1σ (light pink), 2σ (light green) and 3σ (light blue) allowed regions by the global analysis of solar (Borexino included) and KamLAND results. The theoretical correlation factors are taken from Ref. [57].

5.6.2 CNO fluxes as free parameters

The CNO neutrino fluxes are poorly constrained by radiochemical, SNO and Super Kamiokande experiments. It is therefore interesting to study the impact of the Borexino results, especially the ${}^7\text{Be}$ result, in determining f_{CNO} .

To this aim, as in the berillium-boron case, we build a new χ^2_{solar} , characterized by 6 free parameters: Δm_{21}^2 , $\tan^2 \theta_{12}$, $\sin^2 \theta_{13}$, f_{Be} , f_{B} , and f_{CNO} .

In particular, we let f_{Be} , f_{B} and f_{CNO} free to vary between

$$0.5 < f_{\text{Be}} < 1.6, \quad 0.71 < f_{\text{B}} < 1.14 \quad \text{and} \quad 0 < f_{\text{CNO}} < 6,$$

and we impose the strong form of the luminosity constraint as in Eq. 5.5. Then the final χ^2 is computed in the usual way by summing the KamLAND contribution (again, assuming $\theta_{13}=0$).

After marginalizing over Δm_{21}^2 , $\tan^2 \theta_{12}$ and f_{B} , we obtain the $n\text{-}\sigma$ allowed regions in case of solar-without-Borexino plus KamLAND (Fig. 5.18, left panel) and solar-with-Borexino plus KamLAND (Fig. 5.18, right panel).

From Fig. 5.18 and Fig. 5.19 it is clear that the Borexino results are fundamental in constraining f_{CNO} . The global fit however, does not give a significant hint for nonzero

5.6 The free-fluxes analysis

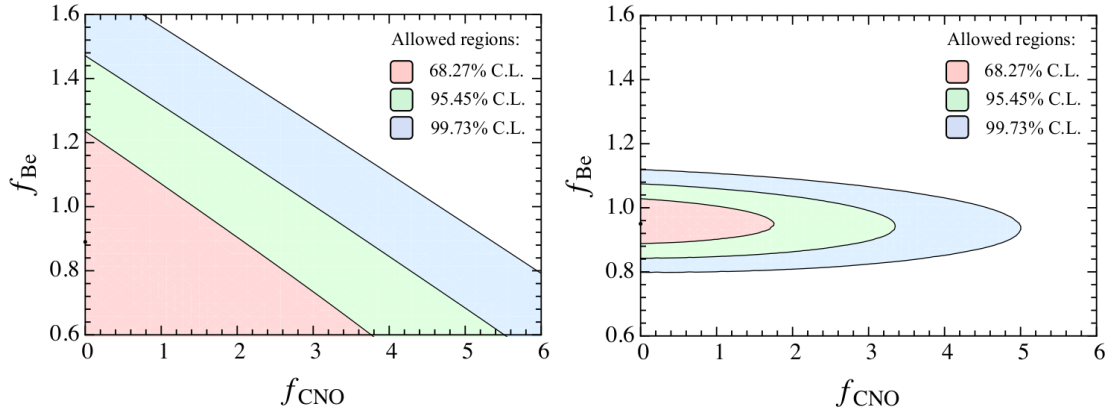


Figure 5.18: The global analysis of solar (without Borexino, on the left; Borexino included, on the right) and KamLAND results in the f_{Be} - f_{CNO} space, after marginalizing over Δm_{21}^2 , $\tan^2 \theta_{12}$ and f_{B} , in the $\theta_{13}=0$ case. Allowed regions at 68.27% C.L. (light pink), 95.45% C.L. (light green) and 99.73% C.L. (light blue).

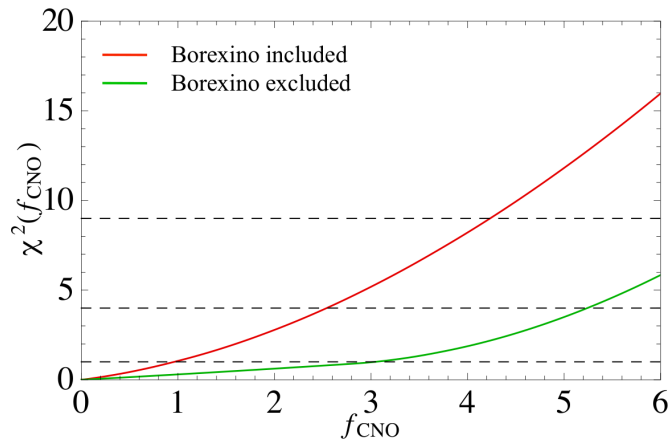


Figure 5.19: f_{CNO} χ^2 -profile obtained by the global analysis of solar (with/without Borexino) plus KamLAND data. The green line shows the Borexino excluded case; the red line shows the Borexino included case. The black dashed lines indicate the 1σ [$\chi^2(f_{\text{CNO}}) = 1$], 2σ [$\chi^2(f_{\text{CNO}}) = 4$] and 3σ [$\chi^2(f_{\text{CNO}}) = 9$] levels.

CNO neutrinos flux value, remaining the best fit $f_{\text{CNO}} = 0$. The following upper limits at 68.27% C.L. (95% C.L.) can be derived for f_{CNO} .

If one considers the solar-without-Borexino plus KamLAND data-set, then the upper bound is:

$$f_{\text{CNO}} \leq 3.04 (\leq 5.17) .$$

Instead, if Borexino is included, the upper bound is strengthened to:

$$f_{\text{CNO}} \leq 0.96 (\leq 2.48) \quad \longrightarrow \quad \Phi_{\text{CNO}} \leq 1.3 \times 10^9 \nu \text{ cm}^{-2} \text{ s}^{-1} \text{ at 95\% C.L. .}$$

Figure 5.19 shows the f_{CNO} χ^2 -profile we obtained after marginalizing over f_{Be} : the green line refers to the solar (Borexino excluded) plus KamLAND data-set while the red line indicate the f_{CNO} behaviour, as determined by the solar (Borexino included) plus KamLAND global analysis. Up-to-now, this is the strongest available constraint on f_{CNO} .

Finally, it is interesting to evaluate the impact of the Borexino in determining f_{pp} and therefore the pp solar neutrino flux.

Using the strong form of the luminosity constraint (Eq. 5.5), we express f_{CNO} as a function of f_{pp} and f_{Be} :

$$f_{\text{CNO}} = (1.09 - f_{\text{pp}} - 0.08 f_{\text{Be}})/0.01 . \tag{5.9}$$

In this way, CNO is free to vary within the limit imposed by the luminosity constraint.

If Borexino is excluded, then the combination of the other neutrino experiments foresees:

$$f_{\text{pp}} = 1.019_{-0.018}^{+0.011} .$$

Once we include the Borexino contribution, we find:

$$f_{\text{pp}} = 1.013_{-0.010}^{+0.003} \quad \longrightarrow \quad \Phi_{\text{pp}} = (6.06_{-0.06}^{+0.02}) \times 10^{10} \nu \text{ cm}^{-2} \text{ s}^{-1} .$$

It is worth to notice that both the precision of the pp flux determination and the constraint on the CNO flux are improved approximately a factor of 2 by the inclusion of the Borexino results.

Conclusion

The main purpose of the work I presented in this thesis was to analyze and understand the implications of the Borexino results in neutrino oscillation physics and solar interior astrophysics.

My personal contribution consisted in reviewing, improving and developing a code that the Borexino collaboration can now use to evaluate the actual impact of its measurements in the global analysis of neutrino data.

The results I obtained were included in two very recent Borexino publications: the analysis of the astrophysical factors f_{Be} and f_{CNO} (Sec. 5.6) was part of the paper “Precision measurement of the ${}^7\text{Be}$ solar neutrino interaction rate in Borexino,” published on *Physical Review Letters* (Ref. [1]); the inclusion of the Borexino day-night asymmetry in the solar analysis and its impact in ruling out the LOW-MSW regime (Sec. 5.1.4), were inserted in the paper “Absence of a day-night asymmetry in the ${}^7\text{Be}$ solar neutrino rate in Borexino,” published on *Physics Letters B* (Ref. [2]).

In this dissertation, we first studied the impact of each single piece of information coming from the Borexino experiment in determining the allowed regions of the $(\tan^2\theta_{12}, \Delta m_{21}^2)$ space of parameters. We performed a χ^2 -based global analysis by combining the ${}^7\text{Be}$ neutrino flux measurement, the ${}^8\text{B}$ neutrino flux above 3 MeV signal and its relative spectral shape, the null day-night asymmetry of the ${}^7\text{Be}$ rate and also the very recent pep neutrino flux measurement.

We also combined the Borexino results with those obtained by the other solar experiment (GALLEX/GNO, SAGE, Homestake, Super Kamiokande, SNO) and we showed that, thanks to the Borexino inclusion, the LOW region of MSW regime is, for the first time, strongly disfavored by solar neutrino data alone. The LMA solution is singled out with very high confidence (at more than 8.5σ), without the inclusion of any anti-neutrino data and therefore without invoking CPT symmetry. We then added to the analysis also the reactor (KamLAND) contribution and the information on θ_{13} coming from the atmospheric (Super Kamiokande), reactor (CHOOZ) and LBL accelerator

experiments. Our best fit ($\pm 1\sigma$) for the oscillation parameters resulted to be:

$$\Delta m_{21}^2 = 7.50_{-0.23}^{+0.17} \times 10^{-5} \text{ eV}^2, \quad \tan^2 \theta_{12} = 0.457_{-0.033}^{+0.031}, \quad \text{and} \quad \sin^2 \theta_{13} = 0.013_{-0.011}^{+0.010}.$$

For what regards solar astrophysics, trying to disentangle the so-called “solar metallicity controversy”, we analyzed the data by leaving $\Phi(^7\text{Be})$, $\Phi(^8\text{B})$ and $\Phi(\text{CNO})$ as free parameters of the fit. Again, the analysis was performed on the solar-without-Borexino and solar-with-Borexino data set.

By imposing the luminosity constraint, we evaluated the theoretical expectations for the reduced fluxes f_{Be} and f_{B} in both the high-metallicity and the low-metallicity hypothesis and we then compared with the experimental data preferences. The final result is that, at present, solar neutrino data cannot discriminate between low or high metallicity hypothesis in the solar model: both the 1σ theoretical range of low and high metallicity models lies in the 3σ allowed region by the current neutrino data.

We were able to set an upper limit (at 95% C.L.) for f_{CNO} that is for the CNO neutrinos flux and up-to-now, this is the strongest available constraint. We also determined the best fit value for f_{pp} i.e. we evaluate the pp solar neutrino flux. Both the precision of the pp flux determination and the constraint on the CNO flux were improved approximately a factor 2 by the inclusion of the Borexino results.

List of publications and activities of Alessandra Carlotta Re

Publications on refereed journals

- *“First evidence of pep solar neutrinos by direct detection in Borexino,”*
G. Bellini *et al.* (the Borexino collaboration),
Physical Review Letters, vol. 108, 051302 (2012).
- *“Absence of a day-night asymmetry in the ${}^7\text{Be}$ solar neutrino rate in Borexino,”*
G. Bellini *et al.* (the Borexino collaboration),
Physics Letters B, vol. 707, pp. 22 (2012).
- *“Precision measurement of the ${}^7\text{Be}$ solar neutrino interaction rate in Borexino,”*
G. Bellini *et al.* (the Borexino collaboration),
Physical Review Letters, vol. 107, 141302 (2011).
- *“Muon and cosmogenic neutron detection in Borexino,”*
G. Bellini *et al.* (the Borexino collaboration),
Journal of Instrumentation, vol. 6, pp. 05005 (2011).
- *“Study of solar and other unknown anti-neutrino fluxes with Borexino at LNGS,”*
G. Bellini *et al.* (the Borexino collaboration),
Physics Letters B, vol. 696, pp. 191 (2011).
- *“Measurement of the solar ${}^8\text{B}$ neutrino rate with a liquid scintillator target and
3 MeV energy threshold in the Borexino detector,”*
G. Bellini *et al.* (the Borexino collaboration),
Physical Review D, vol. 82, pp. 033006 (2010).

-
- “*Observation of geo-neutrinos,*”
G. Bellini *et al.* (the Borexino collaboration),
Physics Letters B, vol. 687, pp. 299 (2010).
 - “*New experimental limits on the Pauli-forbidden transitions in ^{12}C nuclei obtained with 485 days Borexino data,*”
G. Bellini *et al.* (the Borexino collaboration),
Physical Review C, vol. 81, pp. 034317 (2010).

Borexino internal notes

- “*Absence of day night asymmetry of ^7Be solar neutrinos,*”
B. Caccianiga, L. Ludhova, C. Peña-Garay, A. Re and G. Testera,
February 2011.
- “*Global analysis of neutrino data: the impact of Borexino present and future results,*”
B. Caccianiga, L. Perasso, C. Peña-Garay and A. Re,
June 2010.

Talks, posters and proceedings

- “*The Borexino impact in the global analysis of neutrino data,*”
Talk at SIF 2011, Congresso della Società Italiana di Fisica (L’Aquila, Italy, 2011).
- “*The Borexino impact in the global analysis of neutrino data,*”
Poster at TAUP 2011, 12th International Conference on Topics in Astroparticle and Underground Physics (München, Germany, 2011).
Proceedings in print.
- “*A road to reach higher precision in Borexino: the detector calibration campaigns,*”
Proceeding of NeuTel 2011, XIV International Workshop on Neutrino Telescopes (Venezia, Italy, 2011).
Published by M. Mezzetto (Papergraf Editions, Padova, Italy), p. 421.
- “*Geo-neutrinos signal with Borexino,*”
Proceeding of IFAE 2010, Incontri di Fisica delle Alte Energie (Roma, Italy, 2010).
Best communication award.
Il Nuovo Cimento C, vol. 33, pp. 213 (2011).

Seminars

- *“An experimental approach to dark matter,”*
Università degli Studi di Milano, Milano (Italy), November 2010.
- *“An outlook on the Borexino impact in the global analysis of neutrino data,”*
Università degli Studi di Milano-Bicocca, Milano (Italy), November 2010.

Fellowships

- INFN (Istituto Nazionale di Fisica Nucleare) fellowship for undergraduate students; November 2009 - November 2011.

Teaching

- Teaching assistant for the “Fisica Generale 1” class, Mathematics degree course.
Subjects: classical mechanics, fluid statics, thermodynamics;
March 2011 - January 2012,
Università degli Studi di Milano, Milano (Italy).

Schools attended

- *“ISAPP 2010 - International school on astroparticle Physics: a multi-messenger approach to astroparticle Physics,”*
Zaragoza (Spain), July 2010.
- *“International school of nuclear Physics: neutrinos in cosmology, in astro-, particle- and nuclear Physics,”*
Erice (Italy), September 2009.

Appendix A

Results of global analyses

In this appendix we summarize the results of the several analyses that we performed on different neutrino data sets, and we show explicit results for $\theta_{13} \neq 0$. We report either the best fit value together with its $\pm 1\sigma$ bounds or, the $+1\sigma$ upper limit.

Table A.1, Tab. A.2, Tab. A.3 and Tab. A.4 describe the results obtained with different values of θ_{13} by the Borexino, radiochemical, SNO and Super Kamiokande experiments respectively.

The analysis on KamLAND data alone (partial results in Tab. A.5) identifies the following best fit points:

$$\Delta m_{21}^2 = 7.50_{-0.20}^{+0.19} \times 10^{-5} \text{ eV}^2, \quad \tan^2 \theta_{12} = 0.44_{-0.06}^{+0.07}, \quad \text{and} \quad \sin^2 \theta_{13} < 0.034.$$

Partial results of the solar analyses are reported in Tab. A.6 and Tab. A.7. For what concerns the solar-with-Borexino analysis, the best fit points for the oscillation parameters belong to the LMA-MSW region:

$$\Delta m_{21}^2 = 5.4_{-1.1}^{+1.7} \times 10^{-5} \text{ eV}^2, \quad \tan^2 \theta_{12} = 0.468_{-0.044}^{+0.031}, \quad \text{and} \quad \sin^2 \theta_{13} < 0.030.$$

The solar plus KamLAND analysis (see Tab. A.8) identifies as best fit points for the oscillation parameters:

$$\Delta m_{21}^2 = 7.50_{-0.21}^{+0.18} \times 10^{-5} \text{ eV}^2, \quad \tan^2 \theta_{12} = 0.457_{-0.025}^{+0.038}, \quad \text{and} \quad \sin^2 \theta_{13} = 0.023_{-0.018}^{+0.014}.$$

Finally, the global analysis definitely prefers the LMA-MSW oscillation solution and indicates as best fit for the oscillation parameters:

$$\Delta m_{21}^2 = 7.50_{-0.23}^{+0.17} \times 10^{-5} \text{ eV}^2, \quad \tan^2 \theta_{12} = 0.457_{-0.033}^{+0.031}, \quad \text{and} \quad \sin^2 \theta_{13} = 0.013_{-0.011}^{+0.010}.$$

THE BOREXINO EXPERIMENT

$\sin^2 \theta_{13}$	$\tan^2 \theta_{12}$	$\Delta m_{21}^2 (\times 10^{-5} \text{ eV}^2)$	$\chi^2 (\text{ndf}=7)$
0.000	$4.4^{+14.8}_{-2.6}$	$0.46^{+0.19}_{-0.18}$	0.358
0.001	$4.4^{+15.5}_{-2.6}$	$0.46^{+0.18}_{-0.17}$	0.359
0.003	$4.4^{+15.8}_{-2.6}$	$0.46^{+0.18}_{-0.17}$	0.362
0.005	$4.4^{+16.2}_{-2.5}$	$0.46^{+0.17}_{-0.17}$	0.367
0.007	$5.6^{+15.1}_{-3.7}$	$0.44^{+0.19}_{-0.16}$	0.363
0.009	$5.6^{+15.3}_{-3.7}$	$0.44^{+0.18}_{-0.15}$	0.358
0.011	$5.6^{+15.5}_{-3.7}$	$0.44^{+0.18}_{-0.15}$	0.354
0.013	$6.1^{+15.1}_{-4.1}$	$0.44^{+0.17}_{-0.17}$	0.351
0.015	$6.1^{+15.3}_{-4.1}$	$0.43^{+0.14}_{-0.18}$	0.347
0.017	$6.1^{+15.5}_{-4.1}$	$0.43^{+0.14}_{-0.18}$	0.345
0.019	$6.8^{+15.0}_{-4.7}$	$0.43^{+0.18}_{-0.14}$	0.344
0.021	$6.8^{+15.2}_{-4.7}$	$0.43^{+0.17}_{-0.14}$	0.340
0.023	$6.8^{+15.3}_{-4.7}$	$0.42^{+0.17}_{-0.13}$	0.338
0.025	$7.0^{+15.2}_{-4.9}$	$0.42^{+0.17}_{-0.13}$	0.336
0.027	$7.4^{+15.0}_{-5.3}$	$0.42^{+0.17}_{-0.12}$	0.335
0.029	$7.7^{+14.8}_{-5.5}$	$0.41^{+0.17}_{-0.12}$	0.332
0.031	$7.7^{+14.9}_{-5.4}$	$0.41^{+0.17}_{-0.12}$	0.330
0.033	$7.7^{+15.0}_{-5.4}$	$0.41^{+0.16}_{-0.12}$	0.328
0.035	$7.7^{+15.1}_{-5.5}$	$0.40^{+0.16}_{-0.12}$	0.327
0.037	$7.9^{+15.0}_{-5.6}$	$0.40^{+0.16}_{-0.12}$	0.327
0.039	$8.1^{+15.0}_{-5.8}$	$0.39^{+0.16}_{-0.12}$	0.326
0.041	$8.8^{+14.3}_{-6.4}$	$0.39^{+0.16}_{-0.12}$	0.324
0.043	$8.6^{+14.6}_{-6.2}$	$0.39^{+0.16}_{-0.12}$	0.323
0.045	$8.9^{+14.4}_{-6.4}$	$0.38^{+0.16}_{-0.11}$	0.322
0.047	$8.9^{+14.5}_{-6.4}$	$0.38^{+0.16}_{-0.12}$	0.321
0.049	$9.2^{+14.4}_{-6.5}$	$0.38^{+0.16}_{-0.12}$	0.319

Table A.1: Results of the analysis of Borexino data alone (Ref. [1, 4, 2, 3]). The $\tan^2 \theta_{12}$ and Δm_{21}^2 best fit are indicated with their 1σ errors at each θ_{13} value.

THE RADIOCHEMICAL EXPERIMENTS

$\sin^2 \theta_{13}$	$\tan^2 \theta_{12}$	$\Delta m_{21}^2 (\times 10^{-5} \text{ eV}^2)$	$\chi^2 (\text{ndf}=0)$
0.000	$2.1_{-0.9}^{+5.0}$	$0.31_{-0.08}^{+0.11}$	0.00015
0.001	$2.1_{-0.9}^{+5.2}$	$0.31_{-0.08}^{+0.11}$	0.00004
0.003	$2.1_{-1.0}^{+5.5}$	$0.31_{-0.08}^{+0.11}$	0.00003
0.005	$2.2_{-1.0}^{+5.5}$	$0.31_{-0.08}^{+0.11}$	0.00039
0.007	$2.4_{-1.1}^{+5.6}$	$0.32_{-0.08}^{+0.11}$	0.00006
0.009	$2.4_{-1.1}^{+5.7}$	$0.32_{-0.08}^{+0.11}$	0.00000
0.011	$2.5_{-1.2}^{+5.8}$	$0.32_{-0.08}^{+0.10}$	0.00016
0.013	$2.6_{-1.3}^{+6.0}$	$0.32_{-0.08}^{+0.10}$	0.00043
0.015	$2.8_{-1.4}^{+6.0}$	$0.32_{-0.08}^{+0.10}$	0.00031
0.017	$2.9_{-1.5}^{+6.1}$	$0.32_{-0.08}^{+0.10}$	0.00012
0.019	$3.0_{-1.6}^{+6.2}$	$0.32_{-0.08}^{+0.10}$	0.00014
0.021	$3.2_{-1.7}^{+6.2}$	$0.32_{-0.08}^{+0.09}$	0.00002
0.023	$3.4_{-2.9}^{+6.2}$	$0.32_{-0.08}^{+0.09}$	0.00007
0.025	$3.5_{-3.1}^{+6.2}$	$0.32_{-0.08}^{+0.09}$	0.00014
0.027	$3.7_{-3.3}^{+6.2}$	$0.32_{-0.08}^{+0.09}$	0.00030
0.029	$4.0_{-3.0}^{+6.6}$	$0.32_{-0.08}^{+0.10}$	0.00009
0.031	$4.1_{-3.6}^{+6.1}$	$0.32_{-0.07}^{+0.09}$	0.00071
0.033	$4.3_{-3.9}^{+6.0}$	$0.32_{-0.07}^{+0.09}$	0.00016
0.035	$4.6_{-4.2}^{+5.9}$	$0.32_{-0.07}^{+0.08}$	0.00002
0.037	$4.8_{-4.3}^{+5.8}$	$0.31_{-0.07}^{+0.08}$	0.00079
0.039	$5.1_{-4.6}^{+5.7}$	$0.31_{-0.07}^{+0.08}$	0.00004
0.041	$5.2_{-4.7}^{+5.7}$	$0.31_{-0.06}^{+0.08}$	0.00041
0.043	$5.5_{-5.0}^{+5.5}$	$0.31_{-0.07}^{+0.08}$	0.00003
0.045	$5.6_{-5.2}^{+5.4}$	$0.31_{-0.06}^{+0.08}$	0.00009
0.047	$5.6_{-5.1}^{+5.7}$	$0.32_{-0.07}^{+0.08}$	0.00000
0.049	$6.3_{-5.8}^{+5.6}$	$0.30_{-0.07}^{+0.08}$	0.00011

Table A.2: Results of the analysis of radiochemical data alone (Ref. [25, 30, 29]). The $\tan^2 \theta_{12}$ and Δm_{21}^2 best fit are indicated with their 1σ errors at each θ_{13} value.

THE SNO EXPERIMENT

$\sin^2 \theta_{13}$	$\tan^2 \theta_{12}$	$\Delta m_{21}^2 (\times 10^{-7} \text{ eV}^2)$	$\chi^2 (\text{ndf}=4)$
0.000	$1.02^{+0.38}_{-0.13}$	$0.417^{+0.075}_{-0.091}$	2.94
0.001	$1.02^{+0.39}_{-0.14}$	$0.417^{+0.076}_{-0.091}$	2.93
0.003	$1.02^{+0.37}_{-0.14}$	$0.422^{+0.074}_{-0.095}$	2.91
0.005	$1.01^{+0.38}_{-0.14}$	$0.422^{+0.077}_{-0.095}$	2.89
0.007	$1.01^{+0.37}_{-0.14}$	$0.427^{+0.076}_{-0.098}$	2.88
0.009	$1.00^{+0.38}_{-0.14}$	$0.427^{+0.079}_{-0.097}$	2.84
0.011	$1.00^{+0.39}_{-0.13}$	$0.427^{+0.082}_{-0.096}$	2.82
0.013	$1.00^{+0.38}_{-0.14}$	$0.432^{+0.080}_{-0.100}$	2.81
0.015	$0.99^{+0.39}_{-0.13}$	$0.432^{+0.083}_{-0.099}$	2.79
0.017	$0.99^{+0.39}_{-0.14}$	$0.437^{+0.081}_{-0.103}$	2.77
0.019	$0.98^{+0.39}_{-0.14}$	$0.437^{+0.084}_{-0.102}$	2.75
0.021	$0.98^{+0.39}_{-0.14}$	$0.442^{+0.083}_{-0.106}$	2.73
0.023	$0.95^{+0.39}_{-0.14}$	$0.442^{+0.086}_{-0.105}$	2.72
0.025	$0.95^{+0.39}_{-0.14}$	$0.447^{+0.084}_{-0.109}$	2.70
0.027	$0.94^{+0.40}_{-0.14}$	$0.447^{+0.087}_{-0.109}$	2.68
0.029	$0.93^{+0.41}_{-0.13}$	$0.447^{+0.090}_{-0.108}$	2.67
0.031	$0.93^{+0.40}_{-0.14}$	$0.452^{+0.088}_{-0.112}$	2.65
0.033	$0.92^{+0.41}_{-0.13}$	$0.452^{+0.091}_{-0.111}$	2.64
0.035	$0.92^{+0.41}_{-0.14}$	$0.457^{+0.090}_{-0.115}$	2.62
0.037	$0.91^{+0.41}_{-0.14}$	$0.457^{+0.094}_{-0.114}$	2.61
0.039	$0.90^{+0.42}_{-0.13}$	$0.457^{+0.097}_{-0.113}$	2.60
0.041	$0.90^{+0.42}_{-0.14}$	$0.462^{+0.095}_{-0.118}$	2.58
0.043	$0.89^{+0.42}_{-0.13}$	$0.462^{+0.098}_{-0.117}$	2.57
0.045	$0.89^{+0.42}_{-0.14}$	$0.468^{+0.095}_{-0.122}$	2.56
0.047	$0.88^{+0.43}_{-0.13}$	$0.468^{+0.099}_{-0.121}$	2.55
0.049	$0.89^{+0.42}_{-0.14}$	$0.468^{+0.102}_{-0.121}$	2.53

Table A.3: Results of the analysis of SNO data alone (Ref. [35, 77]). The $\tan^2 \theta_{12}$ and Δm_{21}^2 best fit are indicated with their 1σ errors at each θ_{13} value.

THE SUPER KAMIOKANDE EXPERIMENT

$\sin^2 \theta_{13}$	$\tan^2 \theta_{12}$	$\Delta m_{21}^2 (\times 10^{-5} \text{ eV}^2)$	$\chi^2 (\text{ndf}=82)$
0.000	$5.1^{+3.0}_{-1.1}$	$0.556^{+0.071}_{-0.061}$	84.42
0.001	$5.1^{+2.9}_{-1.2}$	$0.562^{+0.076}_{-0.056}$	84.40
0.003	$5.2^{+2.8}_{-1.3}$	$0.556^{+0.065}_{-0.067}$	84.39
0.005	$5.1^{+3.0}_{-1.2}$	$0.562^{+0.067}_{-0.066}$	84.39
0.007	$5.1^{+3.0}_{-1.2}$	$0.569^{+0.070}_{-0.064}$	84.38
0.009	$5.1^{+2.9}_{-1.2}$	$0.569^{+0.066}_{-0.069}$	84.36
0.011	$5.2^{+3.0}_{-1.3}$	$0.575^{+0.070}_{-0.067}$	84.37
0.013	$5.1^{+3.0}_{-1.2}$	$0.569^{+0.059}_{-0.079}$	84.37
0.015	$5.2^{+3.0}_{-1.4}$	$0.582^{+0.068}_{-0.070}$	84.35
0.017	$5.2^{+2.9}_{-1.4}$	$0.589^{+0.072}_{-0.069}$	84.36
0.019	$5.1^{+3.1}_{-1.3}$	$0.596^{+0.075}_{-0.068}$	84.37
0.021	$5.2^{+3.1}_{-1.4}$	$0.596^{+0.069}_{-0.072}$	84.35
0.023	$5.2^{+3.1}_{-1.4}$	$0.603^{+0.074}_{-0.072}$	84.36
0.025	$5.3^{+3.0}_{-1.6}$	$0.603^{+0.070}_{-0.076}$	84.35
0.027	$5.2^{+3.1}_{-1.5}$	$0.610^{+0.073}_{-0.074}$	84.35
0.029	$5.4^{+3.0}_{-1.6}$	$0.610^{+0.068}_{-0.080}$	84.34
0.031	$5.2^{+3.0}_{-1.6}$	$0.617^{+0.070}_{-0.079}$	84.34
0.033	$5.2^{+3.1}_{-1.5}$	$0.624^{+0.075}_{-0.076}$	84.34
0.035	$5.1^{+3.3}_{-1.5}$	$0.631^{+0.078}_{-0.075}$	84.34
0.037	$5.2^{+3.3}_{-1.5}$	$0.631^{+0.073}_{-0.080}$	84.34
0.039	$5.2^{+3.2}_{-1.5}$	$0.638^{+0.075}_{-0.077}$	84.32
0.041	$5.2^{+3.3}_{-1.6}$	$0.638^{+0.071}_{-0.084}$	84.33
0.043	$5.2^{+3.3}_{-1.6}$	$0.646^{+0.075}_{-0.082}$	84.32
0.045	$5.1^{+3.3}_{-1.5}$	$0.653^{+0.079}_{-0.079}$	84.32
0.047	$5.2^{+3.3}_{-1.6}$	$0.653^{+0.074}_{-0.086}$	84.32
0.049	$5.2^{+3.5}_{-1.7}$	$0.661^{+0.073}_{-0.086}$	84.32

Table A.4: Results of the analysis of Super Kamiokande data alone (Ref. [31, 33]). The $\tan^2 \theta_{12}$ and Δm_{21}^2 best fit are indicated with their 1σ errors at each θ_{13} value.

THE KAMLAND EXPERIMENT

$\sin^2 \theta_{13}$	$\tan^2 \theta_{12}$	$\Delta m_{21}^2 (\times 10^{-5} \text{ eV}^2)$	$\chi^2 (\text{ndf}=4)$
0.000	$7.50^{+0.19}_{-0.20}$	$0.490^{+0.095}_{-0.067}$	2.44
0.001	$7.50^{+0.19}_{-0.20}$	$0.490^{+0.092}_{-0.069}$	2.40
0.003	$7.50^{+0.19}_{-0.20}$	$0.484^{+0.092}_{-0.067}$	2.32
0.005	$7.50^{+0.19}_{-0.20}$	$0.484^{+0.086}_{-0.070}$	2.24
0.007	$7.50^{+0.19}_{-0.20}$	$0.479^{+0.086}_{-0.068}$	2.17
0.009	$7.50^{+0.19}_{-0.20}$	$0.473^{+0.086}_{-0.066}$	2.10
0.011	$7.50^{+0.19}_{-0.20}$	$0.468^{+0.086}_{-0.064}$	2.04
0.013	$7.50^{+0.19}_{-0.20}$	$0.468^{+0.081}_{-0.067}$	1.99
0.015	$7.50^{+0.19}_{-0.20}$	$0.462^{+0.081}_{-0.065}$	1.94
0.017	$7.50^{+0.19}_{-0.20}$	$0.457^{+0.082}_{-0.062}$	1.90
0.019	$7.50^{+0.19}_{-0.20}$	$0.457^{+0.077}_{-0.066}$	1.87
0.021	$7.50^{+0.19}_{-0.20}$	$0.452^{+0.077}_{-0.063}$	1.84
0.023	$7.50^{+0.19}_{-0.20}$	$0.447^{+0.077}_{-0.061}$	1.82
0.025	$7.50^{+0.19}_{-0.20}$	$0.442^{+0.078}_{-0.059}$	1.81
0.027	$7.50^{+0.19}_{-0.20}$	$0.442^{+0.073}_{-0.062}$	1.80
0.029	$7.50^{+0.19}_{-0.20}$	$0.437^{+0.073}_{-0.060}$	1.79
0.031	$7.50^{+0.19}_{-0.20}$	$0.432^{+0.074}_{-0.058}$	1.79
0.033	$7.50^{+0.19}_{-0.20}$	$0.427^{+0.074}_{-0.056}$	1.80
0.035	$7.50^{+0.19}_{-0.20}$	$0.427^{+0.070}_{-0.059}$	1.82
0.037	$7.50^{+0.19}_{-0.20}$	$0.422^{+0.070}_{-0.057}$	1.84
0.039	$7.50^{+0.19}_{-0.20}$	$0.417^{+0.071}_{-0.056}$	1.86
0.041	$7.50^{+0.19}_{-0.20}$	$0.417^{+0.067}_{-0.058}$	1.90
0.043	$7.50^{+0.19}_{-0.20}$	$0.412^{+0.067}_{-0.057}$	1.93
0.045	$7.50^{+0.19}_{-0.20}$	$0.407^{+0.068}_{-0.055}$	1.98
0.047	$7.50^{+0.19}_{-0.20}$	$0.407^{+0.064}_{-0.058}$	2.03
0.049	$7.50^{+0.19}_{-0.20}$	$0.403^{+0.065}_{-0.056}$	2.08

Table A.5: Results of the analysis of KamLAND data alone (Ref. [38]). The $\tan^2 \theta_{12}$ and Δm_{21}^2 best fit are indicated with their 1σ errors at each θ_{13} value.

THE SOLAR-WITHOUT-BOREXINO ANALYSIS

$\sin^2 \theta_{13}$	$\tan^2 \theta_{12}$	Δm_{21}^2 ($\times 10^{-5}$ eV ²)	χ^2 (ndf=90)
0.000	$5.2_{-1.0}^{+1.6}$	$0.468_{-0.041}^{+0.030}$	94.29
0.001	$5.2_{-1.0}^{+1.6}$	$0.468_{-0.039}^{+0.031}$	94.27
0.003	$5.3_{-1.0}^{+1.6}$	$0.468_{-0.038}^{+0.034}$	94.25
0.005	$5.2_{-1.0}^{+1.7}$	$0.473_{-0.042}^{+0.033}$	94.25
0.007	$5.3_{-1.0}^{+1.7}$	$0.473_{-0.040}^{+0.036}$	94.25
0.009	$5.3_{-1.0}^{+1.7}$	$0.479_{-0.044}^{+0.032}$	94.24
0.011	$5.4_{-1.1}^{+1.7}$	$0.479_{-0.042}^{+0.035}$	94.22
0.013	$5.3_{-1.0}^{+1.9}$	$0.484_{-0.047}^{+0.034}$	94.28
0.015	$5.3_{-1.0}^{+1.9}$	$0.490_{-0.051}^{+0.030}$	94.29
0.017	$5.7_{-1.4}^{+1.5}$	$0.484_{-0.042}^{+0.039}$	94.31
0.019	$5.3_{-1.0}^{+2.0}$	$0.495_{-0.051}^{+0.030}$	94.37
0.021	$5.8_{-1.5}^{+1.5}$	$0.490_{-0.043}^{+0.038}$	94.40
0.023	$5.5_{-1.2}^{+2.0}$	$0.484_{-0.036}^{+0.047}$	94.48
0.025	$5.4_{-1.0}^{+2.1}$	$0.490_{-0.041}^{+0.045}$	94.55
0.027	$5.7_{-1.4}^{+1.9}$	$0.490_{-0.038}^{+0.047}$	94.62
0.029	$5.8_{-1.5}^{+1.9}$	$0.490_{-0.036}^{+0.050}$	94.68
0.031	$5.7_{-1.4}^{+2.0}$	$0.495_{-0.039}^{+0.048}$	94.77
0.033	$5.5_{-1.1}^{+2.2}$	$0.501_{-0.043}^{+0.045}$	94.86
0.035	$5.8_{-1.4}^{+2.0}$	$0.501_{-0.042}^{+0.050}$	94.97
0.037	$5.9_{-1.6}^{+2.0}$	$0.501_{-0.040}^{+0.052}$	95.09
0.039	$5.8_{-1.4}^{+2.1}$	$0.507_{-0.043}^{+0.049}$	95.16
0.041	$5.9_{-1.6}^{+2.1}$	$0.507_{-0.041}^{+0.052}$	95.29
0.043	$5.7_{-1.3}^{+2.5}$	$0.519_{-0.052}^{+0.044}$	95.45
0.045	$6.0_{-1.6}^{+2.2}$	$0.513_{-0.044}^{+0.053}$	95.57
0.047	$5.9_{-1.6}^{+2.3}$	$0.519_{-0.047}^{+0.050}$	95.70
0.049	$5.9_{-1.5}^{+2.8}$	$0.531_{-0.058}^{+0.043}$	95.89

Table A.6: Results of the analysis of the solar-without-Borexino data set. The $\tan^2 \theta_{12}$ and Δm_{21}^2 best fit are indicated with their 1σ errors at each θ_{13} value.

THE SOLAR-WITH-BOREXINO ANALYSIS

$\sin^2 \theta_{13}$	$\tan^2 \theta_{12}$	$\Delta m_{21}^2 (\times 10^{-5} \text{ eV}^2)$	χ^2 (ndf=99)
0.000	$5.2_{-1.0}^{+1.6}$	$0.468_{-0.040}^{+0.028}$	94.68
0.001	$5.2_{-1.0}^{+1.6}$	$0.468_{-0.039}^{+0.029}$	94.66
0.003	$5.3_{-1.0}^{+1.6}$	$0.468_{-0.037}^{+0.032}$	94.68
0.005	$5.4_{-1.1}^{+1.5}$	$0.468_{-0.037}^{+0.035}$	94.65
0.007	$5.4_{-1.0}^{+1.7}$	$0.473_{-0.041}^{+0.032}$	94.66
0.009	$5.5_{-1.2}^{+1.6}$	$0.473_{-0.038}^{+0.034}$	94.65
0.011	$5.4_{-1.1}^{+1.7}$	$0.468_{-0.044}^{+0.031}$	94.64
0.013	$5.4_{-1.1}^{+1.8}$	$0.468_{-0.033}^{+0.044}$	94.73
0.015	$5.4_{-1.0}^{+1.9}$	$0.473_{-0.036}^{+0.043}$	94.78
0.017	$5.6_{-1.2}^{+1.7}$	$0.473_{-0.034}^{+0.044}$	94.80
0.019	$5.4_{-1.0}^{+2.0}$	$0.479_{-0.038}^{+0.041}$	94.87
0.021	$5.8_{-1.4}^{+1.7}$	$0.490_{-0.048}^{+0.033}$	94.95
0.023	$5.6_{-1.2}^{+2.0}$	$0.484_{-0.041}^{+0.042}$	95.03
0.025	$5.8_{-1.4}^{+1.8}$	$0.484_{-0.038}^{+0.044}$	95.12
0.027	$5.7_{-1.3}^{+2.0}$	$0.490_{-0.044}^{+0.041}$	95.24
0.029	$5.8_{-1.4}^{+2.0}$	$0.490_{-0.041}^{+0.043}$	95.32
0.031	$5.9_{-1.5}^{+2.0}$	$0.490_{-0.040}^{+0.046}$	95.47
0.033	$5.9_{-1.4}^{+2.1}$	$0.495_{-0.045}^{+0.043}$	95.61
0.035	$6.0_{-1.5}^{+2.1}$	$0.495_{-0.042}^{+0.045}$	95.76
0.037	$5.9_{-1.4}^{+2.3}$	$0.501_{-0.048}^{+0.042}$	95.92
0.039	$6.0_{-1.5}^{+2.3}$	$0.501_{-0.046}^{+0.043}$	96.08
0.041	$6.0_{-1.4}^{+2.3}$	$0.507_{-0.051}^{+0.040}$	96.25
0.043	$6.4_{-1.9}^{+2.2}$	$0.501_{-0.046}^{+0.049}$	96.46
0.045	$6.1_{-1.5}^{+2.6}$	$0.513_{-0.057}^{+0.039}$	96.66
0.047	$6.4_{-1.8}^{+2.4}$	$0.507_{-0.051}^{+0.048}$	96.86
0.049	$6.4_{-1.8}^{+3.0}$	$0.519_{-0.064}^{+0.040}$	97.14

Table A.7: Results of the analysis of the solar-with-Borexino data set. The $\tan^2 \theta_{12}$ and Δm_{21}^2 best fit are indicated with their 1σ errors at each θ_{13} value.

THE SOLAR plus KAMLAND ANALYSIS

$\sin^2 \theta_{13}$	$\tan^2 \theta_{12}$	$\Delta m_{21}^2 (\times 10^{-5} \text{ eV}^2)$	χ^2 (ndf=105)
0.000	$7.50^{+0.16}_{-0.24}$	$0.457^{+0.025}_{-0.034}$	99.48
0.001	$7.50^{+0.16}_{-0.23}$	$0.457^{+0.026}_{-0.034}$	99.28
0.003	$7.50^{+0.16}_{-0.24}$	$0.457^{+0.030}_{-0.035}$	99.08
0.005	$7.50^{+0.16}_{-0.24}$	$0.447^{+0.042}_{-0.025}$	98.80
0.007	$7.50^{+0.16}_{-0.24}$	$0.452^{+0.037}_{-0.027}$	98.56
0.009	$7.50^{+0.16}_{-0.23}$	$0.457^{+0.030}_{-0.031}$	98.29
0.011	$7.50^{+0.16}_{-0.22}$	$0.457^{+0.033}_{-0.032}$	98.17
0.013	$7.50^{+0.17}_{-0.23}$	$0.457^{+0.032}_{-0.030}$	98.01
0.015	$7.50^{+0.17}_{-0.22}$	$0.462^{+0.029}_{-0.036}$	97.93
0.017	$7.50^{+0.17}_{-0.22}$	$0.452^{+0.043}_{-0.025}$	97.87
0.019	$7.50^{+0.17}_{-0.22}$	$0.457^{+0.038}_{-0.029}$	97.83
0.021	$7.50^{+0.17}_{-0.22}$	$0.457^{+0.038}_{-0.027}$	97.79
0.023	$7.50^{+0.18}_{-0.21}$	$0.457^{+0.038}_{-0.025}$	97.78
0.025	$7.50^{+0.18}_{-0.22}$	$0.462^{+0.033}_{-0.032}$	97.88
0.027	$7.50^{+0.18}_{-0.21}$	$0.468^{+0.028}_{-0.038}$	97.96
0.029	$7.50^{+0.18}_{-0.21}$	$0.468^{+0.032}_{-0.037}$	98.08
0.031	$7.50^{+0.18}_{-0.21}$	$0.457^{+0.044}_{-0.025}$	98.26
0.033	$7.50^{+0.18}_{-0.21}$	$0.462^{+0.039}_{-0.029}$	98.41
0.035	$7.50^{+0.18}_{-0.21}$	$0.462^{+0.041}_{-0.027}$	98.60
0.037	$7.50^{+0.18}_{-0.21}$	$0.468^{+0.034}_{-0.033}$	98.82
0.039	$7.50^{+0.19}_{-0.20}$	$0.468^{+0.033}_{-0.033}$	99.09
0.041	$7.50^{+0.19}_{-0.20}$	$0.473^{+0.031}_{-0.039}$	99.42
0.043	$7.50^{+0.19}_{-0.20}$	$0.473^{+0.033}_{-0.039}$	99.73
0.045	$7.50^{+0.19}_{-0.21}$	$0.462^{+0.046}_{-0.026}$	100.12
0.047	$7.50^{+0.19}_{-0.20}$	$0.468^{+0.041}_{-0.031}$	100.47
0.049	$7.50^{+0.19}_{-0.19}$	$0.479^{+0.032}_{-0.040}$	100.96

Table A.8: Results of the analysis of the solar-with-Borexino plus KamLAND data set. The $\tan^2 \theta_{12}$ and Δm_{21}^2 best fit are indicated with their 1σ errors at each θ_{13} value.

Bibliography

- [1] G. Bellini *et al.*, “Precision measurement of the ${}^7\text{Be}$ solar neutrino interaction rate in Borexino,” *Physical Review Letters*, vol. 107, p. 141302, 2011. 1, 58, 60, 62, 77, 82, 83, 92, 100, 127, 134
- [2] G. Bellini *et al.*, “Absence of a day-night asymmetry in the ${}^7\text{Be}$ solar neutrino rate in Borexino,” *Physics Letters B*, vol. 707, p. 22, 2012. 1, 60, 77, 82, 91, 100, 109, 127, 134
- [3] G. Bellini *et al.*, “First evidence of pep solar neutrinos by direct detection in Borexino,” *Physical Review Letters*, vol. 108, p. 051302, 2012. 1, 61, 77, 82, 94, 100, 134
- [4] G. Bellini *et al.*, “Measurement of the solar ${}^8\text{B}$ neutrino rate with a liquid scintillator target and 3 MeV energy threshold in the Borexino detector,” *Physical Review D*, vol. 82, p. 033006, 2010. 2, 60, 62, 77, 82, 86, 88, 100, 134
- [5] W. Pauli, “Letter to L. Meitner and her colleagues. December 1930,” in *Wissenschaftlicher Briefwechsel mit Bohr, Einstein, Heisenberg u.a.* (Springer, ed.), p. 39, 1985. 3
- [6] E. Fermi, “Tentativo di una teoria dell’emissione dei raggi beta,” *Ricerca Scientifica*, vol. 4, p. 491, 1933. 3
- [7] K. Nakamura *et al.*, “Review of Particle Physics - Particle Data Group,” *Journal of Physics G*, vol. 37, 2010. 6, 36, 59, 62, 79
- [8] B. Pontecorvo, “Neutrino experiments and the question of leptonic-charge conservation,” *Soviet Physics - JETP*, vol. 26, p. 984, 1968. [Zh. Eksp. Teor. Fiz. 53, 1717 (1967)]. 7
- [9] B. Pontecorvo and V. Gribov, “Neutrino astronomy and lepton charge,” *Physics Letters B*, vol. 28, p. 493, 1969. 7
- [10] H. Bethe, “Energy production in stars,” *Physical Review*, vol. 55, p. 434, 1939. 9

BIBLIOGRAPHY

- [11] A. Eddington, *The internal constitution of the stars*. Cambridge University Press, 1926. 9
- [12] K. Krane, *Introductory nuclear Physics*. John Wiley & Sons, 1998. 12
- [13] J. Bahcall, A. Serenelli, and S. Basu, “New solar opacities, abundances, helioseismology, and neutrino fluxes,” *The Astrophysical Journal Letters*, vol. 621, p. 85, 2005. 14
- [14] J. Bahcall and A. Serenelli, “How do uncertainties in the surface chemical abundances of the sun affect the predicted solar neutrino fluxes?,” *The Astrophysical Journal*, vol. 626, p. 530, 2005. 14
- [15] N. Grevesse and A. Sauval, “Standard solar composition,” *Space Science Reviews*, vol. 85, p. 161, 1998. 15, 16, 61, 62, 119, 120
- [16] M. Asplund, N. Grevesse, and A. Sauval, “The solar chemical composition,” *Nuclear Physics A*, vol. 777, p. 1, 2006. 15, 61, 119, 121
- [17] A. Serenelli, S. Basu, J. Ferguson, and M. Asplund, “New solar composition: the problem with solar models revisited,” *The Astrophysical Journal Letters*, vol. 705, 2009. 15, 16, 62, 119, 120, 121
- [18] A. Serenelli, W. Haxton, and C. Peña-Garay, “Solar models with accretion. I. Application to the solar abundance problem,” *The Astrophysical Journal*, vol. 743, p. 24, 2011. 16, 57, 62, 63, 81, 82, 83, 119, 120, 121
- [19] A. Bernstein, Y. Wang, G. Gratta, and T. West, “Nuclear reactor safeguards and monitoring with antineutrino detectors,” *Journal of Applied Physics*, vol. 91, p. 4672, 2002. 17
- [20] A. Mann, *Shadow of a star: the neutrino story of supernova 1987A*. Freeman, 1997. 18
- [21] L. Wolfenstein, “Neutrino oscillations in matter,” *Physical Review D*, vol. 17, p. 2369, 1978. 22, 62
- [22] C. Kim and A. Pevsner, *Neutrinos in Physics and Astrophysics*, vol. 8 of *Contemporary Concepts in Physics*, p. 1. 1993. 23
- [23] F. Vissani and A. Strumia, “Neutrino masses and mixings and....” arXiv: 0606054v3[hep-ph], 2010. 28

-
- [24] R. D. Jr., D. Harmer, and K. Hoffman, "Search for neutrinos for the sun," *Physical Review Letters*, vol. 20, p. 1205, 1968. 29
- [25] B. Cleveland *et al.*, "Measurement of the solar electron neutrino flux with the Homestake Chlorine detector," *The Astrophysical Journal*, vol. 496, p. 505, 1998. 30, 77, 100, 135
- [26] A. Abazov *et al.*, "Search for neutrinos from sun using the reaction $^{71}\text{Ga}(\nu_e, e^-)^{71}\text{Ge}$," *Physical Review Letters*, vol. 67, p. 3332, 1991. 30
- [27] P. Anselmann *et al.*, "Solar neutrinos observed by GALLEX at Gran Sasso," *Physics Letters B*, vol. 285, p. 376, 1992. 30
- [28] M. Altmann *et al.*, "Complete results for five years of GNO solar neutrino observations," *Physics Letters B*, vol. 616, p. 174, 2005. 30
- [29] F. Kaether *et al.*, "Reanalysis of the GALLEX solar neutrino flux and source experiments," *Physics Letters B*, vol. 685, p. 47, 2010. 30, 77, 100, 103, 135
- [30] J. Abdurashitov *et al.*, "Measurement of the solar neutrino capture rate with gallium metal. III: Results for the 2002-2007 data-taking period," *Physical Review C*, vol. 80, p. 015807, 2009. 30, 77, 100, 103, 135
- [31] J. Hosaka *et al.*, "Solar neutrino measurements in Super-Kamiokande-I," *Physical Review D*, vol. 73, p. 112001, 2006. 31, 62, 77, 78, 100, 137
- [32] J. Cravens *et al.*, "Solar neutrino measurements in Super-Kamiokande-II," *Physical Review D*, vol. 78, p. 032002, 2008. 31, 62
- [33] K. Abe *et al.*, "Solar neutrino results in Super-Kamiokande-III," *Physical Review D*, vol. 83, p. 052010, 2011. 31, 62, 77, 78, 100, 107, 137
- [34] B. Aharmin *et al.*, "Determination of the ν_e and total ^8B solar neutrino fluxes using the Sudbury Neutrino Observatory Phase I data set," *Physical Review C*, vol. 75, p. 045502, 2007. 32, 62
- [35] B. Aharmin *et al.*, "Low-Energy-Threshold-Analysis of the phase I and phase II data sets of the Sudbury Neutrino Observatory," *Physical Review C*, vol. 81, p. 055504, 2010. 32, 62, 77, 100, 103, 104, 114, 136
- [36] B. Aharmin *et al.*, "Measurement of the ν_e and total ^8B solar neutrino fluxes with the Sudbury Neutrino Observatory phase-III data set.." arXiv: 1107.2901[nucl-ex], 2011. 32

BIBLIOGRAPHY

- [37] B. Aharmin *et al.*, “Combined analysis of all three phases of solar neutrino data from the Sudbury Neutrino Observatory.” arXiv: 1109.0763[nucl-ex], 2011. 32, 62, 105
- [38] A. Gando *et al.*, “Constraints on θ_{13} from a three-flavor oscillation analysis of reactor antineutrinos at KamLAND,” *Physical Review D*, vol. 83, p. 052002, 2011. 33, 77, 81, 100, 111, 114, 118, 138
- [39] G. Fogli, E. Lisi, and D. Montanino, “A comprehensive analysis of solar, atmospheric, accelerator and reactor neutrino experiments in a hierarchical three generation scheme,” *Physical Review D*, vol. 49, p. 3626, 1994. 34
- [40] J. Bahcall, M. Gonzalez-Garcia, and C. Peña-Garay, “Global analysis of solar neutrino oscillations including SNO CC measurement,” *Journal of High Energy Physics*, p. 014, 2001. 35
- [41] G. Fogli, E. Lisi, D. Montanino, and A. Palazzo, “Quasi-vacuum solar neutrino oscillations,” *Physical Review D*, vol. 62, p. 113004, 2000. 35
- [42] G. Alimonti *et al.*, “Science and technology of Borexino: a real time detector for low energy solar neutrinos,” *Astroparticle Physics*, vol. 16, p. 205, 2002. 41
- [43] D. D’Angelo, *Towards the detection of low energy solar neutrino in Borexino: data readout, data reconstruction and background identification*. PhD thesis, Technische Universität München, 2006. 43
- [44] M. Wurm, *Cosmic background discrimination for the rare neutrino event search in Borexino and LENA*. PhD thesis, Technische Universität München, 2009. 43
- [45] J. Benziger *et al.*, “The scintillator purification system for the Borexino solar neutrino detector,” *Nuclear Instruments and Methods A*, vol. 587, p. 277, 2008. 44
- [46] V. Lagomarsino and G. Testera, “A gateless charge integrator for Borexino energy measurements,” *Nuclear Instruments and Methods A*, vol. 430, p. 435, 1999. 44
- [47] G. Alimonti *et al.*, “Light propagation in a large volume liquid scintillator,” *Nuclear Instruments and Methods A*, vol. 440, 2000. 45
- [48] G. t’Hooft, “Prediction for neutrino-electron cross-sections in Weinberg’s model of weak interactions,” *Physics Letters B*, vol. 37, p. 195, 1971. 48
- [49] E. Bellotti *et al.*, “New measurement of rock contaminations and neutron activity in the Gran Sasso tunnel,” Tech. Rep. INFN/TC-85/19, INFN, 1985. 52

-
- [50] S. Ahlen *et al.*, “Study of penetrating cosmic ray muons and search for large scale anisotropies at the Gran Sasso Laboratory,” *Physics Letters B*, vol. 249, no. 1, p. 149, 1990. 53
- [51] S. Ahlen *et al.*, “Muon astronomy with the MACRO detector,” *The Astrophysical Journal*, vol. 412, p. 301, 1993. 53
- [52] M. Robinson *et al.*, “Measurements of muon flux at 1070 m vertical depth in the Boulby underground laboratory,” *Nuclear Instruments and Methods A*, vol. 551, p. 347, 2003. 53
- [53] G. Bellini *et al.*, “Muon and cosmogenic neutron detection in Borexino,” *Journal of Instrumentation*, vol. 6, 2011. 53
- [54] P. Belli *et al.*, “Deep underground neutron flux measurement with large BF3 counters,” *Il Nuovo Cimento A*, vol. 101, p. 959, 1989. 53
- [55] C. Arpesella *et al.*, “Direct measurement of the ${}^7\text{Be}$ solar neutrino flux with 192 days of Borexino data,” *Physical Review Letters*, vol. 101, p. 091302, 2008. 57, 58
- [56] V. Barger, D. Marfatia, and K. Whisnant, “Testing the LMA solution with solar neutrinos independently of solar models,” *Physics Letters B*, vol. 617, p. 78, 2005. 59
- [57] J. Bahcall, A. Serenelli, and S. Basu, “10,000 Standard solar models: a Monte Carlo simulation,” *The Astrophysical Journal Supplement*, vol. 165, p. 400, 2006. 61, 87, 123
- [58] A. Serenelli, “New results on standard solar models,” *Astrophysics and space science*, vol. 328, p. 13, 2009. 61
- [59] S. Mikheyev and A. Smirnov, “Resonance amplification of oscillations in matter and spectroscopy of solar neutrinos,” *Soviet Journal of Nuclear Physics*, vol. 42, p. 913, 1985. 62
- [60] P. de Holanda and A. Smirnov, “LMA-MSW solution of the solar neutrino problem and first KamLAND results,” *Journal of Cosmology and Astroparticle Physics*, vol. 0302, 2003. 62
- [61] Q. Ahmad *et al.*, “Measurement of the rate of $\nu_e + d \rightarrow p + p + e^-$ interactions produced by ${}^8\text{B}$ solar neutrinos at the Sudbury Neutrino Observatory,” *Physical Review Letters*, vol. 87, p. 071301, 2001. 62

BIBLIOGRAPHY

- [62] S. Basu, “The solar metallicity problem: what is the solution?,” *ASP Conference Series*, vol. 419, 2009. Proceeding of GONG 2008/SOHO XXI meeting. 63
- [63] G. Bellini *et al.*, “Observation of geo-neutrinos,” *Physics Letters B*, vol. 687, p. 299, 2010. 63, 65
- [64] G. Fogli *et al.*, “Geo-neutrinos: an approach to their uncertainties and correlations,” *Physics Scripta*, p. 89, 2006. 64
- [65] F. Mantovani, L. Carmignani, G. Fiorentini, and M. Lissia, “Antineutrinos from earth: a reference model and its uncertainties,” *Physical Review D*, vol. 69, p. 013001, 2004. 64
- [66] J. Bahcall and C. Peña-Garay, “A roadmap to solar neutrino fluxes, neutrino oscillation parameters and tests for new physics,” *Journal of High Energy Physics*, p. 004, 2003. 67, 101, 120
- [67] T. Kuo and J. Pantaleone, “Three-neutrino oscillations and the solar-neutrino experiments,” *Physical Review D*, vol. 35, p. 3432, 1987. 68, 69
- [68] G. Fogli, E. Lisi, and D. Montanino, “Comprehensive analysis of solar, atmospheric, accelerator and reactor neutrino experiments in a hierarchical three-generation scheme,” *Physical Review D*, vol. 49, p. 3626, 1994. 68, 69
- [69] M. Gonzalez-Garcia and C. Peña-Garay, “Global and unified analysis of solar neutrino data,” in *Nuclear Physics B*, vol. 91 of *Proceedings Supplements*, p. 80, 2001. Proceedings of the Neutrino 2000 conference, Sudbury, (CA). 69
- [70] C. Peña-Garay and A. Serenelli, “Solar neutrinos and the solar composition problem.” arXiv: 0811.2424[astro-ph], 2008. 72, 73
- [71] J. Bahcall, W. Fowler, I. Iben, and R. Sears, “Solar neutrino flux,” *The Astrophysical Journal*, vol. 137, p. 344, 1963. 72, 73
- [72] J. Bahcall, “Solar neutrinos. I. Theoretical,” *Physical Review Letters*, vol. 12, p. 300, 1964. 72, 73
- [73] J. Bahcall, *Neutrino astrophysics*. Cambridge University Press, 1st ed., 1989. 72, 73
- [74] J. Bahcall, “Solar model: an historical overview,” in *Nuclear Physics B*, vol. 118 of *Proceedings Supplements*, p. 77, 2003. Proceedings of the XXth International Conference on Neutrino Physics and Astrophysics. 72, 73

- [75] E. Lisi and D. Montanino, “Earth regeneration effect in solar neutrino oscillation: an analytic approach,” *Physical Review D*, vol. 56, p. 1792, 1997. 74
- [76] A. Dziewonski and D. Anderson, “Preliminary Reference Earth Model,” *Physics of the Earth and Planetary Interiors*, vol. 25, p. 297, 1981. 74, 75
- [77] B. Aharmim *et al.*, “Independent measurement of the total active ^8B solar neutrino flux using an array of the ^3He proportional counters at the Sudbury Neutrino Observatory,” *Physical Review Letter*, vol. 101, p. 111301, 2008. 77, 100, 103, 136
- [78] M. Gonzalez-Garcia, M. Maltoni, and J. Salvado, “Updated global fit to three neutrino mixing: status of the hints of $\theta_{13} > 0$,” *Journal of High Energy Physics*, p. 056, 2010. 77, 99, 116, 118
- [79] G. Fogli, E. Lisi, A. Marrone, A. Palazzo, and A. Rotunno, “Evidence of $\theta_{13} > 0$ from global neutrino data analysis.” arXiv: 1106.6028[hep-ph], submitted to Phys. Rev. D, 2011. 77, 112
- [80] J. Bahcall, “Neutrino-electron scattering and solar neutrino experiments,” *Reviews of Modern Physics*, vol. 59, p. 505, 1987. 78
- [81] J. Bahcall, “Gallium solar neutrino experiments: absorption cross sections, neutrino spectra, and predicted event rates,” *Physical Review C*, vol. 56, p. 3391, 1997. 78
- [82] J. Bahcall, “The ^7Be solar neutrino line: a reflection of the central temperature distribution of the sun,” *Physical Review D*, vol. 49, p. 3923, 1994. 84
- [83] J. Pantaleone, “Suppression of solar line neutrino oscillations,” *Physical Review D*, vol. 43, p. 2436, 1991. 95
- [84] G. Fogli, E. Lisi, A. Marrone, and A. Palazzo, “Global analysis of three-flavor neutrino masses and mixings,” *Progress in Particle and Nuclear Physics*, vol. 57, p. 742, 2006. 110
- [85] G. Fogli, E. Lisi, A. Marrone, A. Palazzo, and A. Rotunno, “Hints of $\theta_{13} > 0$ from global neutrino data analysis,” *Physical Review Letters*, vol. 101, p. 141801, 2008. 112
- [86] J. Bahcall, M. Gonzalez-Garcia, and C. Peña-Garay, “Does the sun shine by pp or CNO fusion reactions?,” *Physical Review Letters*, vol. 90, p. 131301, 2003. 119
- [87] J. Bahcall, “The luminosity constraint on solar neutrino fluxes,” *Physical Review C*, vol. 65, p. 025801, 2002. 120

BIBLIOGRAPHY

- [88] M. Spiro and D. Vignaud, "Solar model independent neutrino oscillation signals in the forthcoming solar neutrino experiments?," *Physics Letters B*, vol. 242, p. 279, 1990. 120

Acknowledgements

Il problema “Alessandra Carlotta, non sei molto brava a scrivere” era arcinoto fin dai tempi delle elementari, circa venti (?!?) anni fa, quando la maestra Annamaria una volta disse (in napoletano stretto) “Alessà, allunga la broda!”. Ahimè, di anni ne sono passati parecchi ma la difficoltà a mettere nero su bianco i mille pensieri di passaggio nella mia testolina permane, anche in questo momento! Momento in cui ho finalmente la possibilità di dire grazie e di ricordare le persone che mi hanno aiutata, spronata e accompagnata.

Famiglia, rientrate in tutte queste categorie lo sapete vero? Vi dedico questo lavoro e il traguardo che oggi raggiungo. E poi... Grazie, grazie per essere voi!

Grazie al mio papà, che continuerà a chiedermi se anche domani devo andare a scuola ma che, in fin dei conti, lo sa che ormai son più vicina ai trent’anni che alla scuola dell’obbligo. Ti voglio tanto bene papà! Grazie alla mia mamma, che è stata la prima persona a farmi sentire adulta e che ogni giorno mi rende tanto fiera della persona che è. Grazie alla mia sorellina Dr.ssa Federica Re, medico chirurgo: la dolce, solida roccia continua la sua strada alla conquista del mondo... e, a quanto pare, in dolce e solida compagnia.

Per quanto riguarda i ringraziamenti “accademici”, vorrei per prima cosa dire grazie alla Prof.ssa Emanuela Meroni che in questi tre anni mi ha indirizzata, sostenuta e, diciamo, bacchettata a dovere quando necessario.

Un sentito grazie al Dr. Eligio Lisi che, con la sua paziente e accurata opera di revisione, mi ha aiutata a capire (e sbrogliare) i nodi di questo lavoro.

Grazie alla Dr.ssa Barbara Caccianiga. Alla Dr.ssa Caccianiga vorrei dire che è stata un aiuto insostituibile e prezioso: con il suo spirito di osservazione mi ha insegnato come avvicinarmi al mondo della Fisica. Vorrei invece ringraziare Barbara per l’amicizia nata tra noi, per le risate, per avermi ascoltata nei momenti difficili, per le sedute in palestra e per le folli, circensi, manovre spagnole... Olè!

A proposito di Spagna, non posso non ringraziare il Dr. Carlos Peña-Garay che, oltre ad essere stato il mio magister di Fisica del neutrino, ha collaborato e reso possibile lo

sviluppo del lavoro che presento in tesi. Senza tener conto delle sue fantastiche guide tra Madrid e Valencia... Gracias Carlos!

La Dr.ssa Livia Ludhova, oltre ad essere un'ottima compagna di tennis (finchè io non ho fatto crac), è una scienziata eccezionale ed è un'amica con cui ho condiviso tanti momenti di questi tre anni. Cara Livia, spero con tutto il cuore che a breve brevissimo tu possa ottenere tutto quello per cui, con la serietà che ti contraddistingue, stai caparbiamente lottando.

Il Dr. Pietro Biassoni. Caro Pietro, ne è passato di tempo da quando ci siamo incontrati per la prima volta nella stanza stampanti eh? Sono certa che l'amicizia che ci lega continuerà a lungo. Al terzo piano si sente già la tua mancanza...

Ovviamente, saluto/ringrazio anche il dottor Trezzi, che da quando è lunatico, ci luna di brutto!

Ringrazio tutto il gruppo Borexino Milano in particolare il prof. Giampaolo Bellini, Gioacchino Ranucci, Paolo Lombardi, Augusto Brigatti, Luciana, Silvia e, ovviamente, Megghi, il nonno DD e Pietro.

Quando lasciai i Laboratori Nazionali del Gran Sasso a fine tesi magistrale, pensavo proprio che non avrei più rivisto quelle montagne tanto care. Invece, nel periodo del dottorato, ho avuto modo di continuare a "vivere" L'Aquila e le persone che l'abitano e le danno anima e corpo... anche dopo il terribile terremoto del 2009.

Il lavorare in Borexino e l'essere spesso presente ai labs hanno inoltre reso possibile l'incontro con tanti nuovi amici. In primis, i "miei" genovesi ovvero Stefano, SD, Guido, Alessio e il Dr. Carraro Carlo; i gransassini D.O.C. ovvero Yura, Chiara, George, Ale, Yusuke (anche se ora sei tornato in Giappone, sarai sempre un gransassino! Arigatou gozaimashita Koshio-san), Andrea Ianni e Stefano Gazzana con il suo bagaglio di esperienze romane-de-Roma. Ringrazio e saluto anche tutti gli amici esterofili: Davide Franco, Carlos Martinez, Szymon Manecky, Richard Saldhana, Alvaro Chavarria, David Montanari, Elena Guardincerri e Iulian Bandac.

Vorrei in particolare rivolgere un pensiero al dr. Stefano Perasso e al dott. (ma futuro dr.) Guido Fernandes.

Caro Stefano, in questi anni ci siamo ben conosciuti e sostenuti in situazioni di ogni tipo, dai momenti faticosi alla gioia per la nascita delle tue nipotine. Anche se tu e la Eli siete a 5000 miglia di distanza, so che posso contare sul tuo appoggio e questo è un dono meraviglioso! Stefano ed Elisabetta: due genovesi alla conquista della East-Cost! Mi mancate un sacco!

Guido, compagno di turni di calibrizioni notturne dentro la montagna, di infinite chat metafisiche o frivole che fossero. Che la nostra amicizia possa crescere e maturare sempre più!

Mentre scrivo, i volti di tante persone che vorrei ringraziare, si affacciano alla mente.

Penso a Marcella ed Antonio che non mi hanno mai persa d'occhio da quando sono venuta al mondo e che si sono sempre interessati a tutte le attività che mi vedevano coinvolta.

A Rino, Bianca, Federica e Riccardo che mi hanno accolta nella loro famiglia e mi hanno fatta sentire ben accetta dal primo istante.

A Stefania, una donna unica che con la sua sensibilità e la sua discreta amicizia sa essere presente nella mia vita come nessun'altra.

A Lucia, una stellina che diventa ogni giorno più luminosa.

Ad Alberto Lemut, amico sempre disponibile all'ascolto, che mi ha offerto un tetto nella mia prima incursione californiana! Caro Albe, grazie di cuore!

Alla Dr.ssa Valentina Presotto e al Dr. Davide Vasco, PhD! Insieme nella specialistica... insieme nel dottorato!

Ad Irene, Marzia, Elena e ovviamente a SD in qualità di Stefanino, l'anima del gruppo! È stato fantastico incontrarci nella calda estate spagnola e ancor più fantastico è riuscire a non perdersi di vista, nonostante esperimenti sparsi ovunque nel mondo: continuiamo così!

E poi, un pensiero e un grazie a Te, splendida persona con cui ho scoperto la bellezza del poter dire noi... La bellezza del sognare, del desiderare e del poter effettivamente costruire un futuro... Insieme. Mano destra sul cuore, amore mio.

